DYNAMIC SIMULATION OF MULTIBODY SYSTEMS IN SIMULTANEOUS, INDETERMINATE CONTACT AND IMPACT WITH FRICTION

by

ADRIAN RODRIGUEZ

Presented to the Faculty of the Graduate School of
The University of Texas at Arlington in Partial Fulfillment
of the Requirements
for the Degree of

DOCTOR OF PHILOSOPHY

THE UNIVERSITY OF TEXAS AT ARLINGTON

May 2014

To Amanda

"in aeternum et nam semper"

Acknowledgements

Thank you to my supervising professor Dr. Alan Bowling first and foremost, for the opportunity to join your research lab – Robotics, Biomechanics and Dynamic System laboratory – allowing me to demonstrate to you my dedicated work ethic. I am very grateful for your relentless support throughout my research work and the push to "just keep on going." There were some struggles along the way, dealing with tough reviewers and publishing our work but we made it through. Best of all, I enjoyed the conference trips and the exposure to a global research community like nothing I have ever experienced.

I would like to thank the members of my dissertation committee: Dr. Panos Shiakolas, Dr. Kent Lawrence, Dr. Bo Wang, and Dr. Ashfaq Adnan for their enthusiastic support from my research work after my comprehensive exam. It delights me to know that all my hard work has made some kind of impression among a distinguished group of faculty members and experienced researchers.

I would also like to acknowledge past and present colleagues in my research lab. George Teng, the *Taiwanese Terror* and loyal Dallas sports fan. Thank you for being a great friend, and someone I could hang out with and get to know outside of the lab. I am honored to have you serve as one of my groomsguard for my wedding. Dr. Daniel M. Flickinger, I am thankful for your guidance during my initial transition into the lab. I had a lot of questions but your patience and willingness to answer my questions benefited me tremendously. I enjoyed our regular lunch meetings and conversations about random topics – I wonder if that wasp is still clocking in to work? Dr. Mahdi Haghshenas-Jaryani, we joined the lab at about the same time and I feel like we

witnessed each other grow with our research work and endure the same struggles with reviewers. I enjoyed the partnerships on various lab projects and am grateful that we shared a strong ability to help each other out. Michael Tadros, thank you for your valuable technical advice and insightful talks. You are truly a great mechanical engineer and I see you as a successful Chief Technology Officer for a company, but I know you like to get into the thick of things and get your hands dirty. Last but not least, Anudeep Palanki, my ships first mate and dear friend. Best of luck to you in all of your endeavors.

Special thanks to all the friends that I met at UT Arlington. There are some people doing great things and I look forward to their future careers. Thank you Lisa Berry for affording me the rare opportunity of being a fellow of the LSAMP-BD program. You were a great mentor throughout my doctorate work. In addition, the friends that I met during my undergrad studies at Texas and resource during my graduate work. They have become a great network of professional contacts who have gone out and actually "changed the world." I am grateful to know these incredible people and continue to remain in contact. I also cannot forget to acknowledge my close friends that I have known since my elementary and middle school days. I enjoyed our yearly get-togethers for holidays when we would visit our families back home. You guys are awesome and have become great people that I truly cherish.

To my family: Arnoldo, Virginia, Arnold and Monica. You guys continue to stand by my side and support me in every endeavor. Sometimes you did not understand why I wanted to stay in school and study, hoping that I would get a job. But you trusted in my decisions and now I can finally get a job! Thank you to my future father and mother in-law, Hugo and Raquel. You guys have always accepted me as a son and helped through the good and the bad, no questions asked. And of course, I am most grateful for my better half and confidant, Amanda. Your

unwavering support and patience helped me get through the pursuit of my doctorate degree. I sincerely appreciate the times you kept me sane by being the person I could share my problems with. I especially enjoyed the times when you would try to stay up late with me while I worked and occasionally going on those snack runs. I cannot wait for our wedding at the end of the year and I look forward to the start of a new chapter in our lives together.

April 7, 2014

Abstract

DYNAMIC SIMULATION OF MULTIBODY SYSTEMS IN SIMULTANEOUS, INDETERMINATE CONTACT AND IMPACT WITH FRICTION

ADRIAN RODRIGUEZ, Ph.D.

The University of Texas at Arlington, 2014

Supervising Professor: Alan Bowling

This research is focused on improving the solutions obtained using theory in contact and impact modeling. A theoretical framework is developed which can simulate the performance of dynamic systems within a real world environment. This environment involves conditions, such as contact, impact and friction. Numerical simulation provides an easy way to perform numerous iterations with varying conditions, which is more cost effective than building equivalent experimental setups. The developed framework will serve as a tool for engineers and scientists to gain some insight on predicting how a system may behave. The current field of research in multibody system dynamics lacks a framework for modeling simultaneous, indeterminate contact and impact with friction. This special class of contact and impact problems is the major focus of this research. This research develops a framework, which contributes to the existing literature.

The contact and impact problems examined in this work are indeterminate with respect to the impact forces. This is problematic because the impact forces are needed to determine the slip-state of contact and impact points. The novelty of the

developed approach relies on the formation of constraints among the velocities of the impact points. These constraints are used to address the indeterminate nature of the collisions encountered. This approach strictly adheres to the assumptions of rigid body modeling in conjunction with the notion that the configuration of the system does not change in the short time span of the collision. These assumptions imply that the impact Jacobian is constant during the collision, which enforces a kinematic relationship between the impact points.

The developed framework is used to address simultaneous, indeterminate contact and impact problems with friction. In the preliminary stages of this research, an iterative method, which incorporated an optimization function was used obtain the solutions for numerical solution to the collision. In an effort to improve the time and accuracy of the results, the iterative method was replaced with an analytical approach and implemented with the constraint formulation to achieve more energetically consistent solutions (i.e. there are no unusual gains in energy after the impact). The details of why this claim is valid will be discussed in more detail in this dissertation. The analytical framework was developed for planar contact and impact problems, while a numerical framework is developed for three-dimensional (3D) problems. The modeling of friction in 3D presents some challenging issues that are well documented in the literature, which make it difficult to apply an analytical framework. Simulations are conducted for a planar ball, planar rocking block problem, Newton's Cradle, 3D sphere, and 3D rocking block. Some examples serve as benchmark problems, in which the results are validated using experimental data.

Table of Contents

Acknowledgements iv

Abstract vii

List of Illustrations xii

List of Tables xvi

Chapter Page

1. Introduction 1

1.1 Overview 1

1.2 Motivation and Problem Statement 2

1.3 Research Contributions 5

2. Contact and Impact Modeling 8

2.1 Contact Models 8

2.2 Friction Models 9

2.3 Complementarity Conditions 11

2.4 Event-Based Simulation Technique 13

3. Indeterminate Contact and Impact 16

3.1 Simultaneous, Multiple Point Impact 16

3.2 Rigid Body Constraints 17

3.3 Constraint Projection 20

3.4 Summary 22

4. Energy Dissipation 24

4.1 Restitution Coefficients 24

4.2 Work-Energy Theory 27

4.3 Stronge's Hypothesis For Multiple Point Impact 31
4.4 Summary 32
5. Two-Dimensional Impact: Analytical Framework 34
5.0.1 Equations of Motion 34
5.0.2 Initial Sliding 35
5.1 Evaluating the Stick-Slip Transition (ST) 38
5.1.1 Slip Resumption (R) 39
5.1.2 Slip-Reversal (S-R) 39
5.1.3 Sticking (S) 40
5.2 No-Slip Condition 43
5.3 Summary 44
6. Simulation Results: Two-Dimensional Examples 46
6.1 Example 1: Planar Ball 46
6.2 Example 2: Planar Rocking Block 50
6.2.1 Case 1: Frictionless Rocking Block 51
6.2.2 Case 2: Frictional Rocking Block 54
6.3 Example 3: Three-Ball Newton's Cradle 58
6.3.1 Case 1: Uniform, Unit Mass and $e_* = 1$ 59
6.3.2 Case 2: Uniform Mass and $e_* = 0.85$ 62
6.4 Summary 68
7. Three-Dimensional Impact: Numerical Framework 69
7.1 Equations of Motion 72
7.2 Rigid Body Constraints 75
7.3 Evaluating the Stick-Slip Transition 77
7.4 Energy Dissipation 78
7.5 Summary 80

8. Simulation Results: Three-Dimensional Examples 82
8.1 Example 4: Sphere Impacting a Corner 82
8.2 Example 5: Three-Dimensional Rocking Block 85
8.2.1 Case 1: Three Corner Impact Points 87
8.2.2 Case 2: Four Corner Impact Points 90
8.2.3 Case 3: Three Centered Impact Points 93
8.3 Summary 96
Appendix
A. Constraint Projection Proof 98
B. Constraint and Slip-State Derivations 103
C. Equations of Motion: Kane's Method 112
D. Additional Example: Five-Ball Newton's Cradle 116
References 128
Biographical Information 137

List of Illustrations

Figure		Page
1.1	Rigid body impact of two bodies and line of impact	2
1.2	(a) Planar model of a ball example and (b) velocities and forces at impact points 1 (ground) and 2 (wall)	4
2.1	Pre– and post-impact regions for discrete modeling approach	8
2.2	Friction cone based on theory of Coulomb friction	10
2.3	Check function of numerical integration for simulation	14
2.4	Flow process used for the simulation of impact problems	15
3.1	Planar ball model with two arbitrary impact points A and B	17
3.2	Three dimensional model of a sphere impacting a corner	19
4.1	Example of compression and restitution effects on a compliant body .	24
4.2	Normal velocity propagation for single point impact	25
4.3	Example plot of the normal work for an impact event showing the shifts that may occur from the stick-slip transition.	29
5.1	Evolution of velocities during initial sliding when (a) one point, or (b) two points come to rest	35
5.2	Typical friction behaviors after the stick-slip transition if (a) one point, or (b) two points come to rest	37
5.3	Check of the no-slip condition in (2.3) for (a) one point using (5.13), or (b) two points using (5.15) for stick after the stick-slip transition . .	41
6.1	(a) Planar model of the ball example (repeated) and (b) velocities and forces at impact points 1 (ground) and 2 (wall) (repeated)	46

6.2 (a) Simulation of the planar ball example and (b) energy consistency for the simulation 47
6.3 (a) Normal work done and (b) evolution of velocities throughout the impact event for the planar ball example 49
6.4 (a) Planar model of a planar rocking block example and (b) velocities and forces at the impact points 50
6.5 (a) Normal work done and (b) evolution of velocities throughout the first impact event for the frictionless rocking block example 51
6.6 (a) Normal work done and (b) evolution of velocities throughout the second impact event for the frictionless rocking block example 52
6.7 (a) Simulation of the frictionless rocking block example and (b) energy consistency for the simulation 53
6.8 (a) Normal work done and (b) evolution of velocities throughout the first impact event for the frictional rocking block example 55
6.9 (a) Normal work done and (b) evolution of velocities throughout the second impact event for the frictional rocking block example 56
6.10 Simulation of the frictional rocking block example and (b) energy consistency for the simulation 57
6.11 (a) Planar model of a three-ball Newton's Cradle and (b) forces at the impact points for each ball 58
6.12 (a) Simulation of the three-ball Newton's Cradle with $e_* = 1$ and (b) table of velocities and generalized speeds 59
6.13 (a) Normal work done and (b) evolution of velocities throughout the impact event for the three-ball Newton's Cradle with $e_* = 1$ 60
6.14 (a) Generalized speeds for the three-ball Newton's Cradle and (b) energy consistency throughout the simulation with $e_* = 1$ 61

6.15 (a) Simulation of the three-ball Newton's Cradle with $e_* = 0.85$ and (b) table of velocities and generalized speeds. 63
6.16 (a) Normal work done and (b) evolution of velocities throughout the first impact event for the three-ball Newton's Cradle with $e_* = 0.85$ . . 64
6.17 (a) Normal work done and (b) evolution of velocities throughout the second impact event for the three-ball Newton's Cradle with $e_* = 0.85$ 65
6.18 (a) Generalized speeds for the three-ball Newton's Cradle and (b) energy consistency throughout the simulation with $e_* = 0.85$ 66
7.1 (a) Slip plane of an impact point coming to rest and (b) evolution of normal and sliding velocities throughout an impact event 69
7.2 Hodograph of an impact point throughout an impact event 70
7.3 Three-dimensional model of a rocking block example with three corner impact points 71
8.1 Three dimensional model of a sphere impacting a corner (repeated) . 82
8.2 (a) Simulation results of the 3D sphere example impacting a corner and (b) trajectory of sphere's mass center 83
8.3 Energy consistency of the 3D sphere example impacting a corner . . . 84
8.4 (a) Normal work done and (b) evolution of sliding velocities, sliding directions, and normal velocities throughout the impact event for the 3D sphere example 85
8.5 Three-dimensional model of a rocking block example with three corner impact points (repeated) 86
8.6 (a) Simulation of the 3D rocking block example with three corner impact points and (b) energy consistency for the simulation 87

8.7 (a) Normal work done and (b) evolution of sliding velocities, sliding directions, and normal velocities throughout the first impact event for the 3D rocking block example with three corner impact points 88
8.8 (a) Normal work done and (b) evolution of sliding velocities, sliding directions, and normal velocities throughout the second impact event for the 3D rocking block example with three corner impact points . . . 89
8.9 Three-dimensional model of a rocking block example with four corner impact points 90
8.10 (a) Simulation of the 3D rocking block example with four corner impact points and (b) energy consistency for the simulation 91
8.11 (a) Normal work done and (b) evolution of sliding velocities, sliding directions, and normal velocities throughout the first impact event for the 3D rocking block example with four corner impact points 92
8.12 (a) Normal work done and (b) evolution of sliding velocities, sliding directions, and normal velocities throughout the second impact event for the 3D rocking block example with four corner impact points . . . 93
8.13 Configuration of the (a) three corner impact points used for *Case 1* and (b) three centered impact points used for *Case 3* 94
8.14 (a) Simulation of the 3D rocking block example with three centered impact points and (b) energy consistency for the simulation 95
8.15 (a) Normal work done and (b) evolution of sliding velocities, sliding directions, and normal velocities throughout the first impact event for the 3D rocking block example with three centered impact points 96
8.16 (a) Normal work done and (b) evolution of sliding velocities, sliding directions, and normal velocities throughout the second impact event for the 3D rocking block example with three centered impact points . . 97

List of Tables

Table Page

6.1 Velocities and generalized speeds for the planar ball simulation. 48

6.2 Comparison of theoretical and experimental results for a frictionless rocking block with $m = 2.5\ kg$, $b = 0.1087\ m$, $h = 0.0645\ m$ and $\theta_1 = \theta_2 = 0^\circ$ in [1]. 53

6.3 Comparison of a frictional rocking block to theoretical and experimental results of a frictionless case. 55

6.4 Comparison of theoretical and experimental results of the three-ball Newton's Cradle with $m = 0.166\ kg$ and $e = 0.85$ (Table 2, [2]). 65

6.5 Model and simulation parameters for the three-ball Newton's Cradle cases. 67

Chapter 1

Introduction

1.1 Overview

The goal of this research is to study the interaction of a dynamic system with its environment by considering factors, such as friction and restitution. A dynamic system here is referred to as a system of multiple, interconnected bodies, or *multibody system* as known in the literature. It is assumed that the collisions experienced by the multibody systems considered in this work are rigid body impacts. Herein, impact is classified as the abrupt interaction between colliding bodies and contact is considered as a succession of impacts. This allows impact and contact to be treated within the same framework. The framework which will be developed is accomplished from a rigid body dynamics approach. In other words, the multibody systems are strictly assumed to be composed of rigid bodies, in which any local deformation as a result of impact is considered to be very small and negligible. This assumption will serve as the cornerstone of the method for treating a special class of problems encountered in multibody dynamics: simultaneous, indeterminate contact and impact with friction.

Before moving forward with the details of this work, it is important to define some other key aspects of the methods used to develop the analytical-numerical framework. This work is focused on the impact dynamics of collisions, which takes into consideration the forces, impulses and velocities involved as opposed to its mechanics. The mechanics of collisions deal with stress, displacement (i.e. local indentation) and wave propagation of forces, which are not considered in this research.

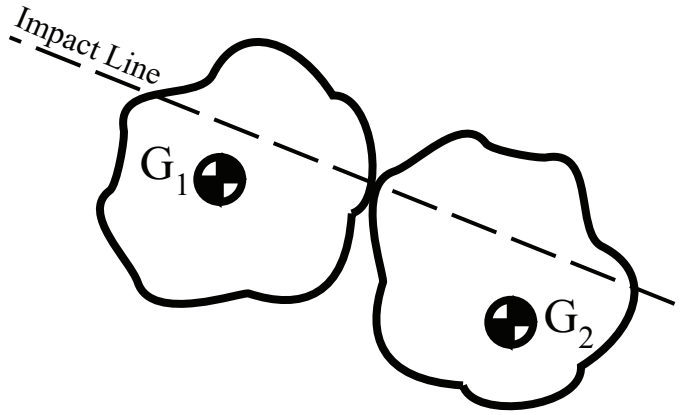

Figure 1.1. Rigid body impact of two bodies and line of impact.

Another key aspect of rigid body collisions is the type of impact encountered, which can be classified into the following: collinear, eccentric, oblique, and direct. Consider, for example, the rigid body impact of two bodies with respective mass centers G_1 and G_2, as depicted in Fig. 1.1. Collinear, or central, impact involves the case in which both mass centers of the bodies lie on the line of impact, whereas eccentric impact means that one or none of the mass centers lie on the line of impact. The latter case is a prominent one to consider for three-dimensional (3D) impact due to the effect of the configuration on the nonlinear behavior of friction but is typically only observed in single point impact [3, 4, 5, 6, 7, 8]. Oblique impact is similar to the definition of eccentric impact but replaces mass centers with initial velocities of the two bodies. Direct impact indicates that the initial velocities lie on the line of impact. The primary types of impact simulated in this research are collinear and direct impact but are not limited to these cases.

1.2 Motivation and Problem Statement

The motivation for this research is to narrow the gap between theory and practice in contact and impact modeling. The benefits of formulating a theoretical model,

or tool, which can accurately and efficiently simulate the behavior of a multibody system in a real world environment are: 1) ease of testing design iterations, and 2) reduction of manufacture time and costs. As mentioned previously, factors such as impact and friction are important to consider in the modeling process because they dictate the dissipation of energy and how a system behaves. Thus, a theoretical model offers engineers and scientists the ability to easily perform numerous simulations of a potential system design under different environment scenarios. Furthermore, theoretical simulation provides a way to improve and gain a better understanding of a system's performance, before the manufacture of a physical prototype begins. This undoubtedly induces savings in the time and cost of producing needless prototypes which may otherwise perform poorly during experimental testing.

The current field of research in multibody system dynamics lacks a framework for modeling simultaneous, indeterminate contact and impact with friction. This research develops a framework as a theoretical tool, which addresses this void in the literature. In order to understand the terminology used to classify the special class of problems examined in this research, an explanation will be given for clarification. Contact and impact is assumed to be concentrated locally at a point in the colliding region between bodies. This is the assumption followed herein, in the case of round or spherical surfaces, whereas multiple points can be used to represent the contact and impact region for flat surfaces. Simultaneous is understood to mean that a multibody system is experiencing contact and/or impact at more than one point, or multiple points, at the same instance in time. This situation is critical because it often leads to an indeterminacy in the system equations of motion with respect to the contact and impact forces; this is especially true when friction is considered at the contact and impact points. The indeterminate nature of the system equations of motion is one of the key issues this research addresses.

Consider by way of example, the planar model of a ball with radius R, shown in Fig. 1.2a. This planar system has three degrees-of-freedom (DOFs) with respect to an inertial reference frame **N** denoted by generalized coordinates q_1, q_2 and q_3, which imply three equations of motion. For the purpose of demonstration, only two impact points are considered with friction, such that there are four unknown impact forces, f_{t1}, f_{n1}, f_{t2}, and f_{n2} in Fig. 1.2b; the subscripts n and t distinguish between normal and tangential terms. Here, the consideration of friction at the two impact points introduces tangential forces, which lead to indeterminate equations of motion with respect to the impact forces. Additional impact points can be considered but only two are needed to introduce the indeterminate issue.

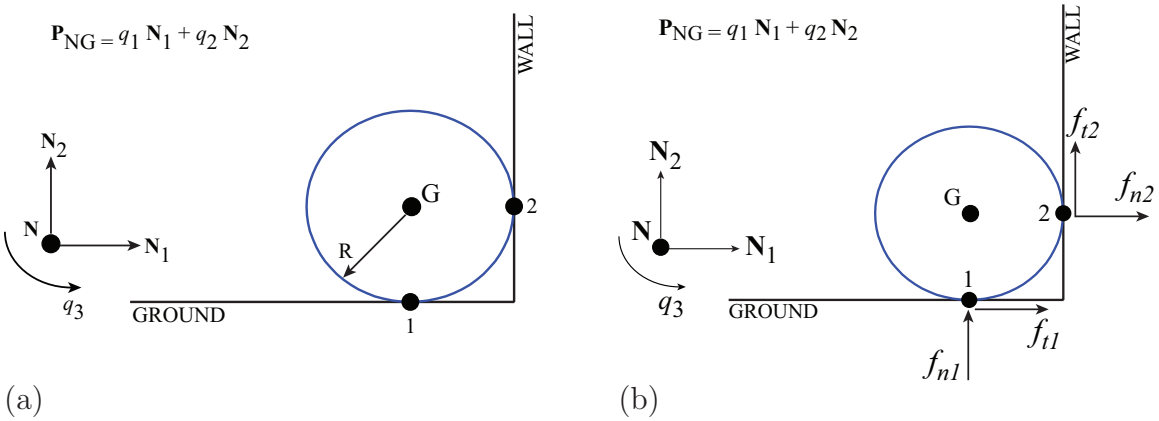

Figure 1.2. (a) Planar model of a ball example and (b) velocities and forces at impact points 1 (ground) and 2 (wall).

Multiple point contact and impact is further used here to stress two common situations encountered. The first deals with the fact that a multibody system may undergo contact and impact at multiple points (i.e. a biped robot may have simultaneous contact and impact with its feet and hands). The second situation suggests

that a contact or impact surface can be approximated by the definition of multiple points on the body of interest in the system, as in the case of a flat surface. Combining simultaneous and indeterminate introduces the specific class of contact and impact problems examined in this research. The consideration of friction complicates the modeling of these problems but adds value to the developed framework because it is necessary to represent the actual characteristics encountered by a real world system.

In the initial stages of this research, an iterative method, which incorporated an optimization function was used to obtain numerical solutions for the collisions simulated [9, 10, 11, 12]. The implementation of velocity constraints were first developed using rigid body assumptions and Newton's coefficient of restitution was used. The numerical method was later replaced with an analytical approach using Stronge's energetic coefficient of restitution (ECOR) in conjunction with the constraint formulation in an effort to improve the time and accuracy of the solutions obtained for planar systems [13, 14, 15, 16]. Experimental validation was used in this work to demonstrate that the developed framework makes a significant impact in the field of multibody system dynamics.

1.3 Research Contributions

In Chapter 3, the indeterminate contact and impact problem is addressed by deriving velocity constraints among the impact points, which are consistent with rigid body assumptions. A general method for obtaining these constraints is demonstrated for an arbitrary configuration of impact points. These velocity constraints are further derived in terms of forces at the impact points using the dual properties of the impact Jacobian. The projection of these constraints between velocity– and force-spaces are proven to give physically meaningful constraints that are consistent with the rigid body modeling approach used in this research.

Chapter 4 discusses the restitution coefficient applied to account for the energy dissipated normal to the impacting bodies. The work done on the system is determined from the Work-Energy Theorem by isolating the components of this calculation that contribute to the normal work. This work is used in conjunction with Stronge's ECOR, which is reinterpreted in the developed framework to represent the *global* energy loss for the impact events analyzed. The theory of Stronge's ECOR is further generalized to treat multiple point impact problems, which incorporates the rigid body constraints developed in Chapter 3 to address indeterminate contact and impact.

In Chapter 5, the analytical framework for treating two-dimensional (or planar) indeterminate contact and impact problems with friction is developed. The analytical framework accounts for the complex slip behaviors of an impact point due to the consideration of friction, such as slip-reversal, sticking, and slip-resumption. A method for checking the no-slip condition, which also incorporates the rigid body constraints developed in Chapter 3 is derived to visualize the regions defined by the no-slip condition for an impact point.

The treatment of three planar example problems with multiple case studies are analyzed using the developed analytical framework in Chapter 6. Several important conclusions are made from the simulation results obtained, including: the interpretation of the ECOR for multiple point impact problems, defining the range of values for the ECOR, the observation of multiple impact events captured for a single collision, and using experimental validation from the simulation results for a frictionless rocking block and three-ball Newton's Cradle.

Chapter 7 presents an extension of the methods used in the analytical framework of Chapter 5 to develop the numerical framework for treating 3D multiple point impact problems with friction. The derivation of rigid body constraints is shown in differential

form for an arbitrary configuration of impact points. The method for deriving these constraints can be generalized for the consideration of additional impact points. An event-based scheme is implemented to address the discontinuity that is encountered at the stick-slip transition for 3D impact problems.

In Chapter 8, a further study is performed on two 3D example problems with multiple cases to test the numerical framework developed in Chapter 7. The total number and configuration of the impact points are varied to gain some insight about the effects in behavior of a 3D rocking block problem with friction, as an equivalent foot-ground interaction. The analysis of these 3D multiple point impact problems demonstrates the effectiveness of the novel method developed in this research for addressing indeterminate contact and impact.

Chapter 2

Contact and Impact Modeling

2.1 Contact Models

Contact and impact of multibody systems has been extensively studied in the literature due to its complex physical nature. There are many different approaches which are used in an attempt to approximate the abrupt interaction between two colliding bodies. Rigid body impacts occur over a very short time period and are commonly characterized by rapid changes in the system velocities and the presence of large forces on the bodies.

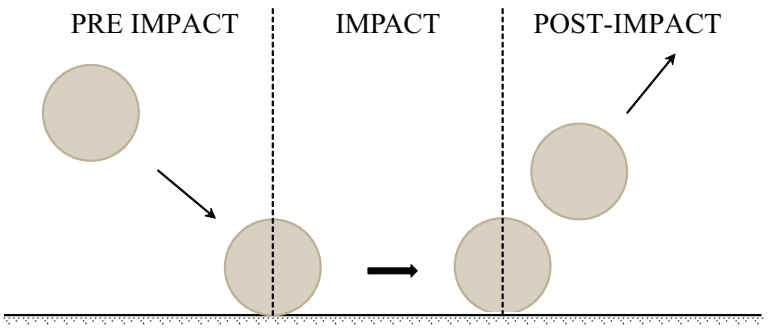

Figure 2.1. Pre– and post-impact regions for discrete modeling approach.

The two most common approaches used to treat rigid body impacts involve a continuous or discontinuous method. In this work, the rigid body impacts are modeled as discrete events using a discontinuous approach, as depicted in Fig. 2.1. This approach, also termed as piecewise [17], nonsmooth [18], or impact and continuous [19], characterizes the impact as an instantaneous change in the velocities of the

impacting bodies and impulse-momentum theory is used to treat the hard impacts [20, 21]. The large impact forces are generated by very small local deformations when a rigid body impact is assumed [3]. It is assumed that the impact event occurs over a very short time period in which the position and orientation of the system remains constant, which establish the Darboux-Keller impact dynamics [22, 23]. Figure 2.1 illustrates how this discrete approach defines a pre– and post-impact region with an impact region that is assumed to be instantaneous. This approach is used in this work and the short impact event is further treated as a continuous process, and examined in the impulse-domain, as in [24, 25, 26] when the bodies are still in contact; here, contact is treated as a succession of discrete impact events. A discrete, algebraic approach is used to define enough equations to describe the system such that the post-impact velocities are solved algebraically [27, 28]. These velocities dictate the dynamic behavior of the system after impact.

An alternative to discrete approaches are continuous approaches, which use regularized [17], non-colliding [19], or compliant [29, 30] contact force models, and often involve penalty methods. These models use the theory of elasticity and incorporate the properties of stiff springs and/or dampers [31, 32] to model the impact. Some of the first models proposed developed a relationship between the local deformations and the time-varying forces on the bodies [33, 31, 34].

2.2 Friction Models

In order to develop a better understanding of the interactions between multi-body systems and their surroundings, this work examines the effects of friction during contact and impact. Continuous friction laws have been proposed and subsequently modified, such as the LuGre [35, 36], Iwan [37] and Dahl [38] friction model. The LuGre friction model uses the basis of bristles to account for the changing friction

force with slipping velocity. Alternatively, the Iwan friction model is associated with modeling the frictional impact using elastic-perfectly plastic theory, while the Dahl friction model examines the behavior as a hysteretic force-displacement using differential analysis. Other approaches incorporate a maximum dissipation principle which is used in conjunction with friction models to produce a physically accurate depiction of friction behavior [27, 39].

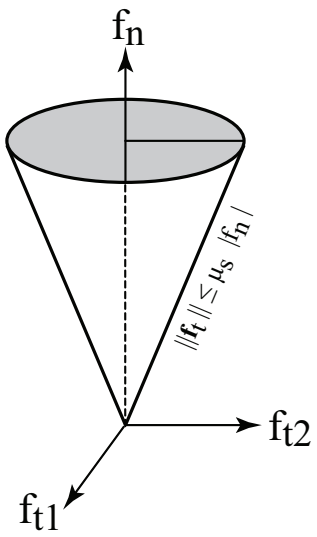

Figure 2.2. Friction cone based on theory of Coulomb friction.

Researchers Banerjee, Bauchau et al. in [40, 41], present a modification to the Coulomb friction model was applied using regularization factors which produced a continuous friction law. This approach smooths the transition between slipping and sticking regions but lacks a physical meaning to the parameters used in the model. Even though these continuous friction laws attempt to avoid the discontinuity, which arises from modeling friction, the discontinuous friction model of Coulomb's law proves to be very useful for multibody impact problems. Coulomb friction is used in the framework developed to relate the tangential impulse to the normal impulse

by a coefficient of friction (COF) [42]. This relationship can be visualized using the friction cone for Coulomb friction, depicted in Fig. 2.2. As mentioned before, the friction force might be discontinuous because changes in the friction direction during an impact event can occur due to sliding or sticking – a dynamic, μ_d or static, μ_s, COF may be used, respectively.

The choice between μ_d and μ_s depends on the slip-state of an impact point. Herein, the slip-state of an impact point refers to whether an impact point is sticking (no-slip) or sliding (slipping). The inner region of the friction cone represents sticking, whereas the outer region is sliding. The boundary of the friction cone between these two regions is the stick-slip transition where an impact point with initial sliding comes to rest and then resumes slip, slip-reverses or remains in the stick region [21, 43]. The conditions that will determine the outcome from the stick-slip transition are discussed in the following section. The lower bound on COF which induces sticking is represented by the critical COF, $\bar{\mu}$. Thus, it is necessary in this research to closely examine the stick-slip transition because it will ultimately affect the post-impact state a system will reach. This theory is developed and applied to dynamic, multibody systems undergoing indeterminate, multiple point impact with friction.

2.3 Complementarity Conditions

The stick-slip transition is best defined in relation to the well-known complementarity conditions, which describe the relationships between friction, contact forces, velocities, and accelerations [27]. Assuming that the distance between the impacting points equals zero, the complementarity conditions are dependent on the value of the pre-impact normal velocity and acceleration as,

$$\begin{cases} v_{ni}(t) < 0 & \text{impact or contact} \\ v_{ni}(t) = 0 \quad \text{and} & \begin{cases} \dot{v}_{ni}(t) \leq 0 & \text{contact} \\ \dot{v}_{ni}(t) > 0 & \text{separation} \end{cases} \\ v_{ni}(t) > 0 & \text{separation} \end{cases} \tag{2.1}$$

A transition between being in and out of contact or impact occurs when the pre-impact normal velocity equals zero. The pre-impact acceleration must be checked to determine whether impact forces will exist. According to classical Coulomb friction, the post-impact tangential velocities satisfy,

$$\begin{cases} \boldsymbol{v}_{ti} = \mathbf{0} \text{ and } \dot{\boldsymbol{v}}_{ti} = \mathbf{0} & \text{then} \quad \|\mathbf{f}_{ti}\| \leq \mu_s \, |\mathrm{f}_{ni}| & \text{sticking} \\ \boldsymbol{v}_{ti} = \mathbf{0} \text{ and } \dot{\boldsymbol{v}}_{ti} \neq \mathbf{0} & \text{then} \quad \|\mathbf{f}_{ti}\| = \mu_s \, |\mathrm{f}_{ni}| & \text{stick-slip transition} \\ \boldsymbol{v}_{ti} \neq \mathbf{0} & \text{then} \quad \|\mathbf{f}_{ti}\| = \mu_d \, |\mathrm{f}_{n_i}| & \text{slipping} \end{cases} \tag{2.2}$$

where μ_s and μ_d are the static and dynamic coefficients of friction [27].

The no-slip condition is defined by the first relation in (2.2), the stick-slip transition is defined by the second, and slipping, or sliding is defined by the third. In (2.2) there is a discontinuous change in the coefficient of friction, assuming $\mu_s \neq \mu_d$, and thus a discontinuous change in the friction forces. This discontinuity defines an abrupt transition from sticking to slipping, a state often referred to as *impending motion*. Once the impact point overcomes the static friction force, or stiction, it begins to slip and the coefficient of friction drops discontinuously from μ_s to μ_d.

The relationships in Eqns. (2.1) and (2.2) are the basis for what is referred to as a complementarity problem [44]. The complementarity conditions apply to both contact and impact forces independently. Other friction models have been proposed which provide a continuous transition between sticking and slipping including the Karnopp model [45, 46]. Herein, impulsive forces are used to check the sticking

condition. The complementarity conditions in terms of impulses are presented in [47],

$$\begin{cases} \boldsymbol{v}_{ti} = \mathbf{0} \text{ and } \dot{\boldsymbol{v}}_{ti} = \mathbf{0} & \text{then} \quad \|\mathbf{p}_{ti}\| \leq \mu_s \ |\mathrm{p}_{ni}| \ \text{ sticking} \\ \boldsymbol{v}_{ti} = \mathbf{0} \text{ and } \dot{\boldsymbol{v}}_{ti} \neq \mathbf{0} & \text{then} \quad \|\mathbf{p}_{ti}\| = \mu_s \ |\mathrm{p}_{ni}| \ \text{ stick-slip transition} \\ \boldsymbol{v}_{ti} \neq \mathbf{0} & \text{then} \quad \|\mathbf{p}_{ti}\| = \mu_d \ |\mathrm{p}_{ni}| \ \text{ slipping} \end{cases} \tag{2.3}$$

Similar complementarity conditions can be developed for moments [48, 49].

2.4 Event-Based Simulation Technique

The two-dimensional and three-dimensional examples studied in this work are simulated using an adaptive Runge-Kutta integrator, which employs the Dormand-Prince method [50]. This integrator is needed to solve the equations of motion when the systems are simulated using the discrete approach for the pre– and post-impact simulations. In order to evaluate the integrity of the simulations performed, a check function is used which is based on the Work-Energy Theorem. This check function is calculated as,

$$check_{1,i} \ = \ T_i \ - \ (T_1 \ + \ W_{1\rightarrow i}) \tag{2.4}$$

where T_i and T_1 are the kinetic energies at the i^{th} and first iteration step of the integration, respectively, and $W_{1\rightarrow i}$ is the work done by generalized active forces, such as conservative and non-conservative, throughout the integration. Figure 2.3 illustrates this check function plotted versus the simulation time. Ideally, the check function should remain constant and close to zero. Otherwise, increases or decreases in this value indicate dynamic inconsistencies in the simulation process.

The use of collision detection algorithms are available in the literature, see [51, 52, 53]. Here, an event-driven scheme, similar to [39, 54] in conjunction with Matlab's *ode45* integrator stops the simulation when a collision is detected. Multiple

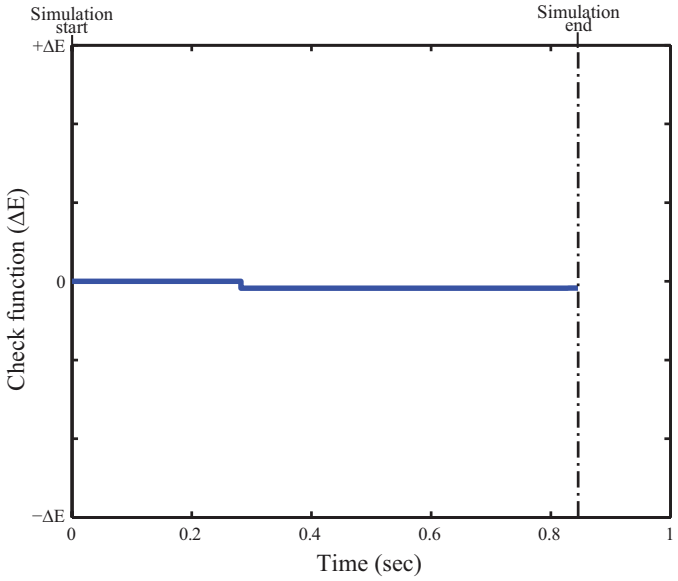

Figure 2.3. Check function of numerical integration for simulation.

impact events can occur in the collisions simulated. This is further discussed in the examples simulated. The developed approach is used to treat the impact events and determine the post-impact velocities of the system. These velocities serve as the initial conditions when the simulation is restarted. This technique is followed herein each time a collision is detected in the simulations conducted.

A process flow chart is presented in Fig. 2.4 to illustrate the operations performed during a simulation. This is true for the planar and 3D multiple point impact problems studied using the analytical-numerical framework developed in this research. The type of algorithm shown in Fig. 2.4 is commonly used in multibody dynamics simulation [19].

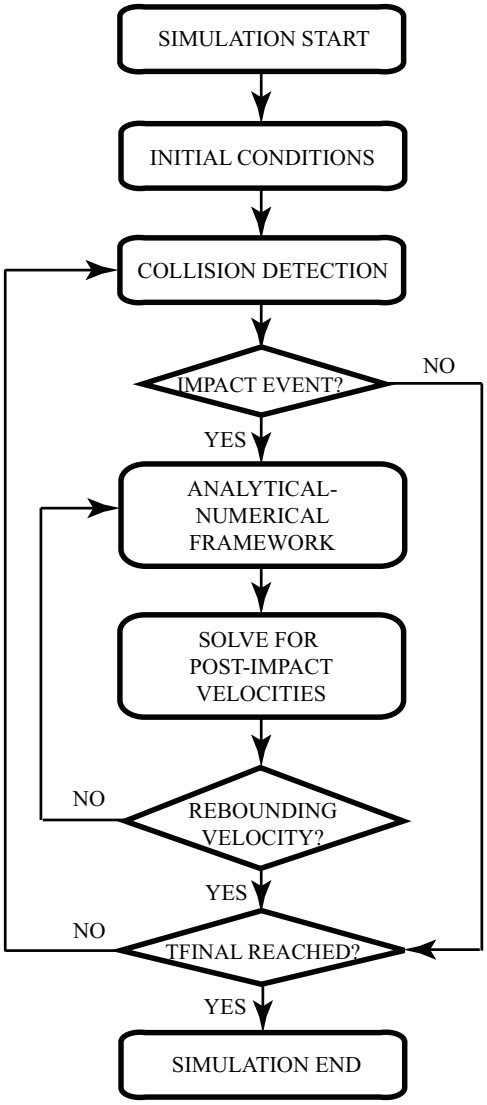

Figure 2.4. Flow process used for the simulation of impact problems.

Chapter 3

Indeterminate Contact and Impact

3.1 Simultaneous, Multiple Point Impact

The central problem addressed in this work is the dynamic modeling of systems involving simultaneous, multiple point impact with friction which yield equations of motion that are indeterminate with respect to the impact forces [55, 56, 57, 58, 9, 10, 12]. This is problematic because the impact forces are needed to determine the slip-state of the impacting point. The simultaneous aspect of the rigid body impacts encountered separates the problem from simply multiple frictional impacts studied by other researchers [59, 60, 29, 61].

The indeterminacy in the equations of motion was first addressed in this research, see [9, 10], where velocity constraints were derived based on rigid body assumptions and applied at the velocity level. This method was used in conjunction with an optimization technique to solve for the post-impact velocities of the system. An alternative method in the literature is to add more DOFs to the problem by considering elasticity in the bodies, as in [55]. Adding more DOFs generates additional equations of motion so that the system is no longer indeterminate. Another technique involves a QR decomposition of the Jacobian's transpose to determine the impact force components which have the least effect on the system [56]. Works in robotic grasping eliminate infeasible force solutions based on the situation-specific contact geometry of a grasped object to solve the indeterminate equations [57, 58].

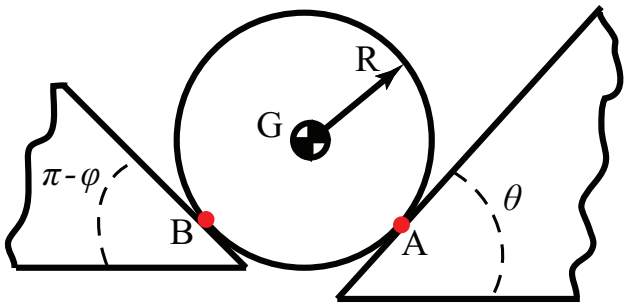

Figure 3.1. Planar ball model with two arbitrary impact points A and B.

In this work, velocity constraints are derived from the kinematic relationship between the impact points but unlike [9, 10, 12], the constraints are applied at the force level by using the dual properties of the impact Jacobian. This is supported by the assumption that the system configuration remains constant in the short time span of the collision, which implies that the impact Jacobian is also constant during the impact event. These aspects of the analysis allow a conversion of physically meaningful velocity constraints into force constraints.

3.2 Rigid Body Constraints

Consider, by way of example, two arbitrary impact points (A and B), located on a planar rigid body, as shown in Fig. 3.1. Using classical rigid body dynamics [62], the difference between the velocities of these two impact points is found as,

$$\mathbf{v}_A \; - \; \mathbf{v}_B \; = \; \boldsymbol{\omega} \; \times \; (\mathbf{P}_{GA} \; - \; \mathbf{P}_{GB}) \tag{3.1}$$

where $\boldsymbol{\omega}$ is the angular velocity of the body and $\mathbf{P}_{Gi}$ is the position vector of impact point i with respect to the body's mass center. If the dot product of the unit direction

between impact points A and B is applied to each side of (3.1), such that the right-hand side is zero, then the rigid body assumption defines that,

$$(\mathbf{v}_A \ - \ \mathbf{v}_B) \cdot \frac{\mathbf{P}_{GA} \ - \ \mathbf{P}_{GB}}{|\mathbf{P}_{GA} \ - \ \mathbf{P}_{GB}|} \ = \ 0 \tag{3.2}$$

yields,

$$(-sin\phi \ cos\theta + cos\phi \ sin\theta)v_{t,A} \ + \ (1 - cos\phi \ cos\theta - sin\phi \ sin\theta)v_{n,A}$$

$$+ \ (-sin\theta \ cos\phi + cos\theta \ sin\phi)v_{t,B} + (cos\theta \ cos\phi + sin\theta \ sin\phi - 1)v_{n,B} \ = \ 0 \tag{3.3}$$

where the subscripts n and t correspond to the normal and tangential velocity components of the impact point.

For the benchmark example presented in Ch. 1 of a planar ball, $\theta = \pi/2$ and $\phi = \pi$, such that,

$$v_{t,A} \ + \ v_{n,A} \ - \ v_{t,B} \ - \ v_{n,B} \ = \ 0 \tag{3.4}$$

or,

$$v_{t1} \ + \ v_{n1} \ - \ v_{t2} \ - \ v_{n2} \ = \ 0 \tag{3.5}$$

where the subscripts n and t distinguish between normal and tangential velocities. Additional rigid body constraints can be formulated using the method of (3.2) with the consideration of more impact points. The benefit is clear from the simple nature of (3.2) and permits the definition of a kinematic relationship among a collection of impact points on a rigid body.

Similarly, the general form of the constraints can be formulated, by way of example, for three impact points (B, C, and D) on a three-dimensional model of a spherical ball, as shown in Fig. 3.2.

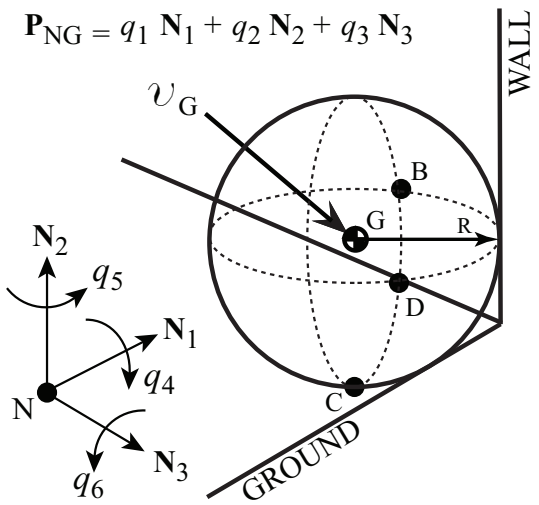

Figure 3.2. Three dimensional model of a sphere impacting a corner.

If the velocity of the sphere's center of mass at point G is known, $\boldsymbol{v}_G$, with respect to an inertial reference frame, then the velocity of point B and C shown in Fig. 3.2 are found as,

$$\boldsymbol{v}_B \;=\; \boldsymbol{v}_G \;+\; \boldsymbol{v}_{GB} \;=\; \boldsymbol{v}_G \;+\; \boldsymbol{\omega} \times \mathbf{P_{GB}} \tag{3.6}$$

$$\boldsymbol{v}_C \;=\; \boldsymbol{v}_G \;+\; \boldsymbol{v}_{GC} \;=\; \boldsymbol{v}_G \;+\; \boldsymbol{\omega} \times \mathbf{P_{GC}} \tag{3.7}$$

where $\boldsymbol{v}_{GB}$ is the relative velocity between points G and B and $\boldsymbol{v}_{GC}$ is the relative velocity between points G and C [62]. Eliminating $\boldsymbol{v}_G$ from the relations in (3.6) yields

$$\boldsymbol{v}_B \;-\; \boldsymbol{v}_C \;=\; \boldsymbol{\omega} \times (\mathbf{P_{GB}} \;-\; \mathbf{P_{GC}}) \tag{3.8}$$

where,

$$\boldsymbol{\omega} \;=\; (\dot{q}_4 + s_5\;\dot{q}_6)\;\mathbf{N_1} \;+\; (c_4\;\dot{q}_5 - s_4\;c_5\;\dot{q}_6)\;\mathbf{N_2} \;+\; (s_4\;\dot{q}_5 + c_4\;c_5\;\dot{q}_6)\;\mathbf{N_3} \tag{3.9}$$

using short-hand notation for the *sin* and *cos* terms. The result in (3.8) gives three independent equations, which are used to derive a relationship among the impact points. If the dot product of the unit direction between impact points B and C is

applied to each side, such that the right-hand side of (3.8) is zero, then the rigid body constraint is expressed as,

$$(\boldsymbol{v}_B \; - \; \boldsymbol{v}_C) \cdot \frac{(\mathbf{P_{GB}} \; - \; \mathbf{P_{GC}})}{|(\mathbf{P_{GB}} \; - \; \mathbf{P_{GC}})|} \; = \; 0 \tag{3.10}$$

such that,

$$v_{n,B} \; + \; v_{t1,B} \; - \; v_{t1,C} \; - \; v_{n,C} \; = \; 0 \tag{3.11}$$

where the subscripts n and t once again distinguish between normal and tangential velocities. The constraint in (3.11) is easily related to the planar case presented if points 1 and 2 are substituted for B and C in (3.11) to achieve the result in (3.5). Similar expressions are obtained among the other impact points such that a total of three constraints are formulated.

$$v_{n,B} \; - \; v_{t2,B} \; - \; v_{t1,D} \; + \; v_{n,D} \; = \; 0 \tag{3.12}$$

$$v_{n,C} \; + \; v_{t2.C} \; - \; v_{t2,D} \; - \; v_{n,D} \; = \; 0 \tag{3.13}$$

In this way, the rigid body assumption has allowed for the definition of three constraints which can be applied to the equations of motion to make them determinate.

3.3 Constraint Projection

The dual nature of the impact Jacobian expresses the relationship between velocities and forces,

$$\boldsymbol{\vartheta} \; = \; \begin{bmatrix} v_{t1} \\ v_{n1} \\ v_{t2} \\ v_{n2} \end{bmatrix} \; = \; J \; \dot{\mathbf{q}} \; , \quad \boldsymbol{\Gamma} \; = \; J^T \; \mathbf{F} \; = \; J^T \begin{bmatrix} f_{t1} \\ f_{n1} \\ f_{t2} \\ f_{n2} \end{bmatrix} \tag{3.14}$$

The question then becomes, what effect does the velocity constraint in (3.5) have on the force space? It is necessary to examine the dual nature of the velocity and force

constraint spaces. Consider an example where the term v_{t1} is constrained, without any loss of generality,

$$\boldsymbol{\vartheta} \;=\; \begin{bmatrix} v_{t1} \\ v_{n1} \\ v_{t2} \\ v_{n2} \end{bmatrix} \;=\; \begin{bmatrix} -1 & 1 & 1 \\ 1 & 0 & 0 \\ 0 & 1 & 0 \\ 0 & 0 & 1 \end{bmatrix} \begin{bmatrix} v_{n1} \\ v_{t2} \\ v_{n2} \end{bmatrix} \;=\; Q\; v^* \tag{3.15}$$

where Q is a matrix of full rank containing the velocity constraint and $\boldsymbol{\vartheta}^*$ contains the constrained velocity space. Taking the left-inverse of Q yields,

$$\boldsymbol{\vartheta}^* \;=\; \left(Q^T Q\right)^{-1} Q^T \boldsymbol{\vartheta} \;=\; Q^+ \boldsymbol{\vartheta} \tag{3.16}$$

Applying the dual property of the impact Jacobian and solving for the constrained force space, yields,

$$\boldsymbol{\Gamma} \;=\; J^T \mathbf{F} \;=\; J^T \left(Q^+\right)^T \mathbf{F}^* \tag{3.17}$$

which yields,

$$\mathbf{F} \;=\; \left(Q^+\right)^T \;\mathbf{F}^* \qquad \text{or} \qquad Q^T\;\mathbf{F} \;=\; \mathbf{F}^* \tag{3.18}$$

where Q^+ is the left-inverse of Q. The second expression in (3.18) is used to solve for $\mathbf{F}^*$ as

$$\mathbf{F}^* \;=\; Q^T\;\mathbf{F} \;=\; \begin{bmatrix} -1 & 1 & 0 & 0 \\ 1 & 0 & 1 & 0 \\ 1 & 0 & 0 & 1 \end{bmatrix} \begin{bmatrix} f_{t1} \\ f_{n1} \\ f_{t2} \\ f_{n2} \end{bmatrix} \;=\; \begin{bmatrix} -f_{t1} \;+\; f_{n1} \\ f_{t1} \;+\; f_{t2} \\ f_{t1} \;+\; f_{n2} \end{bmatrix} \tag{3.19}$$

Using this result in the first relation in (3.19) gives,

$$\begin{bmatrix} f_{t1} \\ f_{n1} \\ f_{t2} \\ f_{n2} \end{bmatrix} \;=\; \mathbf{F} \;=\; (Q^+)^T\;\mathbf{F}^* \;=\; \begin{bmatrix} -0.25 & 0.25 & 0.25 \\ 0.75 & 0.25 & 0.25 \\ 0.25 & 0.75 & -0.25 \\ 0.25 & -0.25 & 0.75 \end{bmatrix} \begin{bmatrix} -f_{t1} \;+\; f_{n1} \\ f_{t1} \;+\; f_{t2} \\ f_{t1} \;+\; f_{n2} \end{bmatrix}$$

$$= \begin{bmatrix} 0.75f_{t1} - 0.25f_{n1} + 0.25f_{t2} + 0.25f_{n2} \\ -0.25f_{t1} + 0.75f_{n1} + 0.25f_{t2} + 0.25f_{n2} \\ 0.25f_{t1} + 0.25f_{n1} + 0.75f_{t2} - 0.25f_{n2} \\ 0.25f_{t1} + 0.25f_{n1} - 0.25f_{t2} + 0.75f_{n2} \end{bmatrix} \tag{3.20}$$

such that every relation in (3.20) yields the same force constraint:

$$f_{t1} + f_{n1} - f_{t2} - f_{n2} = 0 \tag{3.21}$$

which is used to eliminate the dependent force in (3.20). Note that this process essentially can be stated as

$$\mathbf{F} = \left(Q^{+}\right)^{T} Q^{T} \mathbf{F} \tag{3.22}$$

noting that the matrix $(Q^{+})^{T} \; Q^{T}$ does not equal the identity matrix. This matrix projects $\mathbf{F}$ on the right-hand-side of (3.22) into the space orthogonal to the velocity constraint, which must equal the original $\mathbf{F}$. Technically, any vector of forces in the null space of $(Q^{+})^{T} \; Q^{T}$ can be added to the right-hand side and still satisfy (3.22). However, the development of this solution was based on the existence of left-inverses which only find a single solution. In addition, it is expected that adding constraints to a problem would select a particular single solution and not involve the problem of multiple solutions. This is further proved in Appendix A.

3.4 Summary

In this chapter, the rigid body assumptions were used to derive velocity constraints among the impact points and form the novel method for treating indeterminate contact and impact. This special class of multiple frictional impact occurs in situations where the multiple point impact is also simultaneous. A general method was developed for obtaining the rigid body constraints for an arbitrary configuration

and number of impact points considered. The velocity constraints were further derived in terms of forces at the impact points using the dual properties of the impact Jacobian. The projection of these constraints between velocity– and force-spaces were proven to produce physically meaningful constraints because they are consistent with the rigid body modeling approach used in this research.

Chapter 4

Energy Dissipation

4.1 Restitution Coefficients

Another key issue addressed in this research concerns the estimation of energy dissipation in the rigid body collisions simulated. Figure 4.1 depicts the compression and restitution (relaxation) phases a body undergoes during impact. The energy loss for an impact can be attributed to the net work done as a result of these processes. This work is not focused on predicting a coefficient of restitution (COR) by using the material properties of the impacting bodies, which is extensively done by [63, 64, 65]. Rather, the goal here is to implement classical hypotheses used in multibody dynamics, such as Newton's (velocities [66]), Poisson's (impulses [67]), and Stronge's (energy [61]) to estimate the energy dissipated. Each of these hypotheses uniquely define a COR to describe the relationship between the pre– and post-impact states of a system normal to the impacting point(s). Adjacent tangential compliances due to local deformation in the contact area are not accounted for by these hypotheses, which [68, 64, 69] finds that it may affect the COR used; this is not pursued further in this work.

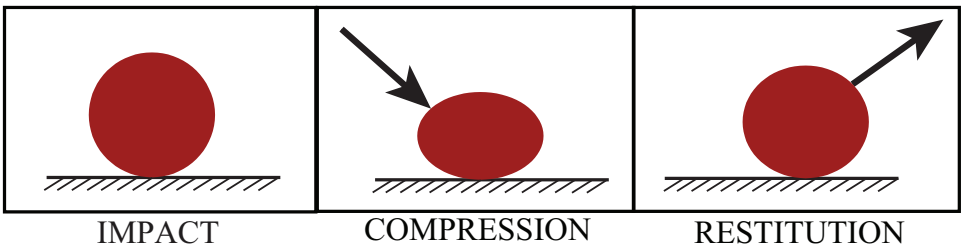

Figure 4.1. Example of compression and restitution effects on a compliant body.

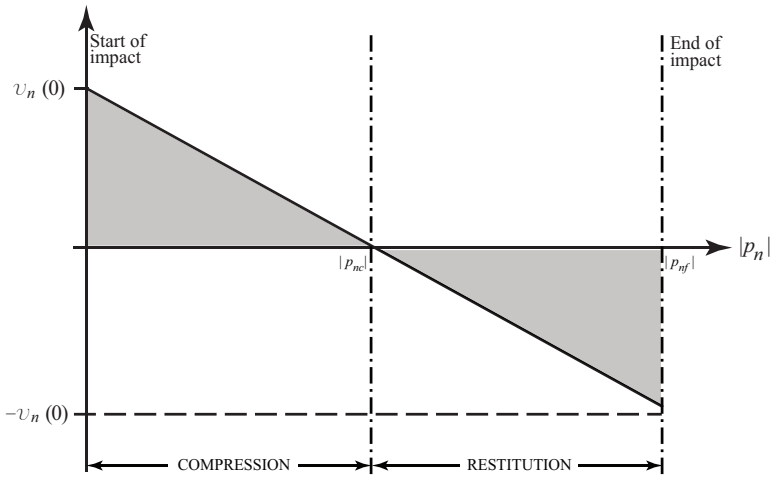

Figure 4.2. Normal velocity propagation for single point impact.

A well-known comparison of the three hypotheses is done by considering the collision process in Fig. 4.2 for a single point impact case. Newton's COR (e_n) relates the post-impact normal velocity to the pre-impact normal velocity as: $e_n = -v_n^+/v_n(0)$, where $v_n^+ = -v_n(0)$ for $e_n = 1$. Poisson's COR (e_p) relates the restitutive normal impulse to the compressive normal impulse as: $e_p = p_{nr}/p_{nc} = (p_{nf} - p_{nc})/p_{nc}$, where $p_{nr} = p_{nc}$ for $e_p = 1$. Stronge's hypothesis (e_*) relates the normal restitutive work to the normal compressive work (shaded areas in Fig. 4.2) as: $e_*^2 = -W_{nr}/W_{nc}$. Note that the compression phase ends when $v_n = 0$ for single point impact but this is not so straight forward for multiple point impact and this research aims to narrow this gap in understanding.

The differences of each COR hypothesis lie in the accuracy of representing physically consistent behavior of a system. For example, Newton's hypothesis has been noted to produce energy inconsistencies in the form of gains in mechanical energy [70, 71]. Poisson's hypothesis is useful for the solutions it gives to rigid body impact problems but lacks a foundation in physical principles [55]. Stronge's hypothesis

however, defines an energetic coefficient of restitution (ECOR) which incorporates work-energy theory, as used in [3, 25, 26], and often leads to energetically consistent results in rigid body impact modeling. The difference in this work is that the application of the ECOR is extended to model the *global* dissipation of energy for multiple point impact problems as opposed defining a local ECOR for each impact point. This global representation of energy loss eliminates the need for tangential coefficients.

The use of the ECOR requires a work-energy analysis at the system level to determine the energy dissipated from a collision [15, 16]. Even though the collisions considered here are treated as rigid body impacts, the compression and restitution phase of the work-energy analysis solely correspond to the change in kinetic energy of the system. In other words, the goal in this work is not to model the physical deformation local to the impact points. Herein, the work done by normal impulsive forces is examined in the impulse domain, as a function of an independent normal impulse parameter, which yields the invariant parabolic shape of the work-energy relationship. In addition, the evolution, or changes, of the impact velocities throughout the collision are also examined in the impulse domain. Changes in velocity directions are largely affected by the coefficient of friction when an impact point comes to rest after initial sliding. Thus, the examination of the stick-slip transition is a major focus in this work. The sign of the corresponding tangential force is opposite of the sliding direction of the impact point on the slip plane, which is represented by Coulomb friction and discussed in Sec. 2.2. This is problematic in the 3D case when the impact point goes through the stick-slip transition (i.e. $s = 0$) because the direction becomes undefined in this region. Iterative or recursive methods [25, 5, 6] work well to define this region and resolve the direction of friction.

These developments lead to a generalized interpretation of Stronge's hypothesis for multiple point collision problems with friction, which is still applicable for single

point impact problems. The methods used also lead to unique and energetically consistent solutions of simultaneous, indeterminate contact and impact problems.

4.2 Work-Energy Theory

Next, the implementation of the work-energy theorem is discussed. The calculation of the work is given as the change in kinetic energy between the initial and final states of the impact as,

$$T_2 \;=\; T_1 \;+\; W_{1-2} \;=\; T_1 \;+\; U_1 \;-\; U_2 \;+\; (W_{1-2})_d \tag{4.1}$$

where T_i and U_i are the kinetic and potential energy at state i, and $(W_{1-2})_d$ is the non-conservative, or dissipative, work done on the system between states 1 and 2. In this work, the potential energy terms U_1 and U_2 are neglected due to the hard impact assumptions, or negligible deformation, from the strict adherence to rigid body modeling.

$$W_{1-2} \;=\; W \;=\; T_2 - T_1 \;=\; \frac{1}{2}\,\dot{\mathbf{q}}^T(t+\epsilon) M\,\dot{\mathbf{q}}(t+\epsilon) - \frac{1}{2}\,\dot{\mathbf{q}}^T(t) M\,\dot{\mathbf{q}}(t) \tag{4.2}$$

Recall from (3.14) the relationship between the component velocities in $\boldsymbol{\vartheta}$ and the generalized speeds in $\dot{\mathbf{q}}$, such that the change in generalized speeds can be written as,

$$\begin{aligned} \dot{\mathbf{q}}(t+\epsilon) \;-\; \dot{\mathbf{q}}(t) \;&=\; \underbrace{(J^T J)^{-1} J^T}\, J(\;\dot{\mathbf{q}}(t+\epsilon) \;-\; \dot{\mathbf{q}}(t)\;) \\ &=\; J^+(\;\boldsymbol{\vartheta}(t+\epsilon) \;-\; \boldsymbol{\vartheta}(t)\;) \end{aligned} \tag{4.3}$$

By using the same representation of the generalized speeds $\dot{\mathbf{q}}(t+\epsilon)$ and $\dot{\mathbf{q}}(t)$ in (4.3), then (4.2) is expressed as,

$$W \;=\; \frac{1}{2}\,(\;J^+\boldsymbol{\vartheta}(t+\epsilon)\;)^T M(\;J^+\boldsymbol{\vartheta}(t+\epsilon)\;) \;-\; \frac{1}{2}\,(\;J^+\boldsymbol{\vartheta}(t)\;)^T M(\;J^+\boldsymbol{\vartheta}(t)\;) \tag{4.4}$$

where the component velocities in $\boldsymbol{\vartheta}(t+\epsilon)$ and $\boldsymbol{\vartheta}(t)$ become apparent in the calculation of the work.

The normal work done throughout an impact event is a function of the component velocities normal to each impact point. To capture the effect that the right hand side of (4.4) has on the normal work due to the normal component velocities, a distinction must be made between the contributing and non-contributing terms.

$$W = \frac{1}{2}\ \left(\ \mathbf{J}_t^+ \boldsymbol{\vartheta}_t(t+\epsilon)\ + \mathbf{J}_n^+ \boldsymbol{\vartheta}_n(t+\epsilon)\ \right)^T M \left(\ \mathbf{J}_t^+ \boldsymbol{\vartheta}_t(t+\epsilon)\ +\ \mathbf{J}_n^+ \boldsymbol{\vartheta}_n(t+\epsilon)\ \right)\ -$$

$$\frac{1}{2}\ \left(\ \mathbf{J}_t^+ \boldsymbol{\vartheta}_t(t)\ +\ \mathbf{J}_n^+ \boldsymbol{\vartheta}_n(t)\ \right)^T M \left(\ \mathbf{J}_t^+ \boldsymbol{\vartheta}_t(t)\ +\ \mathbf{J}_n^+ \boldsymbol{\vartheta}_n(t)\ \right) \qquad (4.5)$$

where $\mathbf{J}_t^+ = [\ \mathbf{J}_1^+ \mid \mathbf{J}_3^+\ ]$, $\mathbf{J}_n^+ = [\ \mathbf{J}_2^+ \mid \mathbf{J}_4^+\ ]$, and $J^+ = [\ \mathbf{J}_1^+ \mid \mathbf{J}_2^+ \mid \mathbf{J}_3^+ \mid \mathbf{J}_4^+\ ]$. The tangential and normal component velocities in (4.5) are distinguished by the terms $\boldsymbol{\vartheta}_t$ and $\boldsymbol{\vartheta}_n$. The product of the terms in (4.5) is carried out to determine the position of the normal velocity terms with respect to the tangential terms so that only the terms contributing to the normal work are extracted.

$$W\ =\ \frac{1}{2}\left(\boldsymbol{\vartheta}_t^T(t+\epsilon)\ \mathbf{J}_t^{+T}\ M\ \mathbf{J}_t^+ \boldsymbol{\vartheta}_t(t+\epsilon)\ +\ 2\ \boldsymbol{\vartheta}_t^T(t+\epsilon)\ \mathbf{J}_t^{+T}\ M\ \mathbf{J}_n^+ \boldsymbol{\vartheta}_n(t+\epsilon) + \right.$$

$$\left.\boldsymbol{\vartheta}_n^T(t+\epsilon)\ \mathbf{J}_n^{+T}\ M\ \mathbf{J}_n^+ \boldsymbol{\vartheta}_n(t+\epsilon)\right)\ -\ \frac{1}{2}\left(\boldsymbol{\vartheta}_t^T(t)\ \mathbf{J}_t^{+T}\ M\ \mathbf{J}_t^+ \boldsymbol{\vartheta}_t(t)\ +\right.$$

$$\left.2\ \boldsymbol{\vartheta}_t^T(t)\ \mathbf{J}_t^{+T}\ M\ \mathbf{J}_n^+ \boldsymbol{\vartheta}_n(t)\ +\ \boldsymbol{\vartheta}_n^T(t)\ \mathbf{J}_n^{+T}\ M\ \mathbf{J}_n^+ \boldsymbol{\vartheta}_n(t)\right) \qquad (4.6)$$

A careful look at all the terms in (4.6) shows tangential, normal, and coupled tangential and normal terms due to the multiple point impact modeling, and are indicated by $\boldsymbol{\vartheta}_t$ and $\boldsymbol{\vartheta}_n$. As it was stated earlier, the component velocities normal to the impact points primarily contribute to the normal work in an impact event. Thus, if only the terms that are a function of the normal velocities $\boldsymbol{\vartheta}_n$ are considered, then the normal work is calculated here as,

$$W_n\ =\ \left(\boldsymbol{\vartheta}_t^T(t+\epsilon)\ \mathbf{J}_t^{+T}\ M\ \mathbf{J}_n^+ \boldsymbol{\vartheta}_n(t+\epsilon)\ +\frac{1}{2}\boldsymbol{\vartheta}_n^T(t+\epsilon)\ \mathbf{J}_n^{+T}\ M\ \mathbf{J}_n^+ \boldsymbol{\vartheta}_n(t+\epsilon)\right)\ -$$

$$\left(\boldsymbol{\vartheta}_t^T(t)\ \mathbf{J}_t^{+T}\ M\ \mathbf{J}_n^+ \boldsymbol{\vartheta}_n(t)\ +\ \frac{1}{2}\boldsymbol{\vartheta}_n^T(t)\ \mathbf{J}_n^{+T}\ M\ \mathbf{J}_n^+ \boldsymbol{\vartheta}_n(t)\right) \qquad (4.7)$$

where the only unknowns are $\boldsymbol{\vartheta}_t(t+\epsilon)$ and $\boldsymbol{\vartheta}_n(t+\epsilon)$, which are the elements of the component velocities in $\boldsymbol{\vartheta}(t+\epsilon)$.

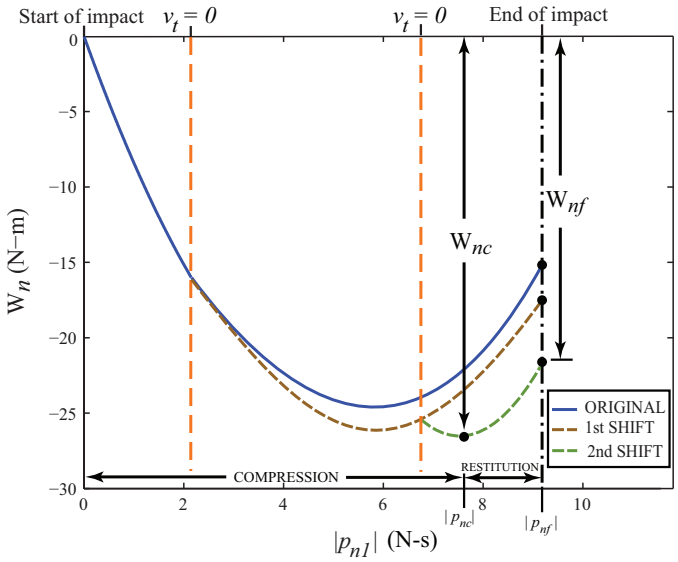

Figure 4.3. Example plot of the normal work for an impact event showing the shifts that may occur from the stick-slip transition..

From (4.7), it can be shown that the normal work is a function of the independent parameter $|p_{n1}|$ and takes the form,

$$W_n = W_n(|p_{n1}|) = a\ |p_{n1}|^2 + b\ |p_{n1}| \tag{4.8}$$

where a and b are constant coefficients. No $|p_{n1}|^0$ term, or constant, appears in (4.8), which is consistent for $|p_{n1}| = 0$ that corresponds to $W_n = 0$ at the start of an impact event, shown for example in Fig. 4.3. This plot illustrates the invariant parabolic shape of the work-energy relationship event when a discontinuity occurs, as in Fig. 4.3 at $v_t = 0$. Differentiating (4.8) with respect to $|p_{n1}|$ and setting the result equal to zero yields the normal impulse $|p_{nc}|$ at the end of the compression phase

for the system. This result is substituted back into (4.8) to evaluate the associated compressive work W_{nc} as,

$$\frac{dW_n}{d|p_{n1}|} = 2a\ |p_{n1}| + b = 0 \quad \longrightarrow \quad |p_{nc}| = -\frac{b}{2a} \tag{4.9}$$

$$W_{nc} \ = \ W_n(|p_{nc}|) \tag{4.10}$$

Note that $|p_{nc}|$ and subsequently W_{nc} may change if the end of the impact event is not reached before a subsequent point reaches the stick-slip transition, as in the case between *Shift 1* and *Shift 2* in Fig. 4.3. Similarly, if no point reaches the stick-slip transition, then no shifts occur. In the event that multiple shifts occur, then the normal work curve for the latter shift is used with the ECOR to determine the net normal work W_{nf} for the impact event as,

$$W_{nf} \ = \ W_{nc}(1 \ - \ e_*^2) \tag{4.11}$$

where (4.11) is the system normal work done and $e_* \in [-1, 1]$ is a *global* ECOR which accounts for the energy dissipated by the system in an impact event. In this work, $e_* < 0$ means that in a simultaneous, multiple point collision subsequent impact events may begin while an initial impact event has not completed its compression phase. The value of e_* is usually not known in a predictive sense, unless a good understanding of the material properties and physical behavior of the system is accounted for, as in [63, 64], which is not the goal in this work. Alternately, e_* functions more as a parameter to estimate the energy dissipated and its value in the present framework can be selected to correlate with experimental studies of an equivalent system.

As it was mentioned previously, a change in the direction of a sliding velocity in (5.6) can also create a discontinuity in the curves of the normal work plot, as shown in Fig. 4.3. As a consequence, the length of a collision is extended by increasing the compression phase, or W_{nc}. These discontinuities are addressed until a segment of

the curve includes a zero slope, which indicates the end of the compression phase and defines $|p_{nc}|$, and consequently W_{nc}, used in (4.11) to determine the end of the impact, W_{nf} and $|p_{nf}|$. In turn, this allows determination of the post-impact velocities, shown later using (5.6).

4.3 Stronge's Hypothesis For Multiple Point Impact

The compression phase end is also noted under Stronge's hypothesis to occur when the normal velocity reaches zero for single point impact, but is not as intuitive when multiple point impact is examined. A different approach to the calculation of the normal work, as in [25], is presented here to gain a better understanding of how Stronge's hypothesis is interpreted in the case of multiple point impact.

Consider the work done during a collision to be the integration of the dot product between force and displacement as,

$$\begin{aligned} W &= \int \mathbf{F}_1 \cdot d\mathbf{x}_1 + \int \mathbf{F}_2 \cdot d\mathbf{x}_2 \\ &= \int \mathbf{F}_1 \cdot d(x_{t1}\mathbf{N}_1 + x_{n1}\mathbf{N}_2) + \int \mathbf{F}_2 \cdot d(x_{n2}\mathbf{N}_1 + x_{t2}\mathbf{N}_2) \end{aligned} \quad (4.12)$$

where $\mathbf{F}_1$ and $\mathbf{F}_2$ contain the vector representations for normal and tangential forces for impact points 1 and 2. The normal work is expressed as,

$$W_n = \int f_{n1}\, dx_{n1} + \int f_{n2}\, dx_{n2} \quad (4.13)$$

and the normal forces are simply the time differentiation of the normal impulses which gives,

$$\begin{aligned} W_n &= \int dp_{n1}\frac{dx_{n1}}{dt} + \int dp_{n2}\frac{dx_{n2}}{dt} = \int v_{n1}\, dp_{n1} + \int v_{n2}\, dp_{n2} \\ &= \int v_{n1}\, |dp_{n1}| + \int v_{n2}\, |dp_{n2}| \end{aligned} \quad (4.14)$$

where the magnitude of the normal impulses is applied. This is acceptable since the the normal work done is dissipative and the normal velocities are decreasing.

Similarly, the relationship between the normal impulses C, which was presented in Sec. 3.2 for planar impact problems, is used to express (4.14) in terms of $|dp_{n1}|$,

$$W_n \;=\; \int (v_{n1} \;+\; C\; v_{n2})\;\; |dp_{n1}| \tag{4.15}$$

The significance of the normal velocities is apparent from (4.15) in the determination of the normal work during the collision. Unlike for single point impact, the end of compression phase does not occur when one normal velocity reaches zero. Rather, it is defined by the combination of normal velocities during the collision and must satisfy,

$$\frac{dW_n}{|dp_{n1}|} \;=\; v_{n1} \;+\; C\; v_{n2} \;=\; 0 \tag{4.16}$$

which is the differentiation of (4.15) with respect to $|p_{n1}|$ and set equal to zero. It should be noted that (4.16) can be simplified to treat single point impact. The result in (4.16) provides a generalized interpretation of Stronge's hypothesis for the consideration of multiple point impact with friction and applicable for the planar impact problems studied here.

4.4 Summary

An extensive comparison of restitution coefficients used in multibody dynamics was reviewed, in which Stronge's ECOR is implemented in this research to account for the energy dissipated normal to the impacting bodies. The work done on the system is determined from the Work-Energy Theorem, where the rigid body assumptions used lead to the change in kinetic energy of a system. By isolating the components of this calculation that contribute to the normal work, then the energy dissipated is evaluated in conjunction with Stronge's ECOR. It was further shown that Stronge's hypothesis was reinterpreted in the developed framework to represent the *global* energy loss for the impact events analyzed. The compression and restitution phases for a collision

were intuitive for single point impact problems (i.e. $v_n = 0$ marks the compression phase end) but this was not the case for multiple point impact problems. The theory of Stronge's ECOR was also generalized to treat multiple point impact problems, which incorporates the rigid body constraints developed in Chapter 3 to show for the case of two point impact that the compression phase end is at $v_{n1} + C\ v_{n2} = 0$. These developments can be applied to address indeterminate contact and impact problems.

Chapter 5

Two-Dimensional Impact: Analytical Framework

In this section, the details of the analytical framework are developed for a rigid body system with two impact points, by way of example but not limitation, to demonstrate the basic approach of the proposed work. Additional impact points may be considered with accompanying rigid body constraints using the general method demonstrated in Sec. 3.2 and further derived in Appendix B, as in [12, 15, 16]. The equations of motion are first expressed as a function of an independent normal impulse parameter for use with work-energy theory. These equations are then presented to consider the possible changes in slip-state of an impact point due to friction and properties of the system.

5.0.1 Equations of Motion

Examination of the impulsive forces requires a consideration of the impact forces in the equations of motion found using Kane's method [70] and shown in Appendix C,

$$M\ \ddot{\mathbf{q}}\ +\ \mathbf{b}(\mathbf{q},\dot{\mathbf{q}})\ +\ \mathbf{g}(\mathbf{q})\ =\ \mathbf{\Gamma}(\mathbf{q})\ =\ J^T(\mathbf{q})\ \mathbf{F}\ =\ J^T(\mathbf{q})\ [f_{t1}\ f_{n1}\ f_{t2}\ f_{n2}]^T \quad (5.1)$$

where M is the mass matrix, while $\mathbf{b}$ and $\mathbf{g}$ are vectors of Coriolis terms and gravity. The generalized coordinates and accelerations are included in $\mathbf{q}$ and $\ddot{\mathbf{q}}$, $\mathbf{\Gamma}$ contains the generalized active forces, and J is the *impact Jacobian matrix* that defines the configuration of the impact points. A definite integration of (5.1) over a very short time interval ϵ for the impact event,

$$\int_t^{t+\epsilon} (M\ \ddot{\mathbf{q}}\ +\ \mathbf{b}(\mathbf{q},\dot{\mathbf{q}})\ +\ \mathbf{g}\ (\mathbf{q}))\ dt\ =\ \int_t^{t+\epsilon} J^T(\mathbf{q})\ \mathbf{F}\ dt \quad (5.2)$$

yields,

$$M\ (\ \dot{\mathbf{q}}(t+\epsilon)\ -\ \dot{\mathbf{q}}(t)\ )\ =\ J^T\mathbf{p}\ =\ J^T[p_{t1}\ p_{n1}\ p_{t2}\ p_{n2}]^T \tag{5.3}$$

where the Coriolis and gravity vectors are omitted because the impact event is assumed to occur over an infinitesimally small duration ϵ in which the configuration remains constant. The terms $\dot{\mathbf{q}}(t)$ and $\dot{\mathbf{q}}(t+\epsilon)$ represent the pre- and post-impact generalized speeds.

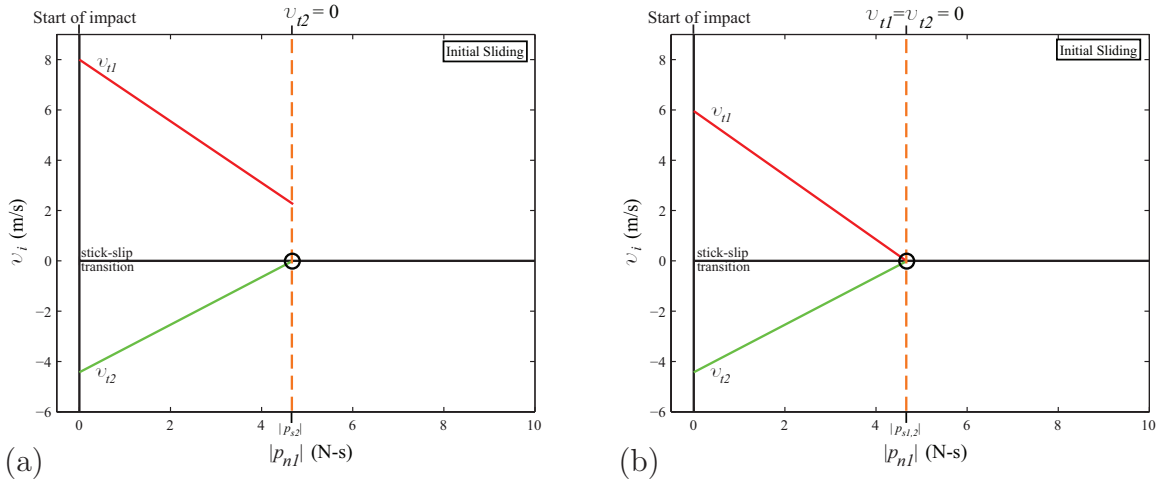

Figure 5.1. Evolution of velocities during initial sliding when (a) one point, or (b) two points come to rest.

5.0.2 Initial Sliding

It is assumed that at the start of the impact event, the tangential velocities are non-zero and therefore in a slip-state of initial sliding, as shown by way of example in Fig. 5.1. Coulomb friction is used to relate the change in the magnitude of the normal impulse to the change in tangential impulse during sliding by using a coefficient of friction μ_i for impact point i. This provides two equations, one for each impact point,

and a third equation is derived from the rigid body constraint that relates the normal impulses,

$$p_{t1} = -sgn(v_{t1})\ \mu_1\ |p_{n1}| \qquad p_{t2} = -sgn(v_{t2})\ \mu_2\ |p_{n2}| \qquad |p_{n2}| = C\ |p_{n1}| \tag{5.4}$$

where $sgn(v_{ti})$ gives the direction of friction based on the sliding velocity of impact point i. The term C is developed from the rigid body constraint on the velocity of two points attached to the same rigid body.

Solving for the post-impact generalized speeds in (5.3) and using the three equations in (5.4) yields,

$$\dot{\mathbf{q}} \ = \ \dot{\mathbf{q}}(0) \ + \ \widetilde{\mathbf{A}}_{sliding}(\mu_1, \mu_2) \cdot |p_{n1}| \tag{5.5}$$

where $\widetilde{\mathbf{A}}_{sliding}$ depends on C, which is a function of μ_1 and μ_2. Equation (5.5) gives an expression for the post-impact generalized speeds as a function of an independent normal impulse parameter, which is chosen as $|p_{n1}|$ without any loss of generality. In effect, the calculation of the generalized speeds in (5.5) is converted from the time domain to the impulse domain. The evolution of the velocities are determined by multiplying (5.5) by the impact Jacobian such that,

$$\boldsymbol{\vartheta} \ = \ \boldsymbol{\vartheta}(0) \ + \ \mathbf{A}_{sliding}(\mu_1, \mu_2) \cdot |p_{n1}| \tag{5.6}$$

where $\mathbf{A}_{sliding}$ represents the conditions for initial sliding and depends on C, which is a function of μ_1 and μ_2.

During initial sliding, (5.6) is used with $\mu_i = \mu_d$, the dynamic coefficient of friction, at impact point i to model the evolution of velocities as the impulsive normal force monotonically increases in the impact event, seen for example in Fig. 5.1. Note that only the tangential velocities appear in the plot to underscore their importance in the consideration of the stick-slip transition. If v_{t1} continues its state of initial,

or forward sliding (FS), and v_{t2} comes to rest at $|p_{n1}| = |p_{s2}|$, as in Fig. 5.1a, it is necessary to evaluate the slip-state to determine the subsequent evolution of the velocities. Similarly, it is possible that both v_{t1} and v_{t2} come to rest at $|p_{n1}| = |p_{s1,2}|$, as shown in Fig. 5.1b. When one and/or two points come to rest at the stick-slip transition, there are three possible outcomes: slip resumption (R), slip-reversal (S-R) and sticking (S), which are shown in Fig. 5.2. The next four sections discuss the treatment of the stick-slip transition to determine whether slip resumption, slip-reversal or sticking will occur, and how (5.6) is modified to reflect the new slip-state of the impact points.

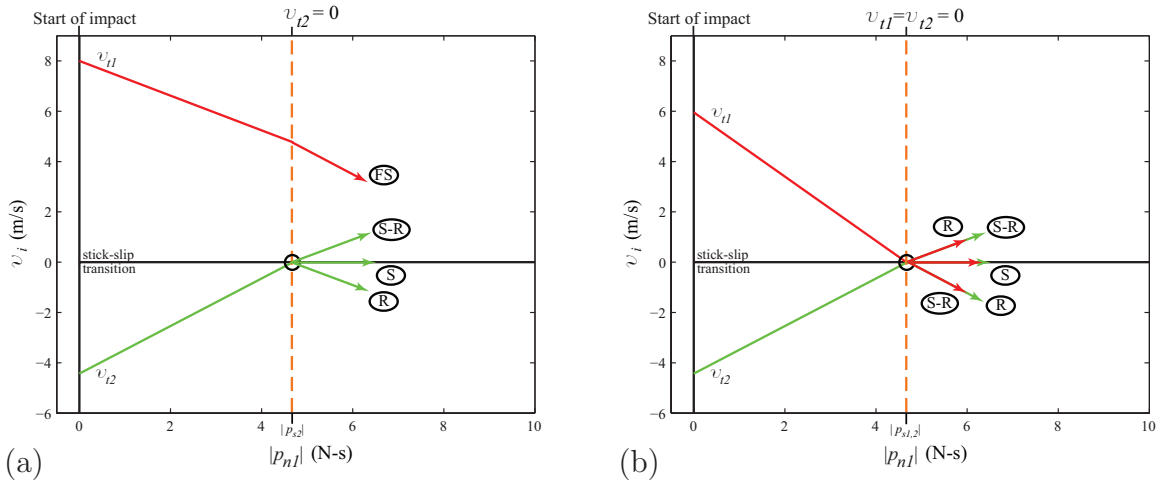

Figure 5.2. Typical friction behaviors after the stick-slip transition if (a) one point, or (b) two points come to rest.

5.1 Evaluating the Stick-Slip Transition (ST)

Consider, by way of example, the case in Fig. 5.2a where only impact point 2 comes to rest, $v_{t2} = 0$, at $|p_{s2}|$. The evolution of velocities in (5.6) in this case become,

$$\boldsymbol{\vartheta} \;=\; \begin{bmatrix} v_{t1}(|p_{s2}|) \\ v_{n1}(|p_{s2}|) \\ 0 \\ v_{n2}(|p_{s2}|) \end{bmatrix} \;+\; \mathbf{A}_{ST}(\mu_1, \bar{\mu}_2) \cdot (|p_{n1}| \;-\; |p_{s2}|) \;\;, \qquad v_{t2} \;=\; 0 \;=\; A_{3,ST}(\mu_1, \bar{\mu}_2) \tag{5.7}$$

where $\mathbf{A}_{ST}(\mu_1, \bar{\mu}_2)$ defines the conditions at the transition stage of the impact and $\bar{\mu}_2$ is the critical coefficient of friction for stick for point 2. Setting $v_{t2} = 0$ is equivalent to the third element of $\mathbf{A}_{ST}(\mu_1, \bar{\mu}_2)$ equal to zero, which yields $\bar{\mu}_2$ from the second equation in (5.7). For the impact point to remain in stick, $\bar{\mu}_2 \leq \mu_2$. If this condition is not met, then the impact point will resume slip or slip-reverses.

Another possible scenario is where both impact points come to rest at the impulse $|p_{s1,2}|$, as shown in Fig. 5.2b. The evolution of velocities in (5.6) in this case become,

$$\boldsymbol{\vartheta} \;=\; \begin{bmatrix} 0 \\ v_{n1}(|p_{s1,2}|) \\ 0 \\ v_{n2}(|p_{s1,2}|) \end{bmatrix} + \mathbf{A}_{ST}(\bar{\mu}_1, \bar{\mu}_2) \cdot (|p_{n1}| - |p_{s1,2}|) \;\;, \qquad \begin{aligned} v_{t1} \;&=\; 0 \;=\; A_{1,ST}(\bar{\mu}_1, \bar{\mu}_2) \\ v_{t2} \;&=\; 0 \;=\; A_{3,ST}(\bar{\mu}_1, \bar{\mu}_2) \end{aligned} \tag{5.8}$$

where $\bar{\mu}_1$ and $\bar{\mu}_2$ are the critical coefficients of friction for stick for point 1 and 2, respectively. Setting $v_{t1} \;=\; v_{t2} \;=\; 0$ yields $\bar{\mu}_1$ and $\bar{\mu}_2$ from the second and third equations in (5.8). Similar to the previous case, for an impact point to remain in stick, $\bar{\mu}_1 \leq \mu_1$ and $\bar{\mu}_2 \leq \mu_2$. If one or both conditions are not met, then the respective impact point will resume slip or slip-reverse.

5.1.1 Slip Resumption (R)

Slip resumption is not commonly encountered in rigid body impact but results from a model with a large coefficient of friction ($\mu_i > 1$) and unbalanced configurations (i.e. eccentric impacts), as noted by [26, 72, 24]. The imbalance between the mass center and impact point results in a positive acceleration of the impact point that leads to slip resumption, which is recognized in the Painlevé problem [73]. To determine if the configuration is unbalanced, consider the matrix $JM^{-1}J^T$ used to form $\mathbf{A}_{sliding}(\mu_1, \mu_2)$,

$$\mathbf{A}_{sliding}(\mu_1, \mu_2) \;=\; (JM^{-1}J^T)\;\widehat{C}(\mu_1, \mu_2)\;[1 \;\; C]^T \cdot |p_{n1}| \tag{5.9}$$

where $\widehat{C}(\mu_1, \mu_2)$ is a matrix containing the Coulomb friction relations. The elements $a_{12} = a_{21}$ and $a_{34} = a_{43}$ in the matrix $JM^{-1}J^T$ are used to determine the configuration balance of a system [26, 72, 24] because they correspond to the inertia and configuration properties of impact points 1 and 2, respectively. If a_{12}, $a_{34} < 0$, then the configuration is unbalanced and slip-resumption will occur. Otherwise, if a_{12}, $a_{34} = 0$, then the configuration is balanced, and configurations with a_{12}, $a_{34} > 0$ will result in slip-reversal which is discussed in the following section.

5.1.2 Slip-Reversal (S-R)

In the event that v_{t2} comes to rest and slip-reversal occurs, then the direction of slip changes, such that $\bar{\mu}_2 = -\mu_2$ in (5.7),

$$\boldsymbol{\vartheta} \;=\; \begin{bmatrix} v_{t1}(|p_{s2}|) \\ v_{n1}(|p_{s2}|) \\ 0 \\ v_{n2}(|p_{s2}|) \end{bmatrix} \;+\; \mathbf{A}_{S-R}(\mu_1, -\mu_2) \cdot (|p_{n1}| \;-\; |p_{s2}|) \tag{5.10}$$

where $\mathbf{A}_{S-R}(\mu_1, -\mu_2)$ represents the conditions for slip-reversal of point 2. Equation (5.10) describes how the velocities evolve after $|p_{s2}|$. The condition for v_{t1} remains unchanged since it continues its state of initial, or forward sliding. The change in sign of μ_2 introduces a discontinuity in the model, which is represented by a change in slope in the evolution of all the velocities; Fig. 5.2a only depicts the change in slope for the tangential velocities.

Similarly, if two points reach the stick-slip transition and slip-reversal occurs for both impact points, then the signs of the coefficient of friction change in (5.8), such that $\bar{\mu}_1 = -\mu_1$ and $\bar{\mu}_2 = -\mu_2$,

$$\boldsymbol{\vartheta} \;=\; \begin{bmatrix} 0 \\ v_{n1}(|p_{s1,2}|) \\ 0 \\ v_{n2}(|p_{s1,2}|) \end{bmatrix} \;+\; \mathbf{A}_{S-R}(-\mu_1, -\mu_2) \cdot (|p_{n1}| \;-\; |p_{s1,2}|) \tag{5.11}$$

where $\mathbf{A}_{S-R}(-\mu_1, -\mu_2)$ represents the conditions for slip-reversal of points 1 and 2.

5.1.3 Sticking (S)

The alternative to slip-reversal is stick. For the example in which v_{t2} remains in stick after the stick-slip transition, its velocity will remain equal to zero until the no-slip condition in (2.3) is violated. The Coulomb friction relation in (5.4) for point 2 no longer describes the relationship between the normal and tangential friction force, which was used to develop (5.6) and subsequently (5.7). In the case of stick, this relationship is represented by the critical coefficient of friction, for example $\bar{\mu}_2$

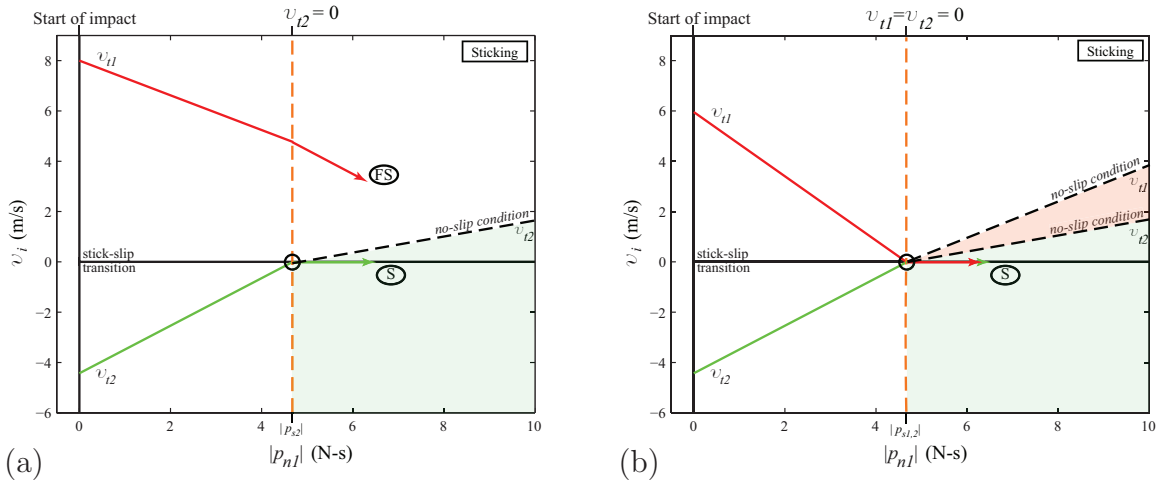

Figure 5.3. Check of the no-slip condition in (2.3) for (a) one point using (5.13), or (b) two points using (5.15) for stick after the stick-slip transition.

obtained from the second equation in (5.7), such that the evolution of velocities are described by,

$$\boldsymbol{\vartheta} \;=\; \begin{bmatrix} v_{t1}(|p_{s2}|) \\ v_{n1}(|p_{s2}|) \\ 0 \\ v_{n2}(|p_{s2}|) \end{bmatrix} \;+\; \mathbf{A}_S(\mu_1, \bar{\mu}_2) \cdot (|p_{n1}| \;-\; |p_{s2}|) \tag{5.12}$$

where $\mathbf{A}_S(\mu_1, \bar{\mu}_2)$ represents the conditions for stick of point 2. However, it is still necessary to check the no-slip condition in (2.3) to determine whether the impact point remains in stick or slip-reverses throughout the remainder of the impact event. For the case in which v_{t2} sticks and v_{t1} continues forward sliding, then the no-slip condition is derived in Sec. 5.2 as a function of $|p_{n1}|$ by combining (2.3), (5.18), and (5.21), yielding,

$$p_{t2} \;-\; \mu_{s2}\,|p_{n2}| \;=\; \frac{a_{31} sgn(v_{t1})\mu_1 - a_{32} - a_{34}C - a_{33}\mu_{s2}\,C}{a_{33}}\,(|p_{n1}| \;-\; |p_{s2}|) + \frac{v_{t2}}{a_{33}} \;\leq\; 0 \tag{5.13}$$

where a_{ij} are the elements of the matrix formed by $JM^{-1}J^T$ describing the system inertia and configuration, and used to form $\mathbf{A}_S(\mu_1, \bar{\mu}_2)$ in (5.12). It is assumed that $a_{33} \neq 0$ and μ_{s2} is the static coefficient of friction at point 2. Equation (5.13) represents the shaded region shown in Fig. 5.3a. If v_{t2} remains within the shaded region, then the point will stick, otherwise it will slip-reverse. A similar process is used to obtain the no-slip condition for v_{t1}.

For completeness, the scenario involving two points remaining in stick after the stick-slip transition, shown in Fig. 5.3b, results in,

$$\boldsymbol{\vartheta} \;=\; \begin{bmatrix} 0 \\ v_{n1}(|p_{s1,2}|) \\ 0 \\ v_{n2}(|p_{s1,2}|) \end{bmatrix} \;+\; \mathbf{A}_S(\bar{\mu}_1, \bar{\mu}_2) \cdot (|p_{n1}| \;-\; |p_{s1,2}|) \tag{5.14}$$

where $\mathbf{A}_S(\bar{\mu}_1, \bar{\mu}_2)$ represents the conditions for two points in stick. Correspondingly, the no-slip conditions for points 1 and 2 yield,

$$p_{t1} \;-\; \mu_{s1}\,|p_{n1}| \;=\; \frac{-a_{11}\mu_{s1} - a_{12} - (a_{14} + a_{13}\mu_{s2})\;C}{a_{13}}\;(|p_{n1}| \;-\; |p_{s1,2}|) \;+\; \frac{v_{t1}}{a_{13}} \;\leq\; 0 \tag{5.15}$$

$$p_{t2} \;-\; \mu_{s2}\,|p_{n2}| \;=\; \frac{-a_{31}\mu_{s1} - a_{32} - (a_{34} + a_{33}\mu_{s2})\;C}{a_{33}}\;(|p_{n1}| \;-\; |p_{s1,2}|) \;+\; \frac{v_{t2}}{a_{33}} \;\leq\; 0 \tag{5.16}$$

where μ_{s1} and μ_{s2} are the respective static coefficients of friction for points 1 and 2, and it is also assumed that $a_{13},\ a_{33} \neq 0$. Equations (5.15) are represented by the shaded region depicted in Fig. 5.3b. Each impact point is governed by its respective no-slip condition and indicate whether the slip-state of the impact point will change before the impact event ends. It is possible to interrupt an impact point in sticking if another point comes to rest during the impact event—any changes to the slip-state of the impact points will result in slope changes in the evolution of velocities.

5.2 No-Slip Condition

Here, an attempt is made to present the derivation of the no-slip condition from (2.3) as a function of $|p_{n1}|$, without any loss of generality. Consider the case in Fig. 5.2a where only $v_{t2} = 0$. The evolution of velocities in (5.3) before the application of any equations from (5.4) are expressed as,

$$\begin{bmatrix} v_{t1} \\ v_{n1} \\ v_{t2} \\ v_{n2} \end{bmatrix} = \begin{bmatrix} v_{t1}(|p_{s2}|) \\ v_{n1}(|p_{s2}|) \\ 0 \\ v_{n2}(|p_{s2}|) \end{bmatrix} + JM^{-1}J^T \begin{bmatrix} p_{t1} \\ p_{n1} \\ p_{t2} \\ p_{n2} \end{bmatrix} \tag{5.17}$$

Setting $v_{t2} = 0$ yields a scalar constraint of the form,

$$v_{t2} \;=\; 0 \;=\; a_{31}\, p_{t1} \;+\; a_{32}\, p_{n1} \;+\; a_{33}\, p_{t2} \;+\; a_{34}\, p_{n2} \tag{5.18}$$

where a_{ij} are the elements of the matrix formed by $JM^{-1}J^T$ describing the system inertia and configuration. Equation (5.18) is used instead of the second Coulomb relation in (5.4) for v_{t2} but note that the first Coulomb relation in (5.4) is still valid for v_{t1}. These two constraints yield,

$$p_{t2} \;=\; -\frac{a_{31}}{a_{33}}\, p_{t1} \;-\frac{a_{32}}{a_{33}}\, p_{n1} \;-\; \frac{a_{34}}{a_{33}}\, p_{n2} \;=\; \frac{a_{31} sgn(v_{t1})\mu_1 - a_{32}}{a_{33}}\, |p_{n1}| \;-\; \frac{a_{34}}{a_{33}}\, |p_{n2}| \tag{5.19}$$

where $\mu_1 = \mu_d$ and assuming that $a_{33} \neq 0$; it is reasonable to assume that the impulse at p_{t2} would have some relation to the speed at v_{t2}. Using (5.19) gives an equation similar to (5.6) as

$$\boldsymbol{\vartheta} \;=\; \begin{bmatrix} v_{t1}(|p_{s2}|) \\ v_{n1}(|p_{s2}|) \\ 0 \\ v_{n2}(|p_{s2}|) \end{bmatrix} + JM^{-1}J^T \begin{bmatrix} -sgn(v_{t1})\mu_1 & 0 \\ 1 & 0 \\ \dfrac{a_{31} sgn(v_{t1})\mu_1 - a_{32}}{a_{33}} & -\dfrac{a_{34}}{a_{33}} \\ 0 & 1 \end{bmatrix} \begin{bmatrix} 1 \\ C \end{bmatrix} \cdot (|p_{n1}| - |p_{s2}|) \tag{5.20}$$

which describes how the velocities evolve after $|p_{s2}|$. Note that for this case, C is only a function of $\mu_1 = \mu_d$.

However, it is still necessary to check the no-slip condition to determine whether this point might slip-reverse. This is accomplished by using (5.18) without setting $v_{t2} = 0$ which yields a relation similar to (5.19):

$$\begin{aligned} v_{t2} &= -\frac{a_{31}}{a_{33}}\, p_{t1} - \frac{a_{32}}{a_{33}}\, p_{n1} - \frac{a_{34}}{a_{33}}\, p_{n2} + \frac{v_{t2}}{a_{33}} \\ &= \frac{a_{31} sgn(v_{t1})\mu_1 - a_{32} - a_{34}\, C}{a_{33}} \left(|p_{n1}| - |p_{s2}|\right) + \frac{v_{t2}}{a_{33}} \end{aligned} \tag{5.21}$$

such that the no-slip condition for point 2 becomes,

$$p_{t2} - \mu_{s2}\, |p_{n2}| = \frac{a_{31} sgn(v_{t1})\mu_1 - a_{32} - a_{34}\, C - a_{33}\mu_{s2}\, C}{a_{33}} \left(|p_{n1}| - |p_{s2}|\right) + \frac{v_{t2}}{a_{33}} \leq 0 \tag{5.22}$$

where μ_{s2} is the static coefficient of friction for point 2 and this condition applies from the start of stick until the impact event ends, or the slip-state changes. A similar process can be followed to obtain the no-slip condition for v_{t1} and the case for two points in stick.

5.3 Summary

Here, the analytical framework for treating two-dimensional (or planar) indeterminate contact and impact problems with friction was developed. The complex slip behaviors of an impact point due to friction, such as slip-reversal, sticking, and slip-resumption are accounted by this framework. The rigid body constraints were also adapted to work in conjunction with these various slip behaviors throughout an impact event. This framework leads to analytical solutions to the post-impact velocities of a system undergoing indeterminate contact and impact. In addition, a method for checking the no-slip condition, which also incorporates the rigid body constraints

is developed to visualize the regions defined by the no-slip condition for an impact point. The plots generated with these regions provide a verification of the slip-state for a given impact point.

Chapter 6

Simulation Results: Two-Dimensional Examples

In this section, simulation results for the planar ball, rocking block problem and three-ball Newton's Cradle are presented. These examples are studied to demonstrate that the developed analytical framework produces experimentally consistent behaviors. In the following simulations that consider friction, the static μ_s and dynamic μ_d coefficient of friction are 0.6 and 0.35 for all impacting surfaces. The stick-slip transition is a major characteristic behavior of multibody systems with contact and impact. The effects of this transition region will be apparent in the results obtained from the cases analyzed.

6.1 Example 1: Planar Ball

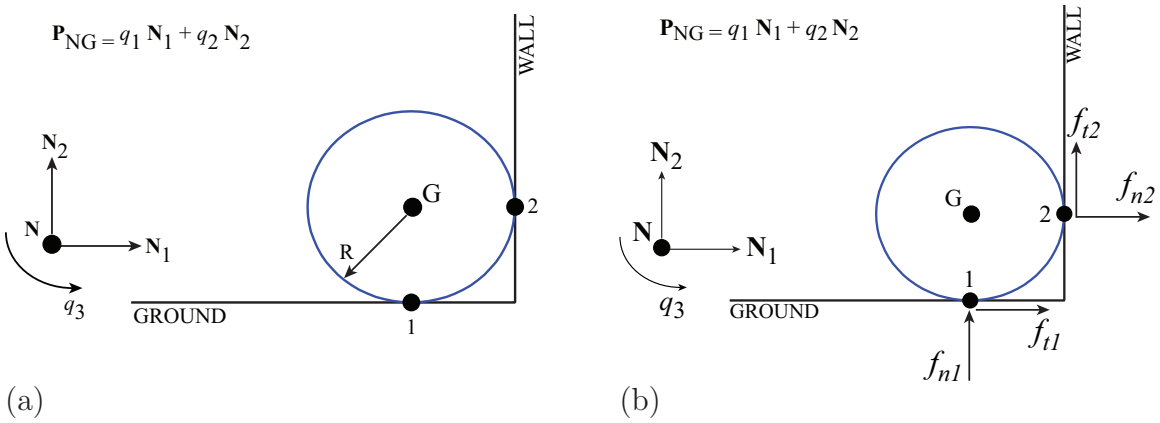

Figure 6.1. (a) Planar model of the ball example (repeated) and (b) velocities and forces at impact points 1 (ground) and 2 (wall) (repeated).

Here, the planar ball example introduced in Ch. 1 impacting a corner, as shown in Fig. 6.1a, is analyzed as a benchmark to show that the proposed method can be applied to other multiple point impact problems. The simulation of the ball is depicted in Fig. 6.2a and ends when a second collision is detected with the ground. A plot of the system energy is shown in Fig. 6.2b to show energy consistency throughout the simulation. Only one impact event is detected in the simulation of the first collision, an indeterminate collision involving points 1 and 2. An $e_* = 0.715$ and $\mu_1 = \mu_2 = 0.35$ is used and the data for this case is given in Table 6.1.

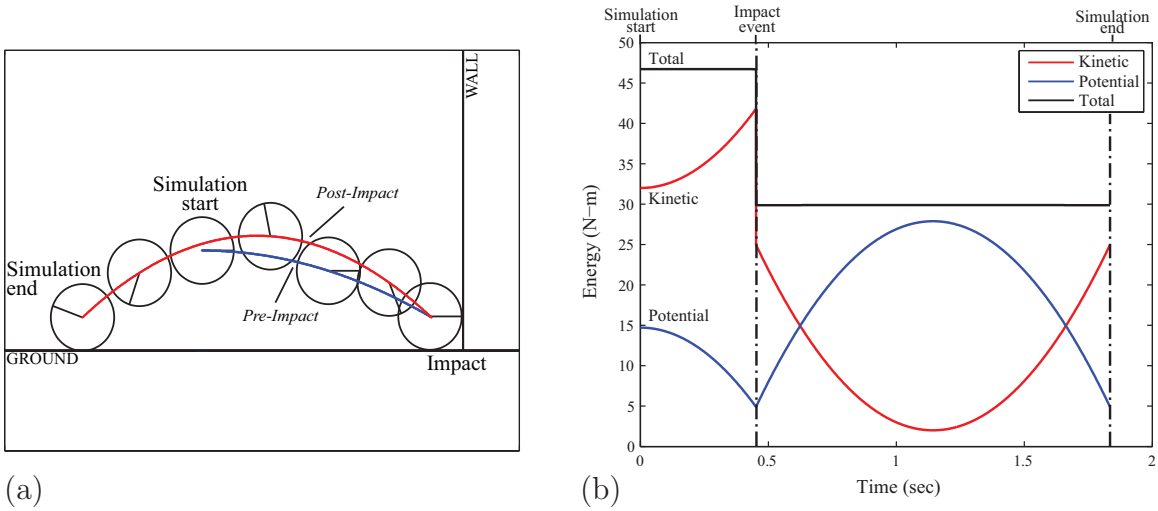

Figure 6.2. (a) Simulation of the planar ball example and (b) energy consistency for the simulation.

The ball has no angular velocity prior to impact but rebounds with a negative angular velocity after impact. This angular velocity is attributed to the slip-state of the wall contact point undergoing slip reversal, while the ground contact point sticks and remains at zero throughout the remainder of the impact event. This is also consistent with the post-impact trajectory of the ball's mass center shown in Fig. 6.2a, which is higher than its pre-impact trajectory.

Table 6.1. Velocities and generalized speeds for the planar ball simulation.

	Initial	**Pre-impact**	**Post-impact**
Position			
q_1	0.000 m	3.614 m	3.614 m
q_2	1.500 m	0.500 m	0.500 m
q_3	0.000 rad	0.000 rad	0.000 rad
Speeds			
$\dot{q}_1$	8.000 m/s	8.000 m/s	-5.504 m/s
$\dot{q}_2$	0.000 m/s	-4.430 m/s	4.893 m/s
$\dot{q}_3$	0.000 rad/s	0.000 rad/s	-9.786 rad/s
Velocities			
v_{t1}	8.000 m/s	8.000 m/s	-10.397 m/s
v_{n1}	0.000 m/s	-4.430 m/s	4.893 m/s
v_{t2}	0.000 m/s	-4.430 m/s	0.000 m/s
v_{n2}	8.000 m/s	8.000 m/s	-5.504 m/s

The result of this case was obtained using the developed analytical framework. First, the impulse at the end of the compression phase was determined by (4.9) and used to find W_{nc} after the last shift in the plot, and the net work done on the system W_{nf} with the *global* ECOR in (4.11). The evolution of the velocities were determined by accounting for the change in slip-state of point 1 and 2 throughout the impact event. The result of these processes is shown in Fig. 6.3. A plot of the normal work throughout the impact event is shown in Fig. 6.3a. There are two shifts in the normal work curve are a result of evaluating the stick-slip transition, which occur at the points where $v_{t2} = 0$ and $v_{t1} = 0$.

The importance of knowing where the tangential velocities come to rest was noted in Sec. 5.0.1 because the stick-slip transition occurs at these instances, which dictate changes in the normal work and evolution of velocities throughout an impact event. The effects of a change in friction direction are illustrated in the evolution of velocities, seen in Fig. 6.3b. Both tangential velocities reach the stick-slip transition

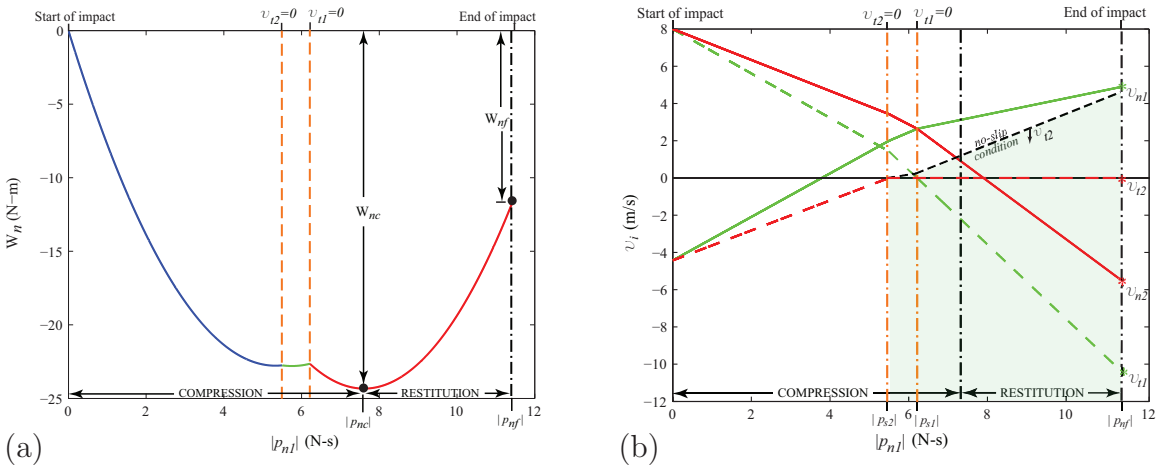

Figure 6.3. (a) Normal work done and (b) evolution of velocities throughout the impact event for the planar ball example.

during this single impact event. The tangential velocity at the wall comes to rest first at $|p_{s2}|$ and is determined to remain in stick. The no-slip condition for this impact point is derived and plotted in Fig. 6.3b to check if the slip-state will change throughout the remainder of the impact event. The tangential velocity of the ground impact point comes to rest next in the impact event at $|p_{s1}|$. This impact point is determined to slip-reverse, such that the friction direction changes which is consistent with the negative angular velocity of the ball after the simultaneous collision. The plot in Fig. 6.3b illustrates a significant shift in the direction of the velocities before they reach their terminal value. The normal work curve in Fig. 6.3a also shows a similar shift before it ascends to its terminal impulse.

The end condition for the normal impulse $|p_{nf}|$ is evaluated with the knowledge of W_{nf}, which marks the end of the impact event. The post-impact velocities at the impact end serve as the initial conditions for restarting the simulation to model the system after impact.

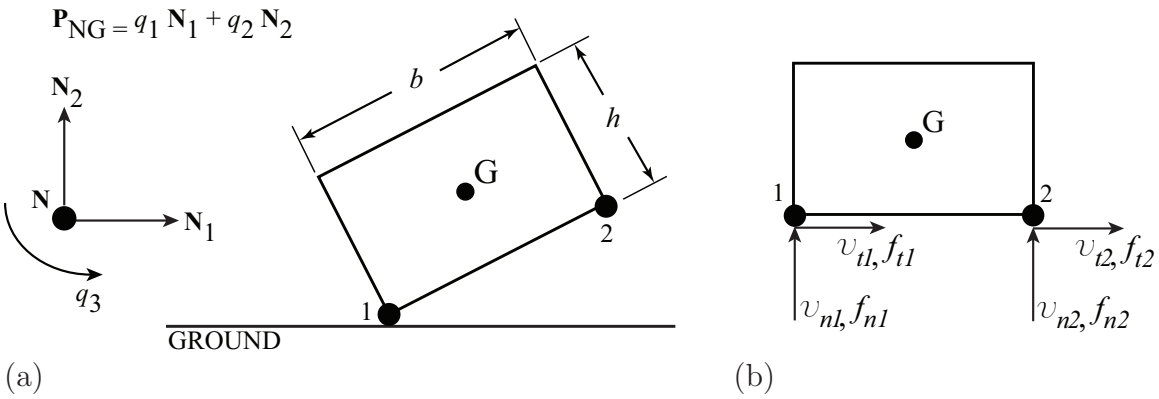

Figure 6.4. (a) Planar model of a planar rocking block example and (b) velocities and forces at the impact points.

The rocking block example has interested many researchers because of the difficulties which arise in the model [74, 1, 75, 76]. The two main issues encountered are the switch between rocking constraints at the bottom corners of the block and the indeterminate system equations encountered when points 1 and 2 are simultaneously in contact with the ground.

The planar rocking block model, as shown in Fig. 6.4a has three DOFs and its center of mass at point G. The block's position is indicated by translational generalized coordinates q_1 and q_2, and its orientation by q_3. The block has width b and height h, where $b/h > \sqrt{2}$ (flat block [1, 76]) in the two cases studied here. It is further assumed in this simulation that the contact of the block's bottom surface with the ground occurs at only two points, labeled as 1 and 2 in Fig. 6.4.

The switch in rocking constraints between the corners of the block at points 1 and 2 is addressed using a discrete approach. Contact constraints are enforced when either point 1 or 2 is in contact with the ground during a rocking motion. This

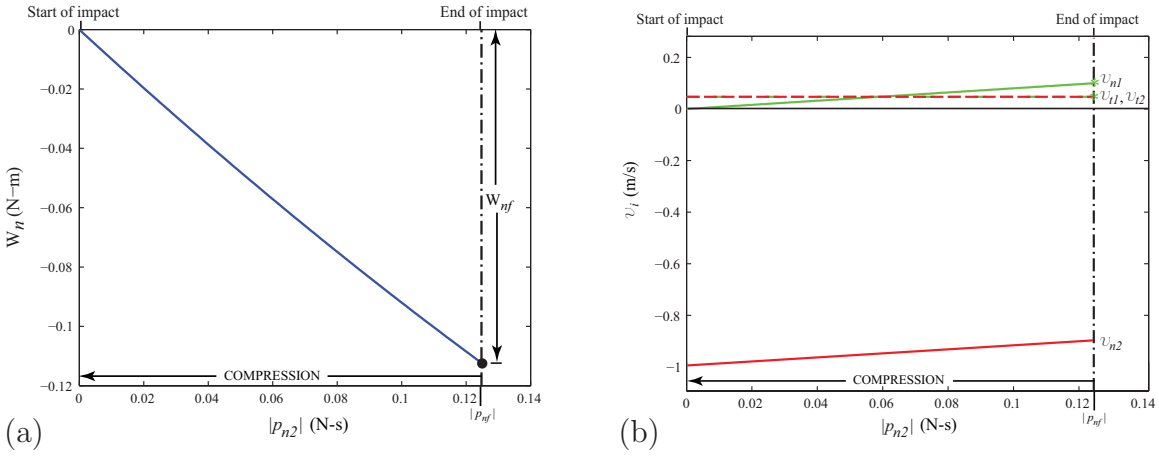

Figure 6.5. (a) Normal work done and (b) evolution of velocities throughout the first impact event for the frictionless rocking block example.

means that the point in contact is not permitted to penetrate the ground using normal kinematic constraints but can slide or stick tangent to the ground. Additionally, there is a short instance when both points 1 and 2 are simultaneously in contact with the ground. This introduces an indeterminacy in the equations of motion with respect to the impact forces, as introduced in Ch. 1. A constraint among the contact points is implemented to resolve the indeterminacy using the proposed method.

6.2.1 Case 1: Frictionless Rocking Block

The benchmark case considered is a frictionless rocking block example with model conditions identical to the experimental study in [1]. The block has a mass $m = 2.5\ kg$, width $b = 0.1087\ m$ and height $h = 0.0645\ m$. Note here that for the frictionless case ($\mu_1 = \mu_2 = 0$), the tangential forces, f_{t1} and f_{t2}, shown in Fig. 6.4b vanish. The simulation starts with point 1 in contact while the block rocks and point 2 impacts the ground; $\theta_1 = \theta_2 = 0^\circ$ in [1] is used which corresponds to a flat plane, or ground surface as it is modeled here.

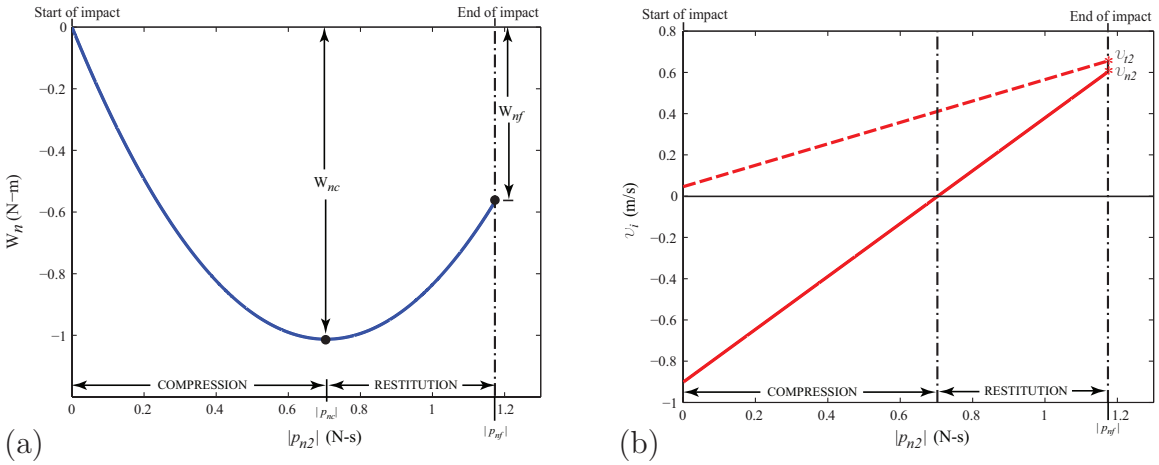

Figure 6.6. (a) Normal work done and (b) evolution of velocities throughout the second impact event for the frictionless rocking block example.

The result of the simulation is depicted in Fig. 6.7a and obtained using the proposed method. A plot of the system energy is included in Fig. 6.7b to show energy consistency for the simulation performed. The collision of point 2 with the ground results in the simultaneous contact of points 1 and 2. This triggers two impact events which are representative of the entire collision of the block with the ground. At the end of the first impact event, the post-impact velocity of point 2 is negative which indicates that it is still moving toward the ground surface. This situation is interpreted as a second impact event involving only point 2. In addition, after the first impact event, point 1 has a positive velocity which is interpreted as having reached its post-impact state. Thus, before restarting the simulation, the second impact event is resolved to find the post-impact velocities of point 2.

The analysis of the first impact event is illustrated in Fig. 6.5. Particularly Fig. 6.5a shows the normal work plot where $e_* = -0.803$ is used, which is still in its compression phase when the first impact event is ended by the start of the second impact event. Note again $e_* < 0$ means that in a simultaneous, multiple point

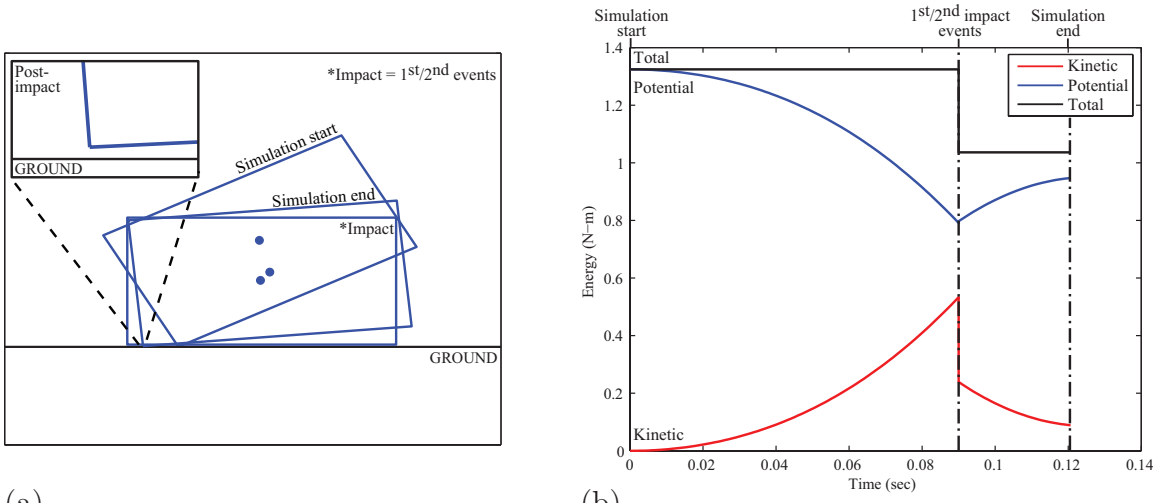

(a) (b)

Figure 6.7. (a) Simulation of the frictionless rocking block example and (b) energy consistency for the simulation.

Table 6.2. Comparison of theoretical and experimental results for a frictionless rocking block with $m = 2.5\ kg$, $b = 0.1087\ m$, $h = 0.0645\ m$ and $\theta_1 = \theta_2 = 0°$ in [1].

		v_1^+/v_2^-	v_2^+/v_2^-	ECORs[1]
Experimental	Yilmaz, et al. [1]	-0.100	-0.600	$e_1 = 0.43$, $e_2 = 0.64$
Theoretical	Rodriguez-Bowling	-0.100	-0.600	$e_* =$ -0.803, 0.654

collision, subsequent impact events may begin while the initial impact event has not completed its characteristic compression phase, as illustrated in Fig. 4.3. Figure 6.5b depicts the evolution of velocities throughout the first impact event. This figure shows how the normal, v_{n1}, and tangential, v_{t1}, velocity of point 1 reach their final, or terminal value at the end of the first impact event. Meanwhile, the normal velocity of point 2 is negative which indicates that it is still impacting the ground and initiates a second impact event.

[1]The ECORs (e_1, e_2) used in [1] are local for each impact point; in this work, two impact events are detected for this case so two *global* ECORs are used here in the order specified.

Analysis of the second impact event is shown in Fig. 6.6 and only involves the velocities of point 2, v_{n2} and v_{t2}. It begins with the velocity of point 2 at the end of the first impact event. In the second impact event, $e_* = 0.654$ is used which yields the evolution of velocities of point 2 shown in Fig. 6.6b.

The results of this benchmark case are comparable to the motion obtained from the experimental result reported in Figure 8 of [1]; Table 6.2 shows this comparison. The proposed work uses *global* ECORs to define the energy dissipated in an impact event. These were selected, such that $e_* = -0.803, 0.654$ were used for the first and second impact events, respectively. The work in [1] uses local ECORs for each of the impact points and experimentally determined them to be $e_1 = 0.43$, $e_2 = 0.64$ for points 1 and 2, respectively. As a result, the solution to the post-impact velocities obtained from this work identically matches the experimental result obtained in [1], shown in Table 6.2. Figure 6.7a shows a close up view of the post-impact state of the block leaving the ground surface after the simultaneous collision. The post-impact velocities in Table 6.2 for points 1, v_1^+, and 2, v_2^+, are normalized with respect to the pre-impact velocity of point 2, v_2^-, to directly compare the two results. In this way, the use of *global* ECORs in the proposed approach is able to produce accurate results that can match experimental data for a frictionless model.

6.2.2 Case 2: Frictional Rocking Block

A rocking block with friction is explored here to observe the effects of considering friction at the impact points. The same model parameters and initial conditions, as in Sec. 6.2.1, are used in this simulation aside from friction at the impact points, where initially $\mu_1 = \mu_2 = 0.35$. The coefficients of friction do not have to be the same but it makes sense for this example because the points impact the same surface.

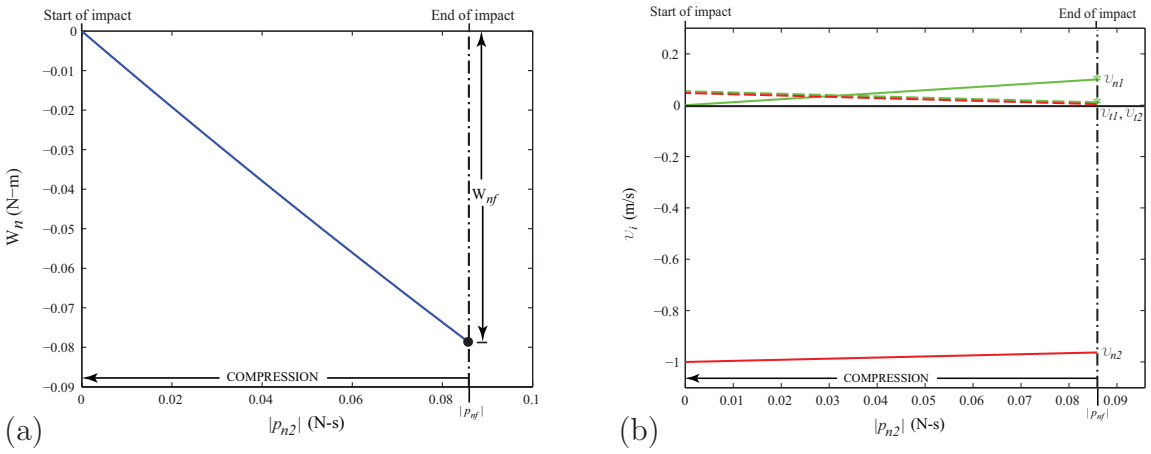

Figure 6.8. (a) Normal work done and (b) evolution of velocities throughout the first impact event for the frictional rocking block example.

Table 6.3. Comparison of a frictional rocking block to theoretical and experimental results of a frictionless case.

		v_1^+/v_2^-	v_2^+/v_2^-	ECORs[2]
Experimental	Yilmaz, et al. [1]	-0.100	-0.600	$e_1 = 0.43$, $e_2 = 0.64$
Theoretical	Rodriguez-Bowling			
	no friction	-0.100	-0.600	$e_* =$ -0.803, 0.654
	with friction	-0.100	-0.600	$e_* =$ -0.883, 0.662

The results of the simulation are depicted in Fig. 6.10a and a plot of the system energy is included in Fig. 6.10b to show energy consistency for the simulation performed. Similar to the frictionless case, the collision of point 2 with the ground results in two impact events which are representative of the entire collision of the block with the ground. The first impact event is the only indeterminate one in the simulation, which involves the simultaneous impact of points 1 and 2. The post-impact velocity of point 2 at the end of the first impact event is negative which indicates that it is still

[2]The ECORs (e_1, e_2) used in [1] are local for each impact point; in this work, two impact events are detected for this case so two *global* ECORs are used here in the order specified.

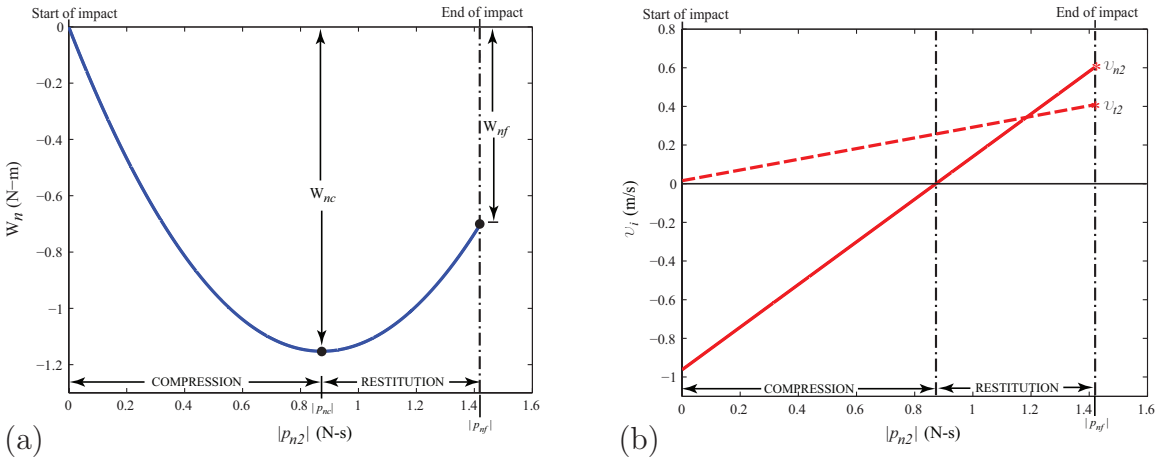

Figure 6.9. (a) Normal work done and (b) evolution of velocities throughout the second impact event for the frictional rocking block example.

moving toward the ground surface. This situation is interpreted as a second impact event involving only point 2, a determinate collision. Furthermore, point 1 has a positive velocity after the first impact event, which is interpreted as having reached its post-impact state, as in the frictionless case. This second impact event is resolved before restarting the simulation.

The result obtained for this case is identical to the frictionless case analyzed in Sec. 6.2.1 and [1]. The only difference is the *global* ECORs are $e_* = -0.883, 0.662$ for the first and second impact events, respectively. The first impact event, illustrated in Fig. 6.8, shows a plot of the normal work and evolution of velocities. The inclusion of friction for this case does not cause the tangential velocities to come to rest at the stick-slip transition; this is almost the case at the end of the first impact event. Thus, the slope of the velocities never changes and the impact points maintain a slip-state of forward sliding throughout the impact event. The plot of the normal work in Fig. 6.8a shows that the first impact event terminated in its compression phase due to the start of the second impact event. As in the frictionless case, Fig. 6.8b shows how

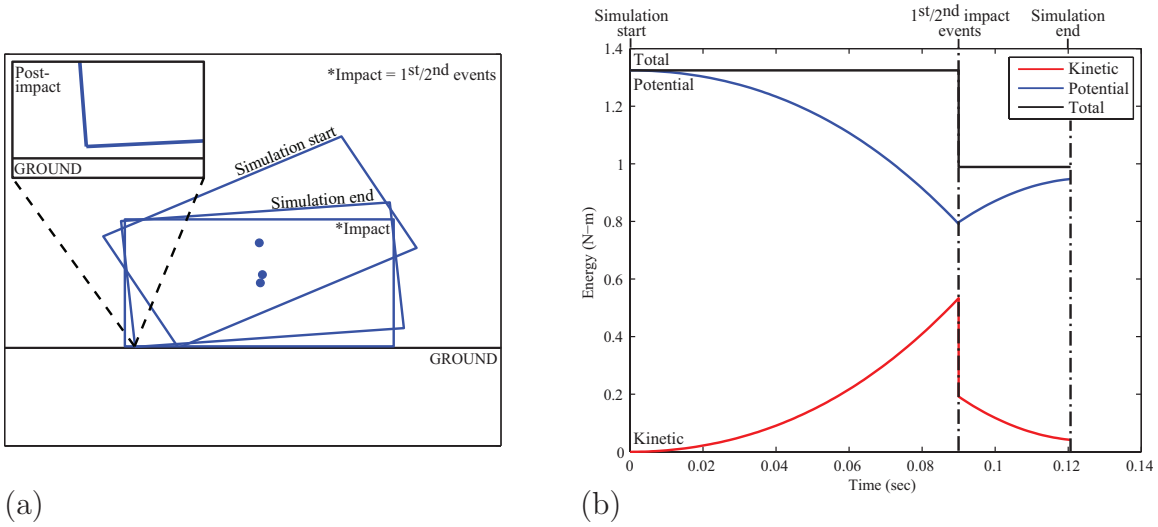

(a) (b)

Figure 6.10. Simulation of the frictional rocking block example and (b) energy consistency for the simulation.

the normal, v_{n1}, and tangential, v_{t1}, velocity of point 1 reach their terminal value at the end of the first impact event. Meanwhile, the normal velocity of point 2 is negative which indicates that it is still impacting the ground and initiates a second impact event. The analysis of the second impact event is shown in Fig. 6.9 and only involves point 2. Figure 6.9a shows the characteristic parabolic shape of the normal work where a compression and restitution phase are clearly defined. Figure 6.9b shows how the velocities of point 2, v_{n2} and v_{t2} reach their terminal value.

The results from this case are summarized in Table 6.3, and also includes the results presented in Table 6.2 for the frictionless case examined in Sec. 6.2.1. Figure 6.10a also shows a close up view of the post-impact state of the block leaving the ground surface after the simultaneous collision. The post-impact velocities of points 1, v_1^+, and 2 v_2^+, are normalized with respect to the pre-impact velocity of point 2, v_2^-. The solution to the post-impact velocities of points 1 and 2 are also identical to the result obtained for the frictionless case. The only difference when friction

is considered is the effect on the *global* ECORs applied in the proposed framework. Friction is dissipative by nature and it is observed that this leads to an increase in the ECORs used to obtain the same post-impact result. Notice that slightly greater *global* ECORs are used in the first and second impact events for the frictional case than in the frictionless case. This example further demonstrates how this work is applied to match experimental work, while accounting for any friction in the model. Although not observed in the analysis of the rocking block cases, the following analysis of the planar ball example will show how the stick-slip transition is treated and affects the solution to the post-impact state.

6.3 Example 3: Three-Ball Newton's Cradle

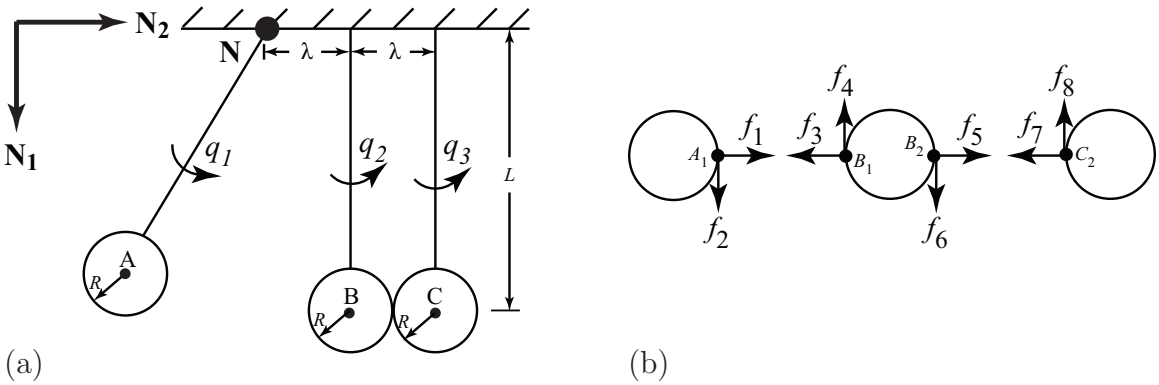

Figure 6.11. (a) Planar model of a three-ball Newton's Cradle and (b) forces at the impact points for each ball.

Consider the Newton's cradle in Fig. 6.11a with three balls of equal radius R labeled A, B, and C with mass m_A, m_B, and m_C. The balls hang from massless strings of length L which are separated by a distance λ. Note that there are eight unknown impact forces, f_1 through f_8 in Fig. 6.11b, but only three rotational generalized

coordinates, q_1, q_2, and q_3. The consideration of frictional impact introduces the tangential forces, f_2, f_4, f_6, and f_8 which are not considered in other works that assume frictionless impacts [77, 78, 79, 2].

6.3.1 Case 1: Uniform, Unit Mass and $e_* = 1$

The first case considered for the three-ball system in Fig. 6.11a examines balls with equal, unit mass $m_A = m_B = m_C = 1\ kg$ and $e_* = 1$, which specifies no energy loss. The motion obtained from simulating this case is shown in Fig. 6.12a. This figure only shows the results of the first collision, which triggers a single impact event. This impact event is indeterminate with respect to the impact forces.

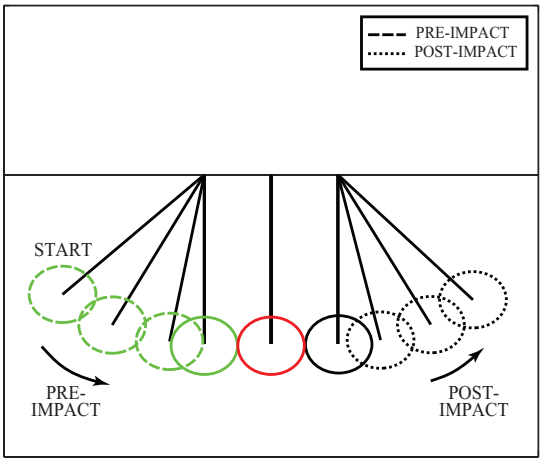

(a)

		Pre-impact	Post-impact
Velocities		(m/s)	(m/s)
Ball A	v_1	1.304	0.000
	v_2	-0.217	0.000
Ball B	v_3	0.000	0.000
	v_4	0.000	0.000
	v_5	0.000	0.000
	v_6	0.000	0.000
Ball C	v_7	0.000	1.304
	v_8	0.000	0.217
Generalized speeds		(rad/s)	(rad/s)
Ball A	$\dot{q}_1$	4.347	0.000
Ball B	$\dot{q}_2$	0.000	0.000
Ball C	$\dot{q}_3$	0.000	4.347

(b)

Figure 6.12. (a) Simulation of the three-ball Newton's Cradle with $e_* = 1$ and (b) table of velocities and generalized speeds.

Ball A is released from rest, swings down, and impacts Balls B and C which are at rest and in contact. Ball A has pre-impact velocity $v_1^- = 1.304\ m/s$. The momentum of Ball A is completely transferred to Ball C, while Balls A and B are at rest and in contact after the collision; the data for this case is given in Fig. 6.12b. A similar result is obtained when Ball C swings back to impact Balls A and B.

First, the impulse at the end of the compression phase was determined using (4.9); for this case $|p_{nc}| = 0.659$ N-s as shown in Fig. 6.13. Using this, one can find W_{nc} and the net work done W_{nf} using the ECOR in (4.11). Lastly, the final impulse at the end of the impact event results in $|p_{nf}| = 1.318$ N-s, which is used to find the post-impact velocities with (5.6). The results of this process are shown in Fig. 6.13.

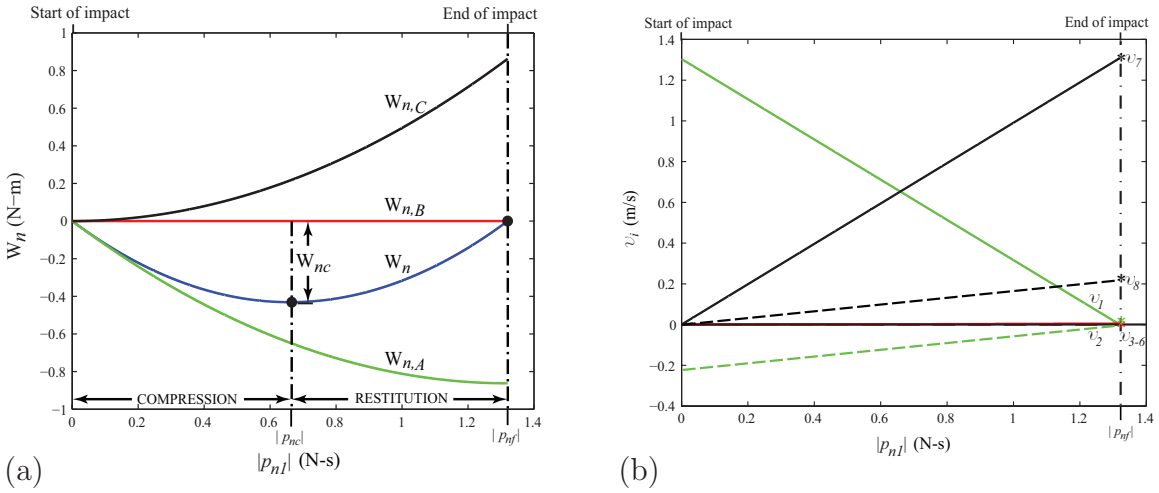

Figure 6.13. (a) Normal work done and (b) evolution of velocities throughout the impact event for the three-ball Newton's Cradle with $e_* = 1$.

A plot of the normal work at the *system level* is shown in Fig. 6.13a by the line labeled W_n. The other three lines show the work done on the individual balls, $W_{n,A}$, $W_{n,B}$, and $W_{n,C}$, which are summed to obtain W_n as in (4.7). Since $e_* = 1$ no energy

is dissipated, which is shown in Fig. 6.13a by W_n ascending back to zero at the end of the restitution phase. Notice that the individual plots of $W_{n,A}$, $W_{n,B}$, and $W_{n,C}$ do not show clear compression and restitution phases, making it difficult to apply the ECOR to each ball. Thus, the plot shows that the ECOR in this work can only function as a global parameter to model the energy dissipated at the *system level*. It will not consider differences in material properties between the balls; i.e. one ball is less elastic, or softer, than another. This is the result of negligible local compliance at the impact points.

The evolution of the velocities during the first impact, shown in Fig. 6.13b, are determined. These calculations show the complete transfer of momentum from Ball A to Ball C. The compressive work done initiates the transfer of momentum as the normal velocity of Ball A, v_1 decreases and Ball C, v_7 increases, as seen in Fig. 6.13b. The point at which these two velocities are equal marks the compression phase end. The velocities of Ball B, v_{3-6} remain constant and zero. The tangential velocity of Ball A, v_2 goes to zero, while that of Ball C, v_8 goes to the initial value of v_2.

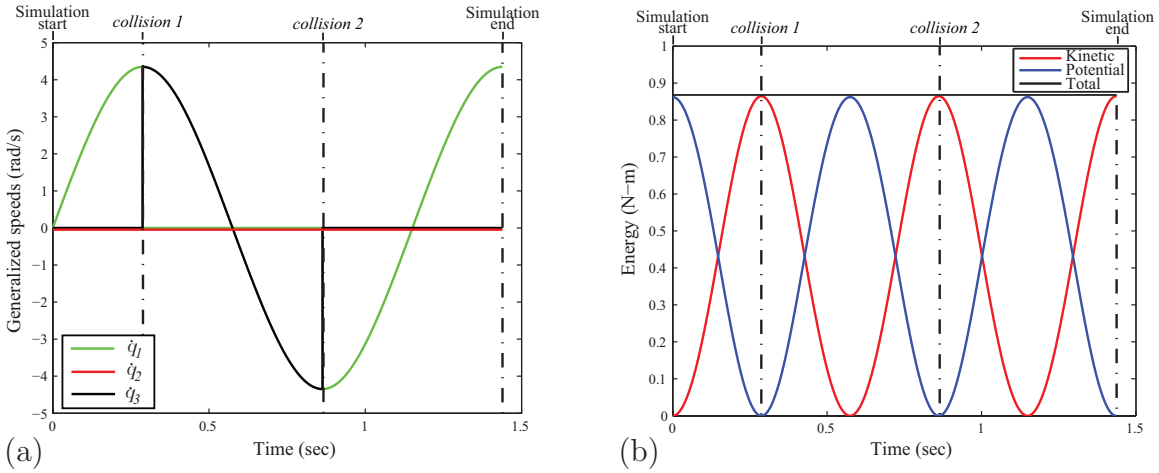

Figure 6.14. (a) Generalized speeds for the three-ball Newton's Cradle and (b) energy consistency throughout the simulation with $e_* = 1$.

The predicted motion shown here is consistent with the results in [80, 77] for a three-ball system with uniform, unit mass and $e_* = 1$. The expected motion for this case, which is noted in [80, 77] is that Balls A and B are very close to zero $\dot{q}_1^+ = \dot{q}_2^+ = 0$, while Ball C moves to the right with the pre-impact velocity of Ball A $\dot{q}_3^+ = \dot{q}_1^-$. Subsequent collisions are not shown in Fig. 6.12a. A plot of the generalized speeds throughout the simulation are shown in Fig. 6.14, for completeness, as well as the energy of the system to verify energetic consistency.

6.3.2 Case 2: Uniform Mass and $e_* = 0.85$

The next case considered for the three-ball Newton's cradle examines balls with $m_A = m_B = m_C = 0.166\ kg$, $e_* = 0.85$, and $v_1^- = 1.0\ m/s$. These are the same conditions for one of the cases studied in [79, 2]. Figure 6.15a depicts the motion obtained from simulating this case and only shows the results of the first collision after Ball A is released from rest. Here, there is a dissipation of energy in the result since $e_* = 0.85$. The data for this case is presented in Fig. 6.15b.

The collision of Ball A with Balls B and C triggers two impact events, a phenomena that was not observed in *Case 1.* The first impact event is the only indeterminate one in the simulation. It involves all three balls simultaneously and most of the momentum is transferred to Ball C. However, the post-impact velocities predicted by the proposed analysis indicate that Ball A is moving to the right at a faster rate than Ball B. This situation is interpreted as a second impact event involving Balls A and B, a determinate collision. In addition, Ball B is moving to the right at a slower rate than Ball C, which is interpreted as Ball C separating from the other two. Thus, before restarting the simulation, this second impact event is resolved also using $e_* = 0.85$ to find the post-impact velocities of Balls A and B. The analysis of the second impact event reveals that neither Ball A or B is at rest after the first two impact events, see

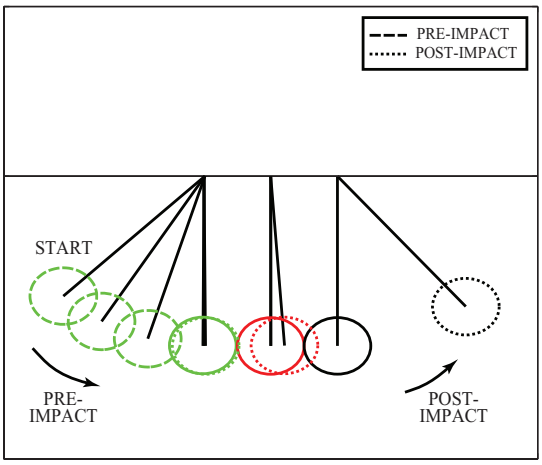

(a)

		Pre-impact	Post-impact
Velocities		(m/s)	(m/s)
Ball A	v_1	1.000	0.006
	v_2	-0.167	-0.001
Ball B	v_3	0.000	0.069
	v_4	0.000	0.012
	v_5	0.000	0.069
	v_6	0.000	-0.012
Ball C	v_7	0.000	0.925
	v_8	0.000	0.154
Generalized speeds		(rad/s)	(rad/s)
Ball A	$\dot{q}_1$	3.333	0.019
Ball B	$\dot{q}_2$	0.000	0.232
Ball C	$\dot{q}_3$	0.000	3.083

(b)

Figure 6.15. (a) Simulation of the three-ball Newton's Cradle with $e_* = 0.85$ and (b) table of velocities and generalized speeds..

Fig. 6.15a. Balls A and B retain some momentum, but most of it is transferred to Ball C.

The analysis of the first impact event is illustrated in Fig. 6.16. Particularly Fig. 6.16a shows the energy loss represented by $e_* = 0.85$ because the curve does not ascend back to zero as occurred in Fig. 6.13a of *Case 1.* This yields a lower terminal impulse, $|p_{nf}|$ for this case, which results in non-zero post-impact velocities for Balls A and B, even though the speed of Ball B is very small, as shown in Fig. 6.16b. This plot depicts the evolution of velocities throughout the first impact event. In Fig. 6.16b, v_7 and v_8 correspond to the terminal normal and tangential velocities of Ball C, respectively. Ball A has residual momentum after the first impact, in which $v_1 > v_{3,5}$, meaning that Ball A is still impacting Ball B. Hence, a second impact event is triggered.

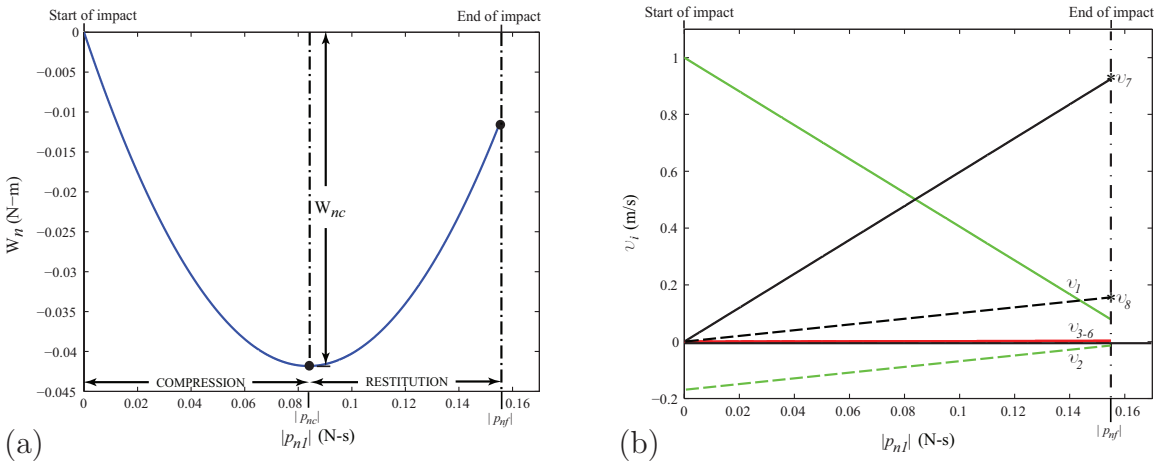

Figure 6.16. (a) Normal work done and (b) evolution of velocities throughout the first impact event for the three-ball Newton's Cradle with $e_* = 0.85$.

Analysis of the second impact event is shown in Fig. 6.17. It begins with the post-impact velocities of Balls A and B obtained from the analysis of the first impact event, in which Ball C has begun to separate from the other two. Thus, the analysis of the normal work in Fig. 6.17a only includes Balls A and B. Once again $e_* = 0.85$ is used, but it is possible to use another value for e_* in this subsequent collision. Some energy is lost in the second impact event which yields the evolution of the velocities of Balls A and B shown in Fig. 6.17b, represented by v_{1-2} and v_{3-6}, respectively.

The propagation of momentum observed in the solution to the post-impact velocities here is comparable to the motion obtained from experimental and theoretical results reported in [2, 79] for a three-ball chain. Specifically, it is comparable to the theoretical results in [79] which reproduces the experimental data in [2] for a ball type of DDD (Table 2, [2]), where D corresponds to a ball with mass $m = 0.166\ kg$ and $e = 0.85$ (Table 1, [2]) with $v_1^- = 1.0\ m/s$. Table 6.4 shows a comparison of theoretical and experimental results from each work. It should be noted that there is a difference in the model description in this work, where $\dot{q}_i$'s are angular general-

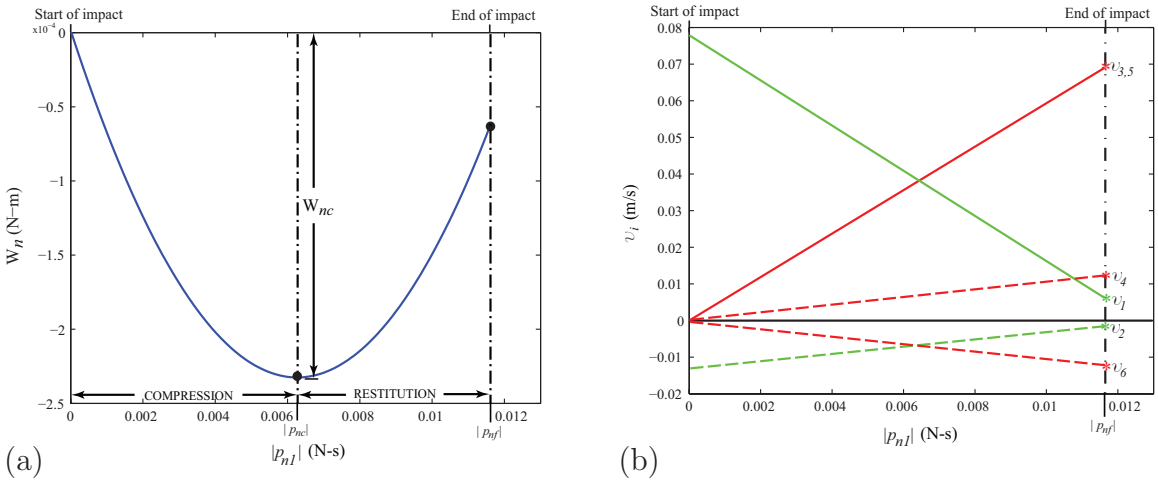

Figure 6.17. (a) Normal work done and (b) evolution of velocities throughout the second impact event for the three-ball Newton's Cradle with $e_* = 0.85$.

ized speeds unlike the translational generalized speeds in [79, 2]. Thus, the motions included in Table 6.4 are the Cartesian velocities of the mass center of each ball; see table footnote [3].

Table 6.4. Comparison of theoretical and experimental results of the three-ball Newton's Cradle with $m = 0.166\ kg$ and $e = 0.85$ (Table 2, [2]).

		$\dot{q}_1^+$ (m/s)	$\dot{q}_2^+$ (m/s)	$\dot{q}_3^+$ (m/s)	$\Sigma\ m_i(\dot{q}_i^+)^2$ $(N-m)$	ECORs[3] [-]
Experimental	[2]	0.036	0.106	0.857	0.124	$e_1 = e_2 = 0.85$
Theoretical	[79]	0.031	0.109	0.860	0.125	$e_1 = e_2 = 0.85$
		0.006	0.069	0.925	0.143	$e_* = 0.85, 0.85$
		0.021	0.124	0.855	0.124	$e_* = 0.711, 0.711$
		0.036	0.106	0.857	0.124	$e_* = 0.715, 0.488$

[3]The ECORs (e_1, e_2) used in [2, 79] are local for each impact point; in this work, two impact events are detected for this case so two global ECORs are used here in the order specified.

The result obtained from this work, which uses a global ECOR $e_* = 0.85$ for the two impact events do not exactly match the results presented in the works of [2, 79], where local ECORs $e_1 = e_2 = 0.85$ are used for each impact point. The post-impact velocities obtained for $\dot{q}_1^+$ and $\dot{q}_2^+$ are much slower than the other works, whereas the solution for $\dot{q}_3^+$ is relatively close. Still, some quality of the solution from this work is concluded since the resulting motions are consistent with $\dot{q}_1^+ < \dot{q}_2^+ < \dot{q}_3^+$. A comparison of $\Sigma\ m_i(\dot{q}_i^+)^2$ is also used to quantify the consistency of the motions. This parameter shows that using $e_* = 0.85$ for the two impact events results in an error of 14-15% compared to the other cases listed in Table 6.4.

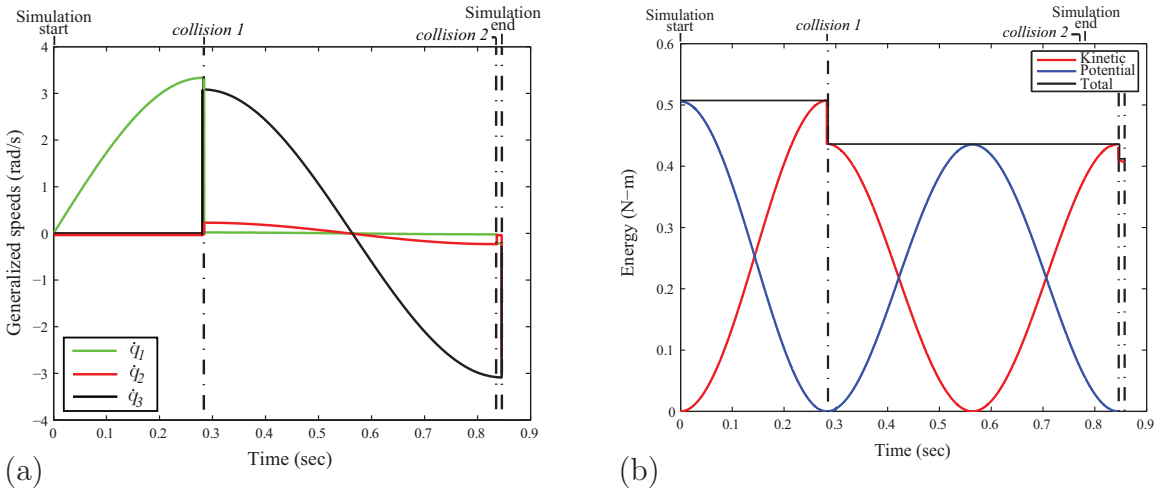

Figure 6.18. (a) Generalized speeds for the three-ball Newton's Cradle and (b) energy consistency throughout the simulation with $e_* = 0.85$.

The consistency of the motion obtained in this work in comparison to [2, 79] could be improved if different global ECORs are used. Therefore, the two global ECORs were lowered to $e_* = 0.711$ to match $\Sigma\ m_i(\dot{q}_i^+)^2$, which also improved the solution of the post-impact velocities of each ball. Specifically, the result for $\dot{q}_1^+$ and $\dot{q}_3^+$ is much improved. Since it is possible to use a different value for e_* in

the subsequent impact event, the global ECORs were modified to be $e_* = 0.715$ and $e_* = 0.488$ for the first and second impact events, respectively. This produced a solution to the post-impact velocities that identically matches the experimental result obtained in [2]. In this way, the use of global ECORs in the proposed approach is able to produce accurate results to model elasticity without using any springs. A plot of the generalized speeds and system energy throughout the simulation is depicted in Fig. 6.18.

Table 6.5. Model and simulation parameters for the three-ball Newton's Cradle cases.

	Parameter[4]	**Value**	**Unit**
Model	L	0.30	m
	R	0.05	m
	λ	0.10	m
Three ball			
Case 1	$m_A - m_C$	1.00	kg
	v_1^-	1.304	m/s
	μ_1, μ_2	0.0	-
Case 2	$m_A - m_C$	0.166	kg
	v_1^-	1.00	m/s
	μ_1, μ_2	0.0	-

[4] *L is the length that each ball hangs (measured to mass center), R is the radius of each ball, and λ is the horizontal distance between each ball's mass center. In this work, λ=2R (no separation) and all balls at rest are in contact. The terms m_i are the mass of each ball i, v_1^- is the initial velocity of Ball A when it collides the chain of balls initially at rest, and μ_i are the coefficient of friction between ball i and $i+1$.*

6.4 Summary

The treatment of three planar example problems were analyzed using the developed analytical framework from Chapter 6. The planar ball analysis was a benchmark example first considered to develop the novel rigid body constraint technique. The changes in slip-state for each impact point was apparent from the analysis of this example – impact point 2 remained in stick while point 1 slip-reversed. The regions for the no-slip condition verified these results. The analysis of the frictionless and frictional rocking block examples provided a way to define a range of values for the ECOR and capture of multiple impact events for a single collision. The results of these cases were compared and identically matched to experimental data found in the literature. The three-ball Newton's Cradle was the final planar example analyzed. It was observed that the ECOR in the present framework was interpreted to function as a *global* energy dissipation parameter. The results of a uniform series of balls were also validated using experimental data.

Chapter 7

Three-Dimensional Impact: Numerical Framework

This section is focused on treating three-dimensional (3D) multibody systems experiencing indeterminate contact and impact with friction. The framework for two-dimensional impact problems was developed to obtain analytical solutions. The transition of this analytical framework to treat three-dimensional impact problems is not so easy. Complications arise when friction is modeled due to the non-linearities associated with sliding friction on the slip plane of the impact point. This further leads to five, first-order nonlinear ordinary, differential equations in the case of single point impact [3, 4, 5, 6, 7, 8]. For a limited set of impact configurations (i.e. collinear/central impact), an analytical solution is possible.

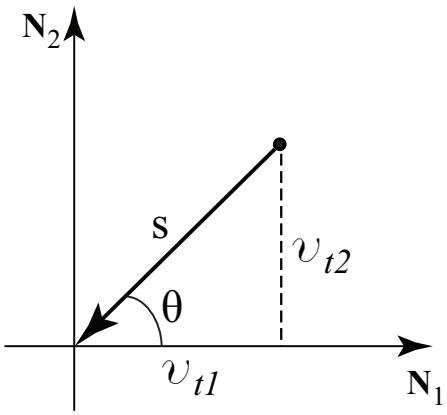

(a)

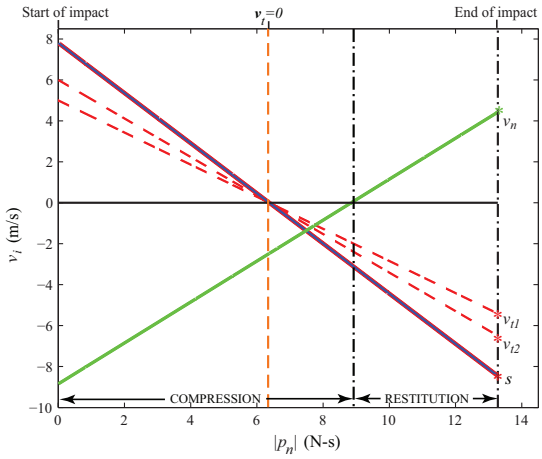

(b)

Figure 7.1. (a) Slip plane of an impact point coming to rest and (b) evolution of normal and sliding velocities throughout an impact event.

Consider for example the 3D impact of a sphere with a half-space (or ground plane). The problem that arises in 3D impact problems with friction is determining the slip direction θ of the impact after it comes to rest, shown in Fig. 7.1a. Note that the slip direction is formed by the velocity components v_{t1} and v_{t2} on the slip plane of the sliding point with sliding velocity s. Stronge showed that for collinear or central collision of bodies that are axisymmetric about the common normal direction, the direction of slip θ does not vary [3]. The sliding velocity also remains constant and found as: $s = -\mu(1 + 5/2)|p_n|$ which produces the plot shown in Fig. 7.1b.

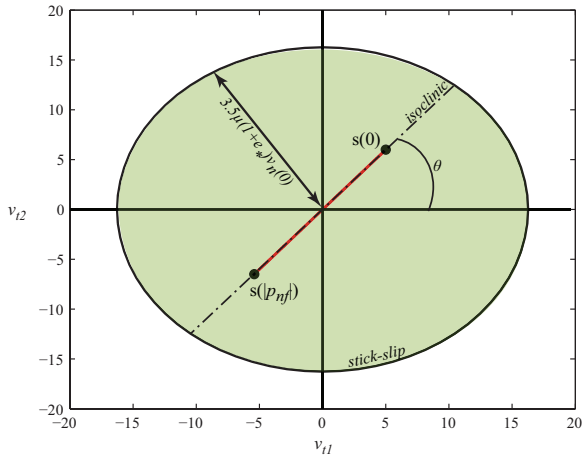

Figure 7.2. Hodograph of an impact point throughout an impact event.

Figure 7.2 shows a hodograph of the impact analysis for this example. Hodographs are a plot of the slip trajectory for an impact point on the slip plane. This plot provides a way to visualize the regions for different slip processes as a result of the stick-slip transition. Battle showed that for a point that comes to rest and slip-reverses, (i) the slip direction is constant (also known as an isoclinic), (ii) impact configuration and coefficient of friction dependent, and (iii) it is unique (relative acceleration of the impact point is positive) [81].

So, what does this mean? Impact problems similar to the sphere example (i.e. collinear impact) can be solved analytically but this is not the general case. The slip direction is not always constant and is nonlinear. In addition, the coupled, nonlinear differential equations which are encountered in 3D problems cannot be solved analytically. Several attempts were made in this research to circumvent the issue, such as, changing the generalized coordinates of the model. This task lead to no new developments. The alternative was to develop a numerical framework, while preserving the remaining key elements of the analytical framework developed for two-dimensional impact problems. These included addressing the indeterminacy using rigid body constraints, equations of motion in the impulse domain using Coulomb friction, analysis of the stick-slip transition and energy dissipation using Stronge's energetic coefficient of restitution (ECOR).

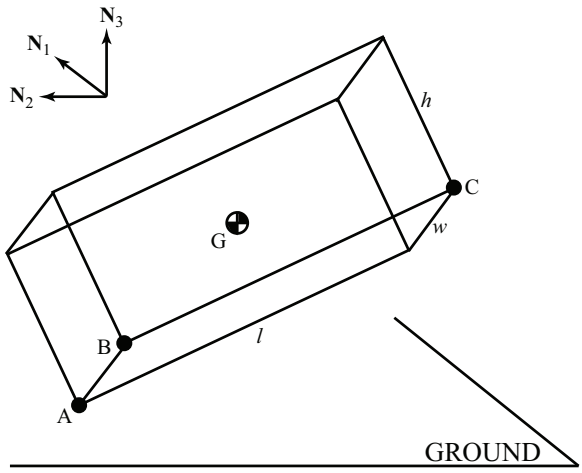

Figure 7.3. Three-dimensional model of a rocking block example with three corner impact points.

Consider, by way of example, the three-dimensional model of a rocking block with three impact points (A, B, and C), shown in Fig. 7.3. This example is considered

as an equivalent foot-ground interaction to gain a better understanding due to friction effects during a stepping motion. Three impact points are considered, by way of example and not limitation, to introduce the indeterminacy that this research is interested in addressing. Additional impact points may be considered as necessary to represent the bottom surface of the block. The numerical framework discussed in next section is developed for multiple point impact but can also be applied for single point impact problems. The equations of motion will first be rewritten and expressed as a function of an independent normal impulse parameter in differential form. Then, the derivation of the rigid body constraints among the impact points will be developed, including the consideration of the stick-slip transition. This is followed by presenting the generalized treatment of multiple point impact problems based on an interpretation of Stronge's hypothesis.

7.1 Equations of Motion

Examination of the impulsive forces requires a consideration of the impact forces in the equations of motion, which are also derived using Kane's method [70]. A definite integration over a very short time interval ϵ for the impact event,

$$\int_t^{t+\epsilon} (M(\mathbf{q})\ \ddot{\mathbf{q}}\ +\ \mathbf{b}(\mathbf{q},\dot{\mathbf{q}})\ +\ \mathbf{g}(\mathbf{q}))\ dt = \int_t^{t+\epsilon} J^T(\mathbf{q})\ \mathbf{F}\ dt \tag{7.1}$$

yields,

$$\boldsymbol{\vartheta}\ =\ \boldsymbol{\vartheta}(0)\ +\ \underbrace{JM^{-1}J^T}_{\beta}\ \mathbf{p}\ =\ \beta[\mathbf{p}_{t,A}\ p_{n,A}\ \mathbf{p}_{t,B}\ p_{n,B}\ \mathbf{p}_{t,C}\ p_{n,C}]^T \tag{7.2}$$

where M is the mass matrix, while $\mathbf{b}$ and $\mathbf{g}$ are vectors of Coriolis terms and gravity. The pre– and post-impact velocities are included in $\boldsymbol{\vartheta}(0)$ and $\boldsymbol{\vartheta}$, respectively, β describes the configuration and inertia properties of the system, where J is the *impact Jacobian matrix* that defines the configuration of the impact points. The Coriolis and

gravity vectors are omitted after the integration because the impact event is assumed to occur over an infinitesimally small duration ϵ in which the configuration remains constant. Note also that $\mathbf{p}_{t,i} = [p_{t1,i} \mid p_{t2,i}]^T$ since slip is now two-dimensional for 3D impact. The differential form of (7.2) is,

$$d\boldsymbol{\vartheta} \;=\; \beta[d\mathbf{p}_{t,A}\; dp_{n,A}\; d\mathbf{p}_{t,B}\; dp_{n,B}\; d\mathbf{p}_{t,C}\; dp_{n,C}]^T \tag{7.3}$$

Coulomb friction is used to relate the change in the magnitude of the normal impulse to the change in tangential impulse during sliding by using a coefficient of friction μ_i, such that $||d\mathbf{p}_{t,i}|| = \mu_i \; |dp_{n,i}|$. The relation written for point A gives,

$$d\mathbf{p}_{t,A} = \begin{bmatrix} dp_{t1,A} \\ dp_{t2,A} \end{bmatrix} = \begin{bmatrix} -\mu_A \; cos\phi_A \\ -\mu_A \; sin\phi_A \end{bmatrix} \; |dp_{n,A}| \tag{7.4}$$

where,

$$cos\phi_A = \frac{v_{t1,A}}{\sqrt{{v_{t1,A}}^2 + {v_{t2,A}}^2}} \qquad sin\phi_A = \frac{v_{t2,A}}{\sqrt{{v_{t1,A}}^2 + {v_{t2,A}}^2}} \tag{7.5}$$

Similar expressions can be obtained for points B and C but are not presented here in the interest of space and unnecessary repetition. The analysis up to this point has been carried out in Cartesian coordinates, see [25, 5]. Given the issues associated with friction and the sliding direction ϕ_i on the slip plane, a cylindrical coordinate formulation is more appropriate moving forward. The transformations for the velocity components of point A yield,

$$\boldsymbol{\vartheta}_A \;=\; \begin{bmatrix} v_{t1,A} \\ v_{t2,A} \\ v_{n,A} \end{bmatrix} \;=\; \begin{bmatrix} s_A \; cos\phi_A \\ s_A \; sin\phi_A \\ v_{n,A} \end{bmatrix} \tag{7.6}$$

where $s_A = \sqrt{{v_{t1,A}}^2 + {v_{t2,A}}^2}$ and $tan^{-1}(\phi_A) = (v_{t2,A}/v_{t1,A})$. Before implementing these relations into (7.3), a differentiation of (7.6) is needed, which gives,

$$d\boldsymbol{\vartheta}_A = \begin{bmatrix} dv_{t1,A} \\ dv_{t2,A} \\ dv_{n,A} \end{bmatrix} = \begin{bmatrix} cos\phi_A & -s_A\, sin\phi_A & 0 \\ sin\phi_A & s_A\, cos\phi_A & 0 \\ 0 & 0 & 1 \end{bmatrix} \begin{bmatrix} ds_A \\ d\phi_A \\ dv_{n,A} \end{bmatrix} = P_A \begin{bmatrix} ds_A \\ d\phi_A \\ dv_{n,A} \end{bmatrix} \tag{7.7}$$

Similar expressions to (7.7) can be obtained for points B and C with corresponding terms on the right-hand side. Collecting coefficients into a matrix $A = diag[P_A, P_B, P_C]$, in which $A \in \mathrm{R}^{9X9}$ and solving for the sliding velocity, sliding direction and normal velocity of each impact point using (7.3) yields,

$$\begin{bmatrix} ds_A \\ d\phi_A \\ dv_{n,A} \\ ds_B \\ d\phi_B \\ dv_{n,B} \\ ds_C \\ d\phi_C \\ dv_{n,C} \end{bmatrix} = \begin{bmatrix} A \end{bmatrix}^{-1} \beta \begin{bmatrix} -\mu_A c_A & 0 & 0 \\ -\mu_A s_A & 0 & 0 \\ 1 & 0 & 0 \\ 0 & -\mu_B c_B & 0 \\ 0 & -\mu_B s_B & 0 \\ 0 & 1 & 0 \\ 0 & 0 & -\mu_C c_C \\ 0 & 0 & -\mu_C s_C \\ 0 & 0 & 1 \end{bmatrix} \begin{bmatrix} |dp_{n,A}| \\ |dp_{n,B}| \\ |dp_{n,C}| \end{bmatrix} \tag{7.8}$$

The matrix A is invertible as long as the sliding velocity of impact point A, B and C are non-zero; in other words $s_A = s_B = s_C \neq 0$. Otherwise, a singularity arises and matrix A is no longer invertible. Also, note that this scenario represents the point during a collision in which an impact point comes to rest at the stick-slip transition. To overcome this singularity, an event-based approach is used, similar to the contact detection scheme [39], to detect when any of the impact points reach the stick-slip transition. The numerical integration is halted and the stick-slip transition

is evaluated to determine if the impact point will slip-reverse or stick. The numerical integration is then restarted using the updated slip-state of the impact point until the impact event ends or another point comes to rest. Further details about the stick-slip transition are provided in Sec. 7.3.

7.2 Rigid Body Constraints

In Sec. 3.2, the application of the velocity constraints at the force level were derived using the dual properties of the impact Jacobian. Here, the constraints are found in differential form to be consistent with the remainder of the numerical framework. Consider for example two of the impact points (A and B) on the three-dimensional rocking block shown in Fig. 7.3. The rigid body constraint becomes,

$$(\mathbf{v}_A - \mathbf{v}_B) \cdot \frac{\mathbf{P}_{GA} - \mathbf{P}_{GB}}{|\mathbf{P}_{GA} - \mathbf{P}_{GB}|} \;=\; 0 \tag{7.9}$$

yields,

$$(v_{t1,A} - v_{t1,B})\overbrace{(-c_5 c_6)}^{x} \;+\; (v_{t2,A} - v_{t2,B})\overbrace{(-s_6 c_4 - s_4 s_5 c_6)}^{y}$$
$$+\; (v_{n,A} - v_{n,B})\underbrace{(-s_4 s_6 + s_5 c_4 c_6)}_{z} \;=\; 0 \tag{7.10}$$

Using the velocity-force projection method developed in Sec. 3.3, then (7.10) is equivalently expressed in differential form as,

$$(dp_{t1,A} - dp_{t1,B})x \;+\; (dp_{t2,A} - dp_{t2,B})y \;+\; (dp_{n,A} - dp_{n,B})z \;=\; 0 \tag{7.11}$$

The constraint C_{AB} between the differential impulses for points A and B results as,

$$|dp_{n,A}| \;=\; \underbrace{\left(\frac{\mu_B cos\phi_B \; x + \mu_B sin\phi_B \; y + z}{\mu_A cos\phi_A \; x + \mu_A sin\phi_A \; y + z}\right)}_{C_{AB}} |dp_{n,B}| \tag{7.12}$$

which provides a general form of the constraint between two arbitrarily configured impact points. Similarly, to obtain a rigid body constraint between points B and C, the same method is applied,

$$(\mathbf{v}_B - \mathbf{v}_C) \cdot \frac{\mathbf{P}_{GB} - \mathbf{P}_{GC}}{|\mathbf{P}_{GB} - \mathbf{P}_{GC}|} \;=\; 0 \tag{7.13}$$

yields,

$$(v_{t1,B} - v_{t1,C})\overbrace{(-s_6 c_5)}^{x} \;+\; (v_{t2,B} - v_{\square,C})\overbrace{(c_4 c_6 - s_4 s_5 s_6)}^{y}$$

$$+\; (v_{n,B} - v_{\square,C})\underbrace{(s_4 c_6 + s_5 s_6 c_4)}_{z} \;=\; 0 \tag{7.14}$$

equivalently,

$$(dp_{t1,B} - dp_{t1,C})x \;+\; (dp_{t2,B} - dp_{\square,C})y \;+\; (dp_{n,B} - dp_{\square,C})z \;=\; 0 \tag{7.15}$$

The subscript $\square$ is included to here to add further generality to the derivation of the constraint in (7.15). For instance, point C may impact a ground surface parallel to impact points A and B, or a wall surface perpendicular to the ground surface. In either case, the corresponding constraints among the differential impulses for points B and C are,

GROUND:

$$|dp_{n,C}| \;=\; \underbrace{\left(\frac{\mu_B cos\phi_B \; x + \mu_B sin\phi_B \; y + z}{\mu_C cos\phi_C \; x + \mu_C sin\phi_C \; y + z}\right)}_{C_{CB}} \; |dp_{n,B}| \tag{7.16}$$

WALL:

$$|dp_{n,C}| \;=\; \underbrace{\left(\frac{\mu_B cos\phi_B \; x + \mu_B sin\phi_B \; y + z}{\mu_C cos\phi_C \; x + y + \mu_C sin\phi_C \; z}\right)}_{C_{CB}} \; |dp_{n,B}| \tag{7.17}$$

The constraints derived from (7.12) and (7.16), or (7.17), are implemented in (7.8) in order to express the differential equations of motion as a function of a single, independent normal impulse parameter $|dp_{n,C}|$, without any loss of generality.

7.3 Evaluating the Stick-Slip Transition

When a point comes to rest at the stick-slip transition, there are two possible outcomes for three-dimensional impact [3, 4]: slip-reversal (S-R) and sticking (S). Consider, by way of example, that impact point A comes to rest and using (7.3), yields,

$$\begin{bmatrix} dv_{t1,A} \\ dv_{t2,A} \end{bmatrix} = \begin{bmatrix} 0 \\ 0 \end{bmatrix} = \begin{bmatrix} \mathbf{b}_{1,1-9} \\ \mathbf{b}_{2,1-9} \end{bmatrix} \begin{bmatrix} dp_{t1,A} \\ dp_{t2,A} \\ \vdots \end{bmatrix} \tag{7.18}$$

where $\mathbf{b}_{i,1-9}$ are row vectors of the matrix β. In addition, the Coulomb friction relation for point A is removed since the slip-state at the stick-slip transition needs to be determined. Solving for the tangential impulses yields,

$$\underbrace{\begin{bmatrix} dp_{t1,A} \\ dp_{t2,A} \end{bmatrix}}_{d\mathbf{p}_{t,A}} = \begin{bmatrix} b_{11} & b_{12} \\ b_{21} & b_{22} \end{bmatrix}^{-1} \begin{bmatrix} -\mathbf{b}_{1,3-9} \\ -\mathbf{b}_{2,3-9} \end{bmatrix} \begin{bmatrix} 1 \\ -\mu_B cos\phi_B \\ -\mu_B sin\phi_B \\ 1 \\ -\mu_C cos\phi_C \\ -\mu_C sin\phi_C \\ 1 \end{bmatrix} \begin{bmatrix} \frac{C_{AB}}{C_{CB}} \\ \frac{1}{C_{CB}} \\ 1 \end{bmatrix} |dp_{n,C}| \tag{7.19}$$

The no-slip condition from (2.3) is used to determine if an impact point will stick or slip-reverse.

$$||d\mathbf{p}_t|| \leq \mu_A |dp_n| \longrightarrow \frac{||d\mathbf{p}_{t,A}||}{|dp_{n,C}|} = \frac{\sqrt{d\mathbf{p}_{t,A}^T d\mathbf{p}_{t,A}}}{|dp_{n,C}|} = \bar{\mu}_A \leq \mu_A \tag{7.20}$$

where $\bar{\mu}_A$ is the critical coefficient of friction for stick for point A. For the impact point to remain in stick, $\mu_A \geq \bar{\mu}_A$ which imposes a lower bound on μ_A. If this condition is not met, then the impact point slip-reverses. It is also important to note that the calculation for this critical coefficient for stick is solely dependent on the

configuration and inertia properties of the system. Whereas, during initial sliding the sliding direction ϕ_i is unpredictable due to the nonlinearities of friction, this is not the case if an impact point slip-reverses. For a point that slip-reverses, the impact point slides in a constant, unique direction [81, 3, 4, 25] and determined by,

$$\widehat{\phi}_A \;=\; tan^{-1}\left(\frac{b_{11}b_{23} \;-\; b_{12}b_{13}}{b_{22}b_{13} \;-\; b_{23}b_{12}}\right) \tag{7.21}$$

by way of example for point A. The sliding direction after the stick-slip transition is a function of the configuration and inertia properties of the system [81, 3, 4, 25], which is similar to the determinate of the critical coefficient of friction. Otherwise, if stick prevails, then $\bar{\mu}_A$ is used instead of μ_A in the analysis.

7.4 Energy Dissipation

Next, the implementation of the work-energy theorem is discussed. The calculation of the work is given as the change in kinetic energy between the initial and final states of the impact as,

$$T_2 \;=\; T_1 \;+\; W_{1-2} \;=\; T_1 \;+\; U_1 \;-\; U_2 \;+\; (W_{1-2})_d \tag{7.22}$$

where T_i and U_i are the kinetic and potential energy at state i, and $(W_{1-2})_d$ is the non-conservative, or dissipative, work done on the system between states 1 and 2. In this work, the potential energy terms U_1 and U_2 are neglected due to the hard impact assumptions, or negligible deformation, from the strict adherence to rigid body modeling.

$$W_{1-2} \;=\; W \;=\; T_2 - T_1 \;=\; \frac{1}{2}\,\dot{\mathbf{q}}^T(t+\epsilon)M\;\dot{\mathbf{q}}(t+\epsilon) - \frac{1}{2}\,\dot{\mathbf{q}}^T(t)M\;\dot{\mathbf{q}}(t) \tag{7.23}$$

Consider the normal work done during a collision to be the integration of the dot product between the normal force and displacement as,

$$W_n \;=\; \int f_{n,A}\;dx_{n,A} \;+\; \int f_{n,B}\;dx_{n,B} \;+\; \int f_{n,C}\;dx_{n,C}$$

$$= \int |dp_{n,A}| \underbrace{\frac{dx_{n,A}}{dt}}_{v_{n,A}} + \int |dp_{n,B}| \underbrace{\frac{dx_{n,B}}{dt}}_{v_{n,B}} + \int |dp_{n,C}| \underbrace{\frac{dx_{n,C}}{dt}}_{v_{n,C}}$$

$$= \int \left(v_{n,A} \left(\frac{C_{AB}}{C_{CB}} \right) + v_{n,B} \left(\frac{1}{C_{CB}} \right) + v_{n,C} \right) |dp_{n,C}| \qquad (7.24)$$

where the rigid body constraints are implemented and the normal work is determined as a function of a single, independent normal impulse parameter. And written in differential form,

$$\frac{dW_n}{|dp_{n,C}|} = v_{n,A} \left(\frac{C_{AB}}{C_{CB}} \right) + v_{n,B} \left(\frac{1}{C_{CB}} \right) + v_{n,C} \qquad (7.25)$$

Notice that (7.25) is differentiated with respect to $|dp_{n,C}|$, similar to the form in (4.9). By equating (7.25) to zero yields the normal impulse $|p_{nc}|$ at the end of the compression phase for the system, which is a function of the normal velocities of the impact points and the constraint equations derived. Also, $|p_{nc}|$ and subsequently W_{nc} may change if the end of the impact event is not reached if an impact point comes to rest at the stick-slip transition. In the event that multiple shifts occur in the normal work plot, then the normal work curve for the latter shift is used with the ECOR to determine the net normal work W_{nf} for the impact event.

The set of first order, nonlinear ODE's in (7.8), the rigid body constraints in (7.12) and (7.16) or (7.17), and the normal work in (7.25) are formulated into a state function $\mathbf{x}$ as,

$$\frac{d\mathbf{x}}{|dp_{n,C}|} = f(|p_{n,C}|, \{s_{A,B,C}, \phi_{A,B,C}, v_{n,A,B,C}, W_n\}) \quad , \quad \mathbf{x}(0) \qquad (7.26)$$

where $\mathbf{x}(0)$ is a vector of the initial conditions for the variables that appear in (7.26). To solve the system of equations in (7.26), Matlab's *ode45* integrator is used, which is sufficient for the nonstiff equations that are encountered in (7.26).

Stronge's energetic coefficient of restitution (ECOR) is applied to determine the net normal work for an impact event as,

$$W_{nf} \;=\; (1 - e_*^2) W_{nc} \tag{7.27}$$

where $e_* \in [-1, 1]$ is a *global* ECOR which accounts for the energy dissipated by the system in an impact event. In this work, $e_* < 0$ means that in a simultaneous, multiple point collision subsequent impact events may begin while an initial impact event has not completed its compression phase. The value of e_* is usually not known in a predictive sense, unless a good understanding of the material properties and physical behavior of the system is accounted for, as in [63, 64], which is not the goal in this work. Alternately, e_* functions more as a parameter to estimate the energy dissipated and its value in the present framework can be selected to correlate with experimental studies of an equivalent system.

7.5 Summary

This chapter presents an extension of the methods used for the analytical framework to develop a numerical framework for treating 3D multiple point impact problems with friction. The complications that arise due to friction were presented, which make analytical solutions very difficult unless the impact configuration is collinear. The derivation of rigid body constraints are developed in differential form for an arbitrary configuration of impact points. The method for deriving these constraints has not changed and stands as the novel approach developed in this research for treating indeterminate contact and impact. Additional impact points may be considered due to the generalized nature of the approach. An event-based scheme is implemented to address the discontinuity that is encountered at the stick-slip transition for 3D impact

problems. This method offers an alternative technique to address this discontinuity that is inherent in the modeling of 3D impact problems.

Chapter 8

Simulation Results: Three-Dimensional Examples

In this section, simulation results for a sphere impact a corner formed by two wall planes perpendicular to a ground plane and a three-dimensional rocking block example are presented. These examples are analyzed to demonstrate that the developed numerical framework produces an approximation to physically consistent behaviors. In the following simulations, the static μ_s and dynamic μ_d coefficient of friction are 0.6 and 0.35 for all impacting surfaces. The stick-slip transition is a major characteristic behavior of multibody systems with contact and impact. The effects of this transition region will be apparent in the results obtained from the cases analyzed.

8.1 Example 4: Sphere Impacting a Corner

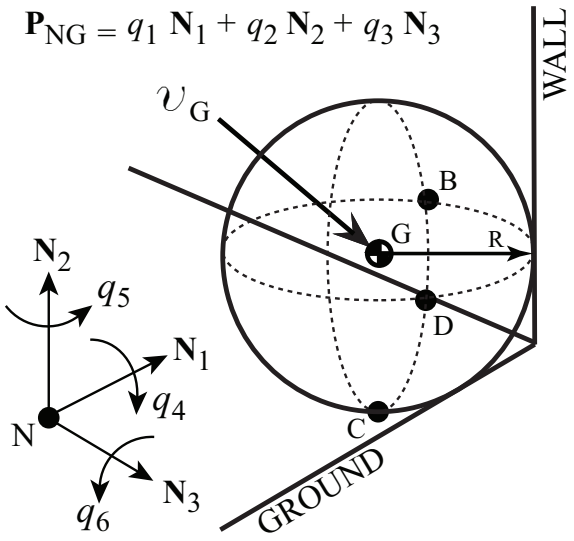

Figure 8.1. Three dimensional model of a sphere impacting a corner (repeated).

The three-dimensional model of the sphere introduced in Sec. 3.2, is shown in Fig. 8.1. The sphere has three impact points denoted by B, C, and D. This system has six degrees-of-freedom (DOF) defined by six generalized coordinates - three translation q_1, q_2, q_3 and three orientation q_4, q_5, q_6 coordinates. The sphere has mass, $m = 1\ kg$ and radius R = 0.50 m.

An arbitrary initial position and translational velocity was used for the ball simulation with no initial angular velocity. The simulation of the sphere is depicted in Fig. 8.2a, as it impacts a corner formed by the ground and two wall planes, and ends when a second impact is captured with the ground. This corner impact event is an indeterminate collision involving points B, C, and D. An $e_* = 0.50$ and $\mu_B = \mu_C = \mu_D = 0.35$ is used. After impacting the corner, the position of the impact points B, C, and D change which demonstrate the sphere's post-impact angular velocity as a result of impact. A plot of the system energy is shown in Fig. 8.3 to show energy consistency throughout the simulation.

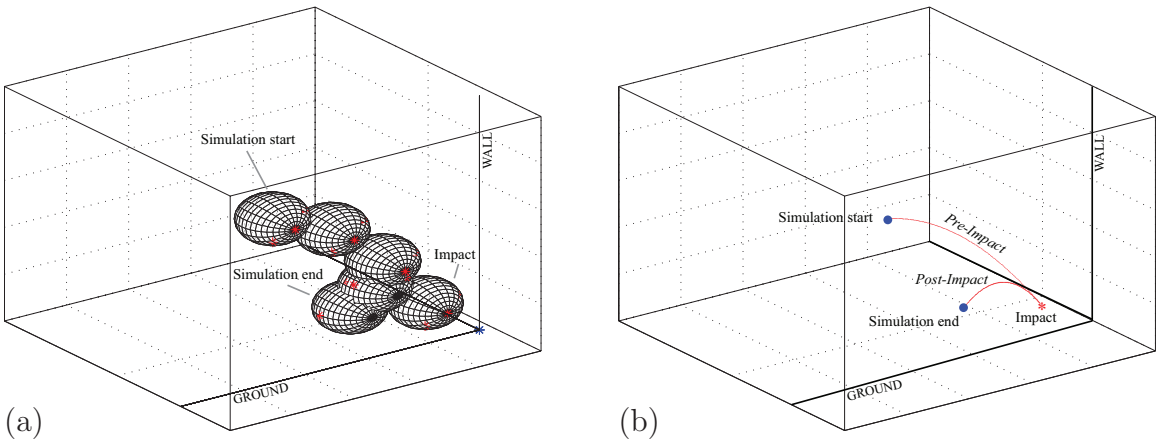

Figure 8.2. (a) Simulation results of the 3D sphere example impacting a corner and (b) trajectory of sphere's mass center.

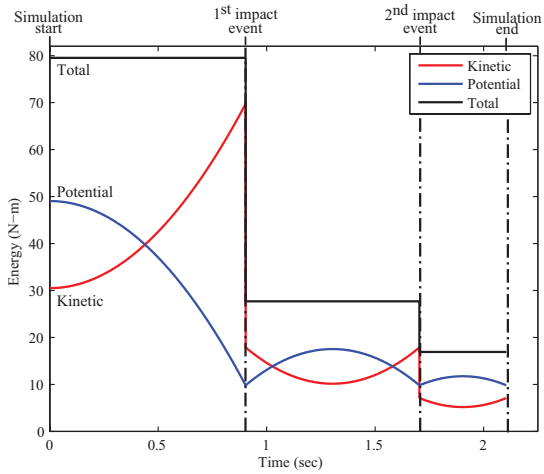

Figure 8.3. Energy consistency of the 3D sphere example impacting a corner.

The trajectory of the sphere's mass center throughout the simulation is shown in Fig. 8.2b. After impact, the sphere follows a lower trajectory which suggests that the system lost energy from the impact. This is supported by the energy plot in Fig. 8.3, which is further used to determine that no energy gains were encountered throughout the simulation.

The result of this three-dimensional case was obtained using the developed numerical framework. First, the impulse at the end of the compression phase was determined by (4.9) and used to find W_{nc}, and the net work done on the system W_{nf} with the *global* ECOR in (4.11). The evolution of the sliding velocities, sliding directions, and normal velocities were determined by the numerical integration of the system equations in (7.26) throughout the impact event, and shown in Fig. 8.4b. A plot of the normal work throughout the impact event is shown in Fig. 8.4a. In this particular simulation, none of the sliding velocities come to rest at the stick-slip transition, which result in no shifts in the normal work plot.

The end condition for the normal impulse $|p_{nf}|$ is evaluated with the knowledge of W_{nf}, which marks the end of the impact event. The post-impact velocities at the

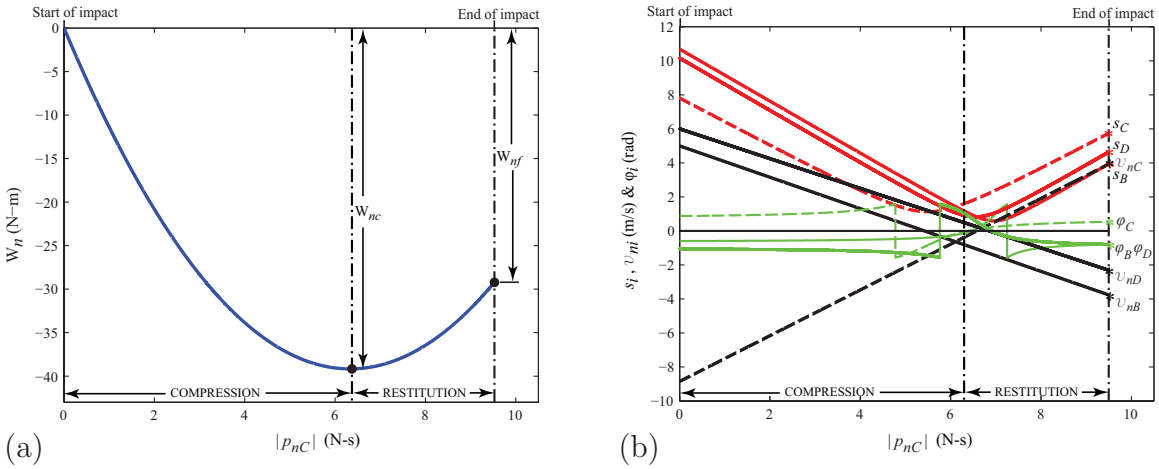

Figure 8.4. (a) Normal work done and (b) evolution of sliding velocities, sliding directions, and normal velocities throughout the impact event for the 3D sphere example.

impact end serve as the initial conditions for restarting the simulation to model the system after impact.

8.2 Example 5: Three-Dimensional Rocking Block

A three-dimensional model of a rocking block example, shown in Fig. 8.5, is analyzed here for the purposes of investigating an equivalent foot-ground contact interaction. The block model identifies three impact points, denoted by A, B, and C, which are located at the corner points of the block and its center of mass at point G. The system has six DOFs described by six generalized coordinates - three translation q_1, q_2, q_3 and three orientation q_4, q_5, q_6 coordinates. The block has length l, width b, and height h with mass $m = 2.5\ kg$.

Three separate cases are simulated with ground impact: 1) three corner impact points, 2) four corner impact points, and 3) three centered impact points. In all three cases, the simulation is started with points A and B in contact with the ground

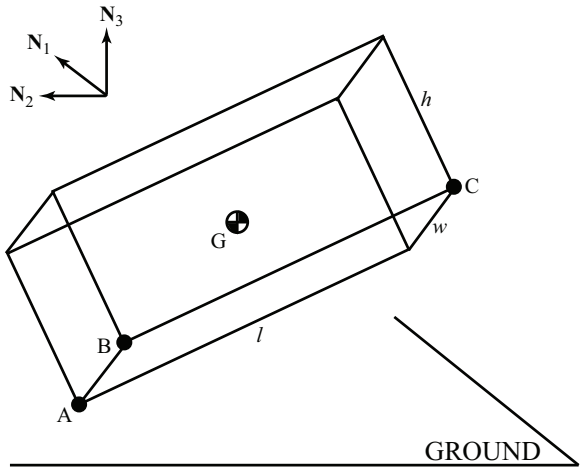

Figure 8.5. Three-dimensional model of a rocking block example with three corner impact points (repeated).

surface. The block is allowed to rock about these points initially in contact before impacting with point C (*Cases 1* and *3*) and points C and D (*Case 2*). It is assumed in the simulations that follow, that the contact and impact of the block's bottom surface with the ground occurs only at the points identified in Fig. 8.5. A static and dynamic coefficient of friction of 0.6 and 0.35 are used, with $e_* = 0.50$ for all three cases.

As in the planar case, contact constraints are enforced when points A and B are in contact with the ground, and the block rocks about these points. This means that the points in contact are not permitted to penetrate the ground using normal kinematic constraints but can slide or stick along the ground surface, or slip plane. Additionally, there is a short instance when all three points are simultaneously in contact with the ground. This introduces an indeterminacy in the equations of motion with respect to the impact forces, as introduced in Ch. 1. The constraint relationships developed in Sec. 7.2 are implemented to resolve the indeterminacy with the developed numerical framework.

8.2.1 Case 1: Three Corner Impact Points

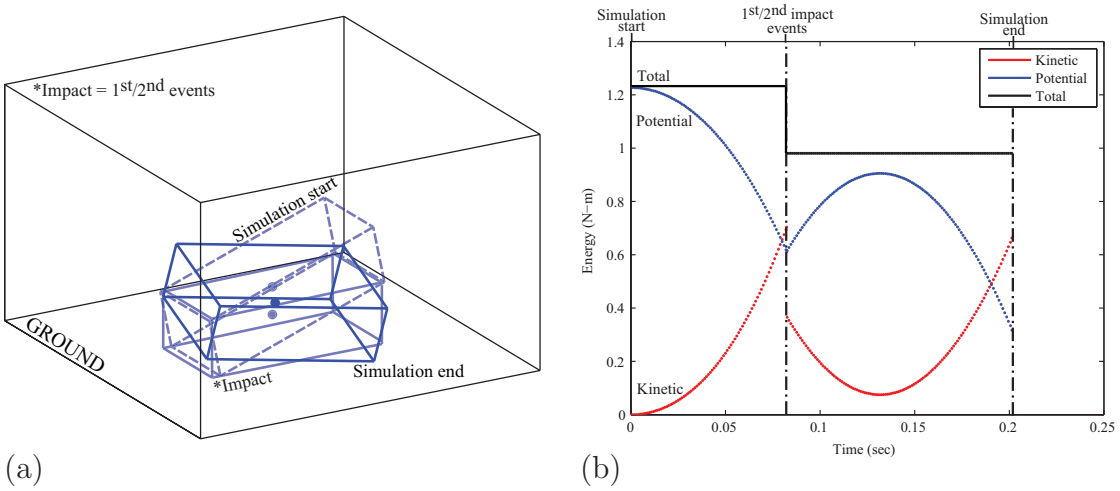

Figure 8.6. (a) Simulation of the 3D rocking block example with three corner impact points and (b) energy consistency for the simulation.

The results of the simulation are depicted in Fig. 8.6a. The block results in a post-impact angular velocity about a fictitious line from point A and C, with a slight rebound from the ground surface. A plot of the system energy is included in Fig. 8.6b to show energy consistency for the simulation performed. The collision of point C with the ground results in two impact events which are representative of the entire collision of the block with the ground. The first impact event is the only indeterminate one in the simulation, which involves the simultaneous impact of points A, B, and C. The post-impact velocity of point C at the end of the first impact event is negative which indicates that it is still moving toward the ground surface. This situation is interpreted as a second impact event involving only point C, a determinate collision. Furthermore, points A and B have a positive velocity after the first impact event,

which are interpreted as having reached their post-impact state. The second impact event is resolved before restarting the simulation.

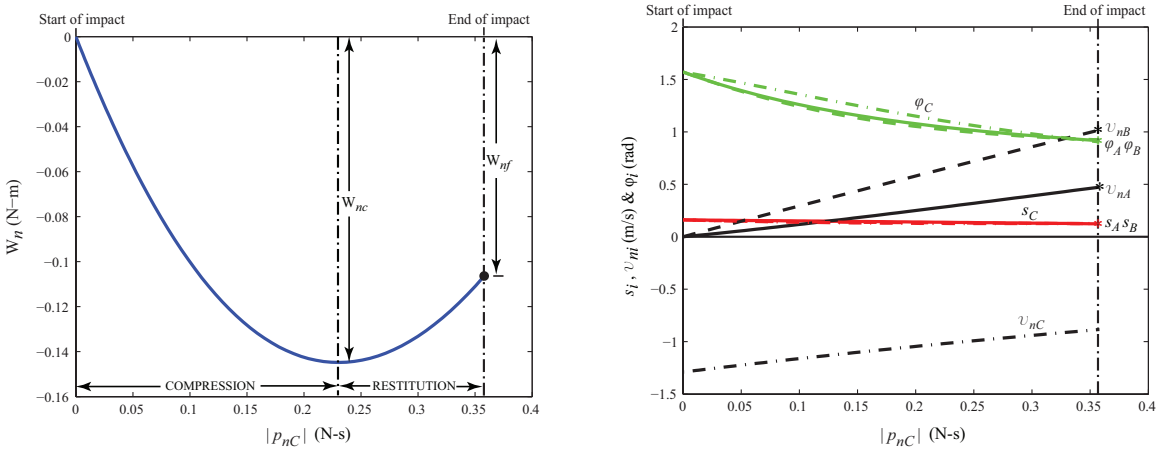

Figure 8.7. (a) Normal work done and (b) evolution of sliding velocities, sliding directions, and normal velocities throughout the first impact event for the 3D rocking block example with three corner impact points.

The result for this case is obtained by using *global* ECORs $e_* = 0.50, 0.50$ for the first and second impact events, respectively. The first impact event, illustrated in Fig. 8.7, shows a plot of the normal work and evolution of sliding velocities, sliding directions, and normal velocities. The inclusion of friction for this case does not cause the tangential velocities to come to rest at the stick-slip transition; this is almost the case at the end of the first impact event. Thus, the slope of the velocities never changes and the impact points maintain a slip-state of forward sliding throughout the impact event. The plot of the normal work in Fig. 8.7a shows its characteristic shape for the first impact event. Figure 8.7b shows how the states of points A and B reach their terminal value at the end of the first impact event. Meanwhile, the normal velocity of point C is negative which indicates that it is still impacting the ground

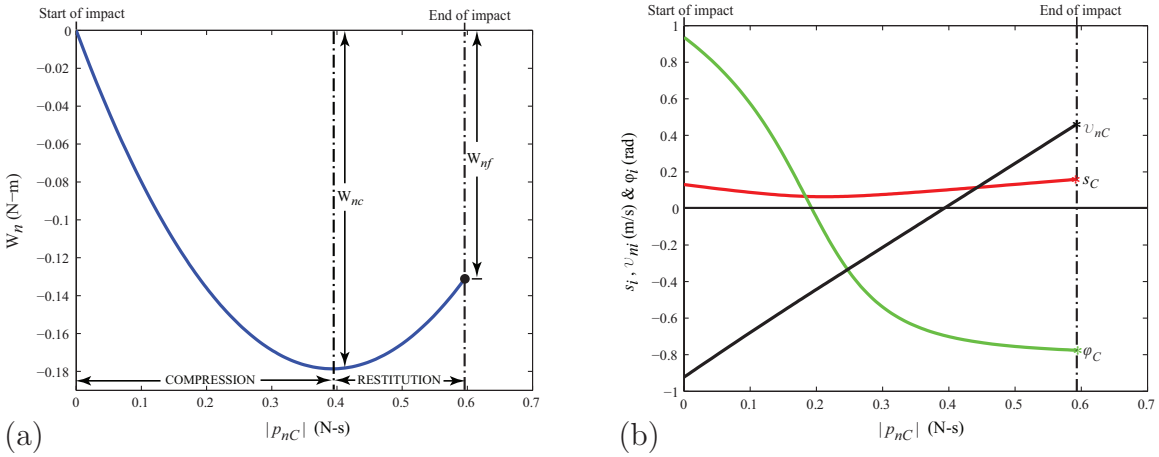

Figure 8.8. (a) Normal work done and (b) evolution of sliding velocities, sliding directions, and normal velocities throughout the second impact event for the 3D rocking block example with three corner impact points.

and initiates a second impact event. The analysis of the second impact event is shown in Fig. 8.8 and only involves point C. Figure 8.8a once again shows the characteristic parabolic shape of the normal work where a compression and restitution phase are clearly defined. Figure 8.8b shows how the state of point C reaches its terminal value.

The results from the analysis of a three-dimensional block with three corner impact points produced some insightful conclusions. The location of the impact points produced an effect on the post-impact behavior of the system. This can be obvious if one considers the balance of forces acting on a body, or system as a result of impact. Points A and C are balanced about the mass center but point B is not. This fact is consistent from the simulation, which resulted in a post-impact angular velocity of the block about a fictitious line from point A and C. The following case makes a first alternative to address the results from this case.

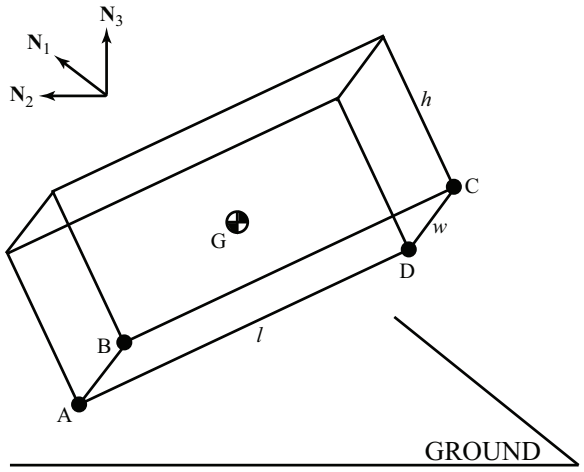

Figure 8.9. Three-dimensional model of a rocking block example with four corner impact points.

8.2.2 Case 2: Four Corner Impact Points

In the simulation presented here, an identical three-dimensional rocking block is considered, as in *Case 1*, aside from the number of impact points. Figure 8.9 depicts the block with four corner impact points denoted by A, B, C, and D. The consideration of an additional impact point means that an additional constraint is derived to account for this change but is straightforward using the developed framework. The goal is to determine if the number of impact points considered will affect the post-impact behavior of the system.

The results of the simulation are depicted in Fig. 8.10a. The block initially rocks about points A and B, and after impacting at points C and D, the block slightly rebounds in a forward direction. A plot of the system energy is included in Fig. 8.10b to show energy consistency for the simulation performed. The collision of points C and D with the ground results in two impact events which are representative of the entire collision of the block. The first impact event is the only indeterminate one in the simulation, which involves the simultaneous impact of points A, B, C, and D.

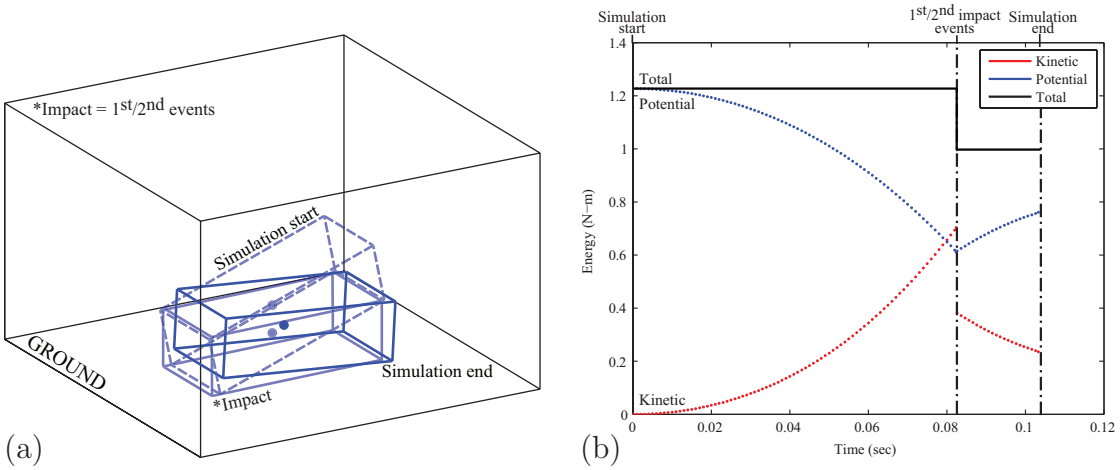

Figure 8.10. (a) Simulation of the 3D rocking block example with four corner impact points and (b) energy consistency for the simulation.

The post-impact velocity of points C and D at the end of the first impact event are negative which indicate that they are still moving toward the ground surface. This situation is interpreted as a second impact event involving only points C and D, a determinate collision. Furthermore, points A and B have a positive velocity after the first impact event, which are interpreted as having reached their post-impact state. The second impact event is resolved before restarting the simulation.

The result for this case is obtained by using *global* ECORs $e_* = 0.50, 0.50$ for the first and second impact events, respectively. The first impact event, illustrated in Fig. 8.11, shows a plot of the normal work and evolution of sliding velocities, sliding directions, and normal velocities. The inclusion of friction for this case does cause the tangential velocities to come to rest together at the stick-slip transition in the first impact event. An evaluation of the stick-slip transition results in slip-reversal, such that all three sliding velocities continue sliding in a constant direction. The plot of the normal work in Fig. 8.11a shows its characteristic shape for the first impact event. Figure 8.11b shows how the states of points A and B reach their terminal value at

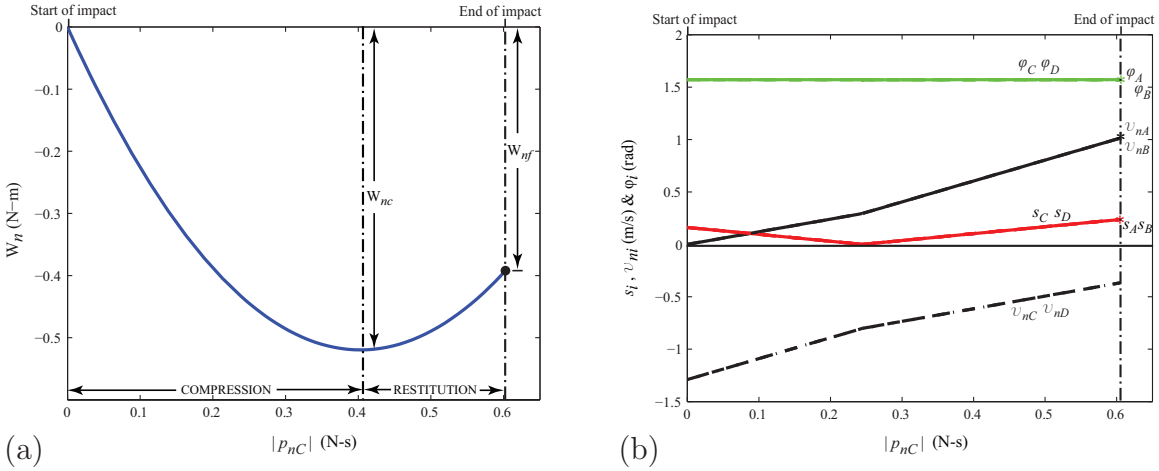

Figure 8.11. (a) Normal work done and (b) evolution of sliding velocities, sliding directions, and normal velocities throughout the first impact event for the 3D rocking block example with four corner impact points.

the end of the first impact event. Meanwhile, the normal velocity of points C and D are negative which indicate that they are still impacting the ground and initiates a second impact event. The analysis of the second impact event is shown in Fig. 8.12 and only involves points C and D. Figure 8.12a once again shows the characteristic parabolic shape of the normal work where a compression and restitution phase are clearly defined. Figure 8.12b shows how the state of points C and D reach their terminal value.

The results from this analysis produced a different result in comparison to *Case 1*. Once again, points A and C are balanced but unlike in *Case 1*, point B is balanced by point D. This fact is directly apparent from the result of the simulation, which is more consistent with what would be expected. Restated again: the block initially rocks about points A and B, and after impacting at points C and D, the block rebounds in a forward direction. The last case makes a second alternative to address the result from *Case 1*.

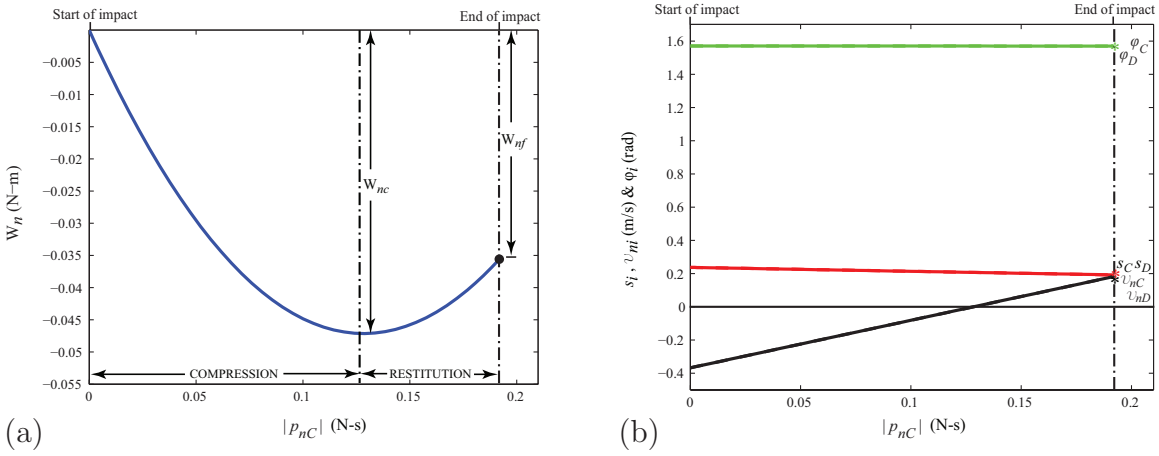

Figure 8.12. (a) Normal work done and (b) evolution of sliding velocities, sliding directions, and normal velocities throughout the second impact event for the 3D rocking block example with four corner impact points.

8.2.3 Case 3: Three Centered Impact Points

In the simulation presented here, an identical three-dimensional rocking block is considered, as in *Case 1*, aside from the location of the impact points. Figure 8.9 depicts top views of the block and the location of the three impact points considered in *Case 1* and *Case 3*. The goal is to determine if the location of the impact points considered will also affect the post-impact behavior of the system, similar to *Case 2*. It is important to note that points A, B, and C in this case enclose the mass center, as depicted in Fig. 8.9b.

The results of the simulation are depicted in Fig. 8.14a. The block initially rocks about points A and B, and after impacting at point C, the block slightly rebounds in a forward direction; this result is similar to the result from *Case 2*. A plot of the system energy is included in Fig. 8.14b to show energy consistency for the simulation performed. The collision of point C with the ground results in two impact events which are representative of the entire collision of the block. The first impact event is

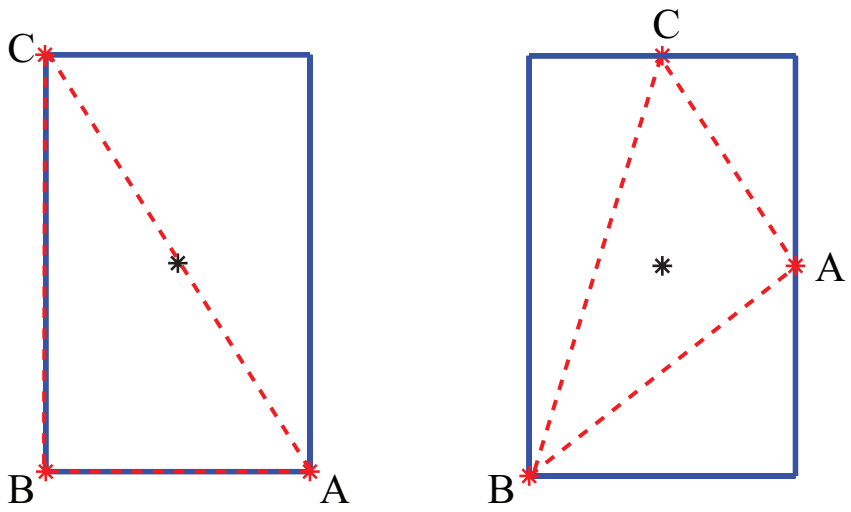

(a) (b)

Figure 8.13. Configuration of the (a) three corner impact points used for *Case 1* and (b) three centered impact points used for *Case 3*.

the only indeterminate one in the simulation, which involves the simultaneous impact of points A, B, and C. The post-impact velocity of point C at the end of the first impact event is negative which indicates that it is still moving toward the ground surface. This situation is interpreted as a second impact event involving only point C, a determinate collision. Furthermore, points A and B have a positive velocity after the first impact event, which are interpreted as having reached their post-impact state. The second impact event is resolved before restarting the simulation.

The result for this case is obtained by using *global* ECORs $e_* = 0.50, 0.50$ for the first and second impact events, respectively. The first impact event, illustrated in Fig. 8.15, shows a plot of the normal work and evolution of sliding velocities, sliding directions, and normal velocities. The inclusion of friction for this case does cause the tangential velocities to come to rest together at the stick-slip transition in the first impact event. Similar to the analysis from *Case 2*, the slip-states of the impact points

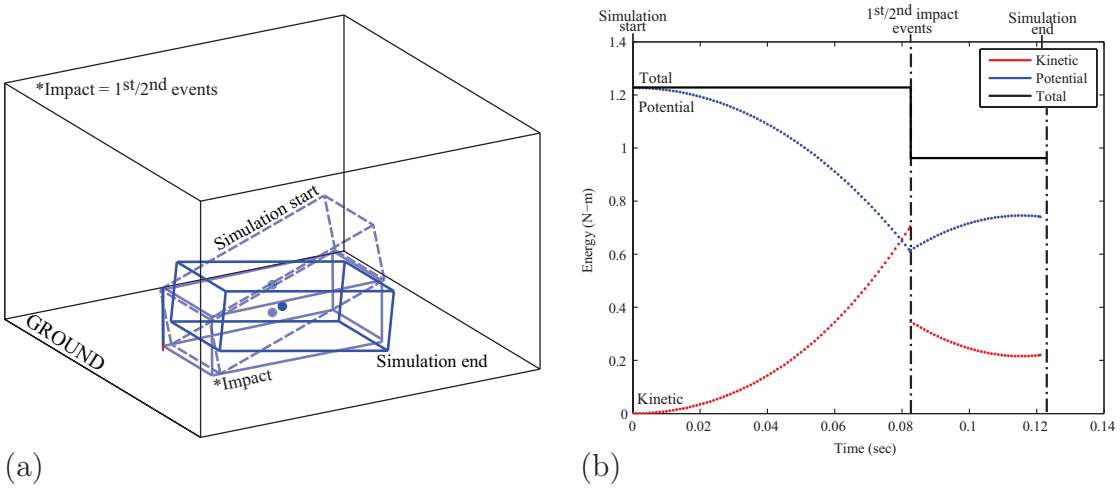

Figure 8.14. (a) Simulation of the 3D rocking block example with three centered impact points and (b) energy consistency for the simulation.

result in slip-reversal, such that they continue sliding in a constant direction. The plot of the normal work in Fig. 8.15a shows its characteristic shape for the first impact event. Figure 8.15b shows how the states of points A and B reach their terminal value at the end of the first impact event. Meanwhile, the normal velocity of point C is negative which indicates that it is still impacting the ground and initiates a second impact event. The analysis of the second impact event is shown in Fig. 8.16 and only involves point C. Figure 8.16a once again shows the characteristic parabolic shape of the normal work where a compression and restitution phase are clearly defined. Figure 8.16b shows how the state of point C reaches its terminal value.

The results from this analysis were very similar to that of *Case 2*, in which four impact points were considered. Thus, the simulation was also consistent with what would be expected for a block initially rocking about points A and B. The difference here is that as long as the location of the impact points is strategically selected in a stable configuration, then a reduced number of impact points can be used to achieve

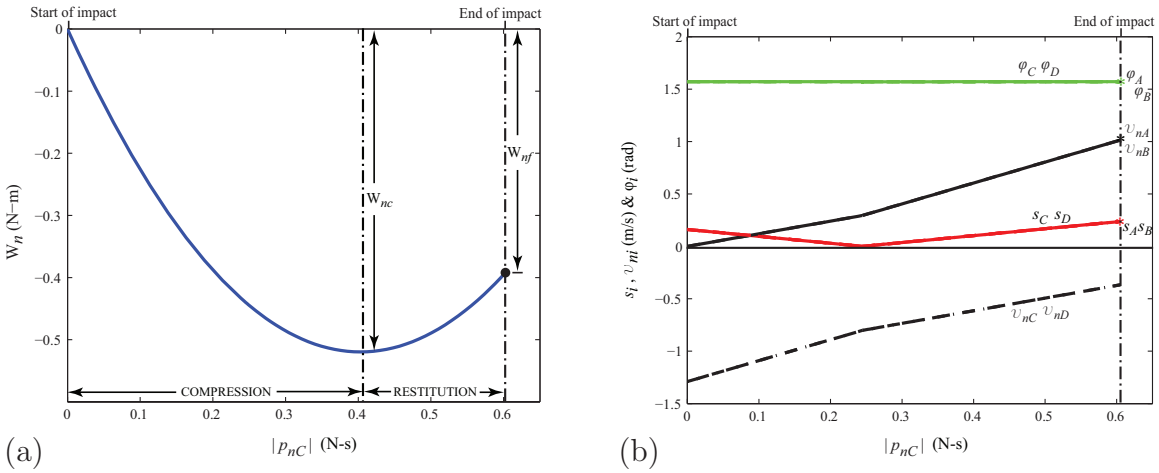

Figure 8.15. (a) Normal work done and (b) evolution of sliding velocities, sliding directions, and normal velocities throughout the first impact event for the 3D rocking block example with three centered impact points.

a physically consistent result. Three impact points represent the minimal number of points to define a surface and also reduces the number of constraints that need to be applied in the analysis. It is further concluded that the developed numerical framework performs well in the simulations conducted and can be extended to applications with multi-DOF robots that involve an equivalent foot-ground interaction.

8.3 Summary

This chapter performed a further study on two 3D example problems to test the numerical framework developed. The unique approach to treat indeterminate contact and impact, and modeling energy dissipation worked very well like it did for the planar problems. The total number and configuration of the impact points were varied to gain some insight about the effects in behavior of a 3D rocking block problem with friction, as an equivalent foot-ground interaction. The case in which only three points were considered demonstrated the ability to achieve physically consis-

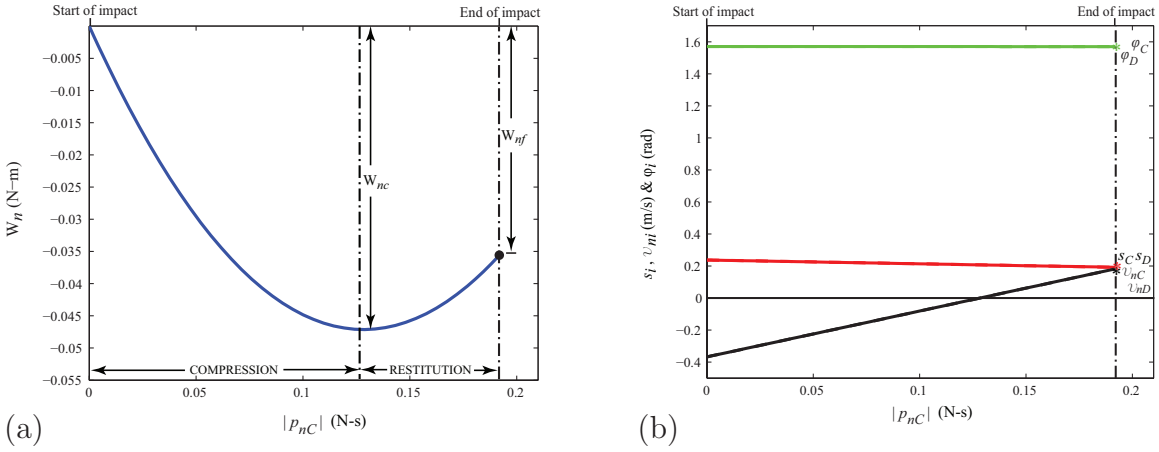

Figure 8.16. (a) Normal work done and (b) evolution of sliding velocities, sliding directions, and normal velocities throughout the second impact event for the 3D rocking block example with three centered impact points.

tent behavior by observation. The analysis of the 3D multiple point impact problems here demonstrates the effectiveness of the novel method developed in this research for addressing indeterminate contact and impact.

Appendix A

Constraint Projection Proof

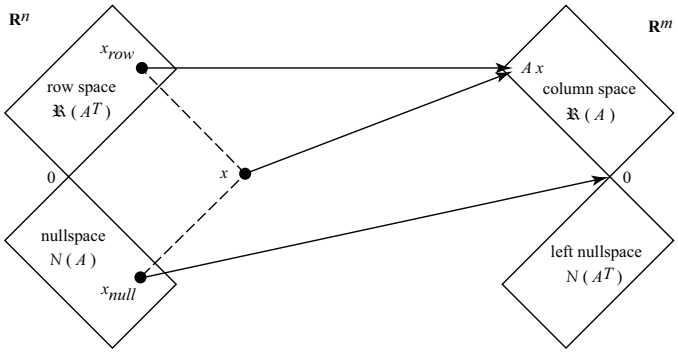

Figure A.1. Complementary subspaces.

In this appendix, an attempt is made to demonstrate the uniqueness of the solutions obtained in this work. The velocity constraints, which are consistent with rigid body assumptions, are derived as force constraints that are physically meaningful. As a result, these constraints lie in complementary subspaces, as in Fig. A.1 and are proven to show that multiple solutions do not exist. Beginning with the dual property of the Jacobian,

$$\boldsymbol{\vartheta} \;=\; J\;\dot{\mathbf{q}} \qquad\qquad \boldsymbol{\Gamma} \;=\; J^T\;\mathbf{F} \tag{A.1}$$

and using the principle of virtual work yields,

$$\mathbf{F}\cdot\delta\mathbf{x} \;=\; \Gamma\cdot\delta\mathbf{q} \qquad\longrightarrow\qquad \mathbf{F}\cdot\boldsymbol{\vartheta} \;=\; \Gamma\cdot\dot{\mathbf{q}} \tag{A.2}$$

where the δ operator corresponds to the virtual displacement. By applying the transpose to (A.2), it can be written as,

$$\mathbf{F}^T\boldsymbol{\vartheta} \;=\; \Gamma^T\dot{\mathbf{q}} \tag{A.3}$$

Replacing the full vector of velocities $\boldsymbol{\vartheta}$ on the right-hand side of (A.3) by the equivalent constraint matrix-reduced velocity vector representation, gives,

$$\mathbf{F}^T\;(Q\;\boldsymbol{\vartheta}^*) \;=\; \mathbf{F}^T\;Q\;(Q^+\boldsymbol{\vartheta}) \;=\; \mathbf{F}^T\;Q\;(Q^+J\;\dot{\mathbf{q}}) \;=\; \Gamma^T\dot{\mathbf{q}} \tag{A.4}$$

Using the existence of the left-inverse for the constraint matrix Q and its established relationship with the velocities in $\boldsymbol{\vartheta}$, then it can be shown that,

$$\mathbf{F}^T\ Q\ Q^+ J\ =\ \Gamma^T \qquad\qquad J^T\ (Q^+)^T\ \overbrace{Q^T\ \mathbf{F}}^{\mathbf{F}^*}\ =\ \Gamma \tag{A.5}$$

where $\mathbf{F}^*$ contains the constrained set of forces as a result of applying the constraint term Q. An equivalent relationship for the dual property of the Jacobian can be obtained from the result in (A.5) as,

$$\boldsymbol{\vartheta}^*\ =\ Q^+ J\ \dot{\mathbf{q}} \qquad\qquad \boldsymbol{\Gamma}\ =\ J^T\ (Q^+)^T\ \mathbf{F}^* \tag{A.6}$$

Thus, the constraint derivation between the $\boldsymbol{\vartheta}$-space and $\mathbf{F}$-space is summarized as follows. The velocity constraints are represented as,

$$\boldsymbol{\vartheta}\ =\ Q\ \boldsymbol{\vartheta}^* \tag{A.7}$$

and yield,

$$\boldsymbol{\vartheta} = J\ \dot{\mathbf{q}}\ =\ Q\ \boldsymbol{\vartheta}^* \quad \rightarrow \quad \boldsymbol{\vartheta}^*\ =\ Q^+ J\ \dot{\mathbf{q}} \tag{A.8}$$

using (A.1) and the result obtained by (A.5). The corresponding force constraint becomes,

$$\mathbf{F}\ =\ (Q^+)^T\ \mathbf{F}^* \qquad\qquad Q^T\ \mathbf{F}\ =\ \mathbf{F}^* \tag{A.9}$$

where Q^+ is the left-inverse of Q (and Q^T that of $(Q^+)^T$). It is important to note that the matrix $(Q^+)^T\ Q^T$ does not equal the identity matrix. In other words,

$$\mathbf{F}\ =\ \underbrace{\left(Q^+\right)^T Q^T}_{\neq I}\ \mathbf{F} \tag{A.10}$$

This matrix projects $\mathbf{F}$ on the right-hand-side of (A.10) into the space orthogonal to the velocity constraint, which must equal the original $\mathbf{F}$. Technically, any vector of forces in the null space of $(Q^+)^T\ Q^T$ can be added to the right-hand side and still

satisfy (A.10), see Fig. A.1. However, the development of this solution was based on the existence of left-inverses which only find a single solution. In addition, it is expected that adding constraints to a problem would select a particular single solution and not involve the problem of multiple solutions. To further demonstrate the uniqueness of the solutions obtained, a look at null space projections is considered.

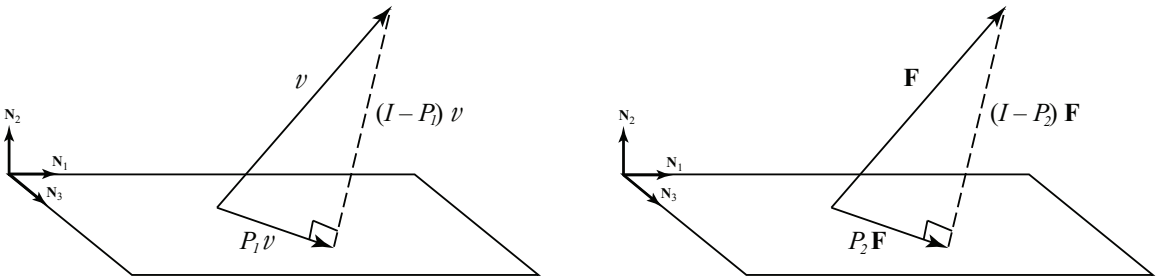

(a) (b)

Figure A.2. Constraint projections in (a) velocity space and (b) force space.

Let,

$$\boldsymbol{\vartheta} \;=\; \underbrace{Q\,Q^{+}}_{\neq I}\;\boldsymbol{\vartheta} \;=\; \underbrace{Q\,Q^{+}}_{P_1}\;\boldsymbol{\vartheta} \tag{A.11}$$

where P_1 is a projection of $\boldsymbol{\vartheta}$ onto the column space of Q, as shown in Fig. A.2,

$$\boldsymbol{\vartheta} \;=\; \underbrace{P_1\,\boldsymbol{\vartheta}}_{column\ \ space} \;+\; \underbrace{(I \;-\; P_1)\,\boldsymbol{\vartheta}}_{left-nullspace} \tag{A.12}$$

A similar projection is obtained by considering the forces and the projection of the constraints from the velocities,

$$\mathbf{F} \;=\; \underbrace{\left(Q^{+}\right)^{T} Q^{T}}_{P_2 \;=\; P_1^{T}}\;\mathbf{F} \tag{A.13}$$

where P_2 is a projection of $\mathbf{F}$ onto the column space of $(Q^{+})^{T}$, such that,

$$0 \;=\; \mathbf{F} \;-\; (Q^{+})^{T} Q^{T}\;\mathbf{F} \;=\; (I \;-\; (Q^{+})^{T} Q^{T})\;\mathbf{F} \;=\; \bar{a}\;(I \;-\; (Q^{+})^{T} Q^{T})\;\mathbf{F} \tag{A.14}$$

where $\bar{a}$ can be any vector or scalar term, yet the solution is preserved. Therefore, this presents a significant conclusion about the velocity and force constraints derived. The existence of a left-inverse for the constraint matrix Q shows that a solution also exists and is unique, which provides verification of the novel approached developed in this research.

Appendix B

Constraint and Slip-State Derivations

This appendix is included here to show how the constraints for some of the planar examples is derived to consider the various slip-states of an impact point. Consider for example two impact points, 1 and 2, located on a rigid body. Using classical rigid body dynamics [62], the difference between the velocities of these two impact points is found as,

$$\mathbf{v}_1 \; - \; \mathbf{v}_2 \; = \; \boldsymbol{\omega} \; \times \; (\mathbf{P}_{G1} \; - \; \mathbf{P}_{G2}) \tag{B.1}$$

where $\boldsymbol{\omega}$ is the angular velocity of the body and $\mathbf{P}_{Gi}$ is the position vector of impact point i with respect to the body's mass center. If the dot product of the unit direction between impact points 1 and 2 is applied to each side of (B.1), such that the right-hand side is zero, then the rigid body assumption defines that,

$$(\mathbf{v}_1 \; - \; \mathbf{v}_2) \; \cdot \; \frac{(\mathbf{P}_{G1} \; - \; \mathbf{P}_{G2})}{|(\mathbf{P}_{G1} \; - \; \mathbf{P}_{G2})|} \; = \; 0 \tag{B.2}$$

Additional rigid body constraints can be formulated using this method with the consideration of more impact points. The benefit is clear from the simple nature of (B.2) and permits the definition of a kinematic relationship among a collection of impact points on a rigid body.

B.1 Rocking Block

Evaluating the terms involved in the constraint for the planar rocking block yields,

$$(\; (v_{t1} - v_{t2}) \; \mathbf{N}_1 + (v_{n1} - v_{n2}) \; \mathbf{N}_2 \;) \cdot (-\mathbf{N_1}) \; = \; v_{t1} \; - \; v_{t2} \; = \; 0 \tag{B.3}$$

The velocity constraint obtained in (B.3) is used to constrain one of the tangential velocities. Consider an example where v_{t1} is constrained. This is accomplished by solving for this velocity term and substituting the expression into (B.5) which gives,

$$\boldsymbol{\vartheta} \;=\; \begin{bmatrix} v_{t1} \\ v_{n1} \\ v_{t2} \\ v_{n2} \end{bmatrix} \;=\; \begin{bmatrix} v_{t2} \\ v_{n1} \\ v_{t2} \\ v_{n2} \end{bmatrix} \;=\; \begin{bmatrix} 0 & 1 & 0 \\ 1 & 0 & 0 \\ 0 & 1 & 0 \\ 0 & 0 & 1 \end{bmatrix} \begin{bmatrix} v_{n1} \\ v_{t2} \\ v_{n2} \end{bmatrix} \;=\; Q\ \boldsymbol{\vartheta}^* \tag{B.4}$$

where Q is a matrix of full rank containing the velocity constraint and $\boldsymbol{\vartheta}^*$ contains the constrained velocity space. The dual property of the impact Jacobian defines a relationship between velocities and forces, which is derived based on the principle of virtual work and conservation of energy theory [82],

$$\boldsymbol{\vartheta} \;=\; \begin{bmatrix} v_{t1} \\ v_{n1} \\ v_{t2} \\ v_{n2} \end{bmatrix} \;=\; J\ \dot{\mathbf{q}}\ , \quad \boldsymbol{\Gamma} = J^T\ \mathbf{F} \;=\; J^T \begin{bmatrix} f_{t1} \\ f_{n1} \\ f_{t2} \\ f_{n2} \end{bmatrix} \tag{B.5}$$

such that,

$$\boldsymbol{\Gamma} \;=\; J^T\ \mathbf{F} \;=\; J^T\ (Q^+)^T\ \mathbf{F}^* \tag{B.6}$$

The relationship in (B.6) yields,

$$\mathbf{F} \;=\; \left(Q^+\right)^T\ \mathbf{F}^* \qquad \text{or} \qquad Q^T\ \mathbf{F} \;=\; \mathbf{F}^* \tag{B.7}$$

where Q^+ is the left-inverse of Q. It is incorrect to assume that the constrained force space $\mathbf{F}^*$ will involve the same terms as in the constrained velocity space $\boldsymbol{\vartheta}^*$. Therefore, consider the second expression in (B.7) where $\mathbf{F}^*$ is solved as,

$$\mathbf{F}^* \;=\; Q^T\ \mathbf{F} \;=\; \begin{bmatrix} 0 & 1 & 0 & 0 \\ 1 & 0 & 1 & 0 \\ 0 & 0 & 0 & 1 \end{bmatrix} \begin{bmatrix} f_{t1} \\ f_{n1} \\ f_{t2} \\ f_{n2} \end{bmatrix} \;=\; \begin{bmatrix} f_{n1} \\ f_{t1} \;+\; f_{t2} \\ f_{n2} \end{bmatrix} \tag{B.8}$$

such that,

$$\begin{bmatrix} f_{t1} \\ f_{n1} \\ f_{t2} \\ f_{n2} \end{bmatrix} = \mathbf{F} = (Q^+)^T \mathbf{F}^* = \begin{bmatrix} 0 & 0.5 & 0 \\ 1 & 0 & 0 \\ 0 & 0.5 & 0 \\ 0 & 0 & 1 \end{bmatrix} \begin{bmatrix} f_{n1} \\ f_{t1} + f_{t2} \\ f_{n2} \end{bmatrix} = \begin{bmatrix} 0.5\,(f_{t1} + f_{t2}) \\ f_{n1} \\ 0.5\,(f_{t1} + f_{t2}) \\ f_{n2} \end{bmatrix} \tag{B.9}$$

The first and third relations yield the same force constraint,

$$f_{t1} - f_{t2} = 0 \tag{B.10}$$

Applying a definite integration of (B.10), the constraint is expressed in terms of impulses as,

$$p_{t1} - p_{t2} = 0 \tag{B.11}$$

Note that for a frictionless case ($\mu_i = 0$) the tangential forces vanish, which eliminates the indeterminacy in the system equations of motion.

B.1.1 Initial Sliding, Slip-Resumption and Slip-Reversal

Incorporating Coulomb friction gives,

$$-sgn(v_{t1})\mu_1 \, |p_{n1}| + sgn(v_{t2})\mu_2 \, |p_{n2}| = 0 \tag{B.12}$$

such that,

$$|p_{n2}| = \left(\frac{sgn(v_{t1})\mu_1}{sgn(v_{t2})\mu_2}\right) |p_{n1}| = C_{block} \, |p_{n1}| \tag{B.13}$$

B.1.2 Sticking

Consider for example that v_{t2} is in stick and incorporating Coulomb friction for v_{t1} gives,

$$-sgn(v_{t1})\mu_1 \, |p_{n1}| - p_{t2} = 0 \tag{B.14}$$

and substituting the expression for p_{t2} given by the velocity constraint among the impulse terms in the case of stick yields,

$$-sgn(v_{t1})\mu_1 \ |p_{n1}| \ - \ \left[\left(\frac{sgn(v_{t1})\mu_1 a_{31} - a_{32}}{a_{33}}\right)|p_{n1}| \ - \ \left(\frac{a_{34}}{a_{33}}\right)|p_{n2}|\right] \ = \ 0 \quad \text{(B.15)}$$

such that,

$$|p_{n2}| \ = \ \left(\frac{sgn(v_{t1})\mu_1(a_{31}+a_{33}) - a_{32}}{a_{34}}\right) \ |p_{n1}| \ = \ C_{block} \ |p_{n1}| \quad \text{(B.16)}$$

B.2 Planar Ball

Evaluating the terms involved in the constraint for the planar ball shown in Fig. 6.1b yields,

$$\begin{aligned}(\ (v_{t1} \ - \ v_{n2}) \ \mathbf{N}_1 \ + \ (v_{n1} \ - \ v_{t2}) \ \mathbf{N}_2 \ ) \ \cdot \ \left(-\frac{1}{\sqrt{2}} \ \mathbf{N_1} \ - \ \frac{1}{\sqrt{2}} \ \mathbf{N_2}\right) \\ = \ -v_{t1} \ - \ v_{n1} \ + \ v_{t2} \ + \ v_{n2} \ = \ 0 \end{aligned} \quad \text{(B.17)}$$

The velocity constraint obtained in (B.17) is used to constrain one of the tangential velocities. Consider an example where v_{t1} is constrained. This is accomplished by solving for this velocity term in (B.17) which gives,

$$\boldsymbol{\vartheta} \ = \ \begin{bmatrix} v_{t1} \\ v_{n1} \\ v_{t2} \\ v_{n2} \end{bmatrix} \ = \ \begin{bmatrix} -v_{n1} \ + \ v_{t2} \ + \ v_{n2} \\ v_{n1} \\ v_{t2} \\ v_{n2} \end{bmatrix} \ = \ \begin{bmatrix} -1 & 1 & 1 \\ 1 & 0 & 0 \\ 0 & 1 & 0 \\ 0 & 0 & 1 \end{bmatrix} \begin{bmatrix} v_{n1} \\ v_{t2} \\ v_{n2} \end{bmatrix} \ = \ Q \ \boldsymbol{\vartheta}^* \quad \text{(B.18)}$$

where Q is a matrix of full rank containing the velocity constraint and $\boldsymbol{\vartheta}^*$ contains the constrained velocity space. Applying the dual property of the impact Jacobian and solving for the constrained force space, yields,

$$\mathbf{F}^* \;=\; Q^T\,\mathbf{F} \;=\; \begin{bmatrix} -1 & 1 & 0 & 0 \\ 1 & 0 & 1 & 0 \\ 1 & 0 & 0 & 1 \end{bmatrix} \begin{bmatrix} f_{t1} \\ f_{n1} \\ f_{t2} \\ f_{n2} \end{bmatrix} \;=\; \begin{bmatrix} -f_{t1} \;+\; f_{n1} \\ f_{t1} \;+\; f_{t2} \\ f_{t1} \;+\; f_{n2} \end{bmatrix} \tag{B.19}$$

Using this result in the first relation in (B.7) gives,

$$\begin{bmatrix} f_{t1} \\ f_{n1} \\ f_{t2} \\ f_{n2} \end{bmatrix} \;=\; \mathbf{F} \;=\; (Q^+)^T\,\mathbf{F}^* \;=\; \begin{bmatrix} -0.25 & 0.25 & 0.25 \\ 0.75 & 0.25 & 0.25 \\ 0.25 & 0.75 & -0.25 \\ 0.25 & -0.25 & 0.75 \end{bmatrix} \begin{bmatrix} -f_{t1} \;+\; f_{n1} \\ f_{t1} \;+\; f_{t2} \\ f_{t1} \;+\; f_{n2} \end{bmatrix}$$

$$= \begin{bmatrix} 0.75f_{t1} \;-\; 0.25f_{n1} \;+\; 0.25f_{t2} \;+\; 0.25f_{n2} \\ -0.25f_{t1} \;+\; 0.75f_{n1} \;+\; 0.25f_{t2} \;+\; 0.25f_{n2} \\ 0.25f_{t1} \;+\; 0.25f_{n1} \;+\; 0.75f_{t2} \;-\; 0.25f_{n2} \\ 0.25f_{t1} \;+\; 0.25f_{n1} \;-\; 0.25f_{t2} \;+\; 0.75f_{n2} \end{bmatrix} \tag{B.20}$$

such that every relation in (B.20) yields the same force constraint:

$$f_{t1} \;+\; f_{n1} \;-\; f_{t2} \;-\; f_{n2} \;=\; 0 \tag{B.21}$$

Applying a definite integration of (B.21), the constraint is expressed in terms of impulses as,

$$p_{t1} \;+\; p_{n1} \;-\; p_{t2} \;-\; p_{n2} \;=\; 0 \tag{B.22}$$

Note again that for a frictionless case ($\mu_i = 0$) the tangential forces vanish, which eliminates the indeterminacy in the system equations of motion.

B.2.1 Initial Sliding, Slip-Resumption and Slip-Reversal

Applying the magnitude on the normal impulse terms in (B.22) and incorporating Coulomb friction gives,

$$-sgn(v_{t1})\mu_1 \; |p_{n1}| \; + \; |p_{n1}| \; + \; sgn(v_{t2})\mu_2 \; |p_{n2}| \; - \; |p_{n2}| \; = \; 0 \tag{B.23}$$

such that,

$$|p_{n2}| \; = \; \left(\frac{1 - sgn(v_{t1})\mu_1}{1 - sgn(v_{t2})\mu_2}\right) \; |p_{n1}| \; = \; C_{ball} \; |p_{n1}| \tag{B.24}$$

B.2.2 Sticking

Consider for example that v_{t2} is in stick, while v_{t1} remains sliding and applying the magnitude on the normal impulse terms in (B.22) gives,

$$-sgn(v_{t1})\mu_1 \; |p_{n1}| \; + \; |p_{n1}| \; - \; p_{t2} \; - \; |p_{n2}| \; = \; 0 \tag{B.25}$$

and substituting the expression for p_{t2} given by the velocity constraint among the impulse terms in the case of stick yields,

$$-sgn(v_{t1})\mu_1 \; |p_{n1}| + |p_{n1}| - \left[\left(\frac{sgn(v_{t1})\mu_1 a_{31} - a_{32}}{a_{33}}\right) |p_{n1}| - \left(\frac{a_{34}}{a_{33}}\right) |p_{n2}|\right] - |p_{n2}| \; = \; 0 \tag{B.26}$$

such that,

$$|p_{n2}| \; = \; \left(\frac{-sgn(v_{t1})\mu_1(a_{31} + a_{33}) + a_{32} + a_{33}}{a_{33} - a_{34}}\right) \; |p_{n1}| \; = \; C_{ball} \; |p_{n1}| \tag{B.27}$$

B.3 Three-Ball Newton's Cradle

Evaluating the terms involved in the constraint for the three-ball Newton's Cradle shown in Fig. 6.11b yields,

$$(\; (v_4 - v_6) \; \mathbf{N}_1 + (v_3 - v_5) \; \mathbf{N}_2 \;) \cdot (-\mathbf{N_2}) \; = \; v_5 - v_3 \; = \; 0 \tag{B.28}$$

The velocity constraint obtained in (B.28) is used to constrain one of the tangential velocities. Consider an example where v_{t1} is constrained. This is accomplished by solving for this velocity term in (B.28) which gives,

$$\boldsymbol{\vartheta} = \begin{bmatrix} v_1 \\ v_2 \\ v_3 \\ v_4 \\ v_5 \\ v_6 \\ v_7 \\ v_8 \end{bmatrix} = \begin{bmatrix} v_1 \\ v_2 \\ v_3 \\ v_4 \\ v_3 \\ v_6 \\ v_7 \\ v_8 \end{bmatrix} = \begin{bmatrix} 1 & 0 & 0 & 0 & 0 & 0 & 0 \\ 0 & 1 & 0 & 0 & 0 & 0 & 0 \\ 0 & 0 & 1 & 0 & 0 & 0 & 0 \\ 0 & 0 & 0 & 1 & 0 & 0 & 0 \\ 0 & 0 & 1 & 0 & 0 & 0 & 0 \\ 0 & 0 & 0 & 0 & 1 & 0 & 0 \\ 0 & 0 & 0 & 0 & 0 & 1 & 0 \\ 0 & 0 & 0 & 0 & 0 & 0 & 1 \end{bmatrix} \begin{bmatrix} v_1 \\ v_2 \\ v_3 \\ v_4 \\ v_6 \\ v_7 \\ v_8 \end{bmatrix} = Q\ v^* \qquad \text{(B.29)}$$

where Q is a matrix of full rank containing the velocity constraint and $\boldsymbol{\vartheta}^*$ contains the constrained velocity space. Applying the dual property of the impact Jacobian and solving for the constrained force space, yields,

$$\mathbf{F}^* = Q^T\ \mathbf{F} = \begin{bmatrix} 1 & 0 & 0 & 0 & 0 & 0 & 0 & 0 \\ 0 & 1 & 0 & 0 & 0 & 0 & 0 & 0 \\ 0 & 0 & 1 & 0 & 1 & 0 & 0 & 0 \\ 0 & 0 & 0 & 1 & 0 & 0 & 0 & 0 \\ 0 & 0 & 0 & 0 & 0 & 1 & 0 & 0 \\ 0 & 0 & 0 & 0 & 0 & 0 & 1 & 0 \\ 0 & 0 & 0 & 0 & 0 & 0 & 0 & 1 \end{bmatrix} \begin{bmatrix} f_1 \\ f_2 \\ f_3 \\ f_4 \\ f_5 \\ f_6 \\ f_7 \\ f_8 \end{bmatrix} = \begin{bmatrix} f_1 \\ f_2 \\ f_3 + f_5 \\ f_4 \\ f_6 \\ f_7 \\ f_8 \end{bmatrix} \qquad \text{(B.30)}$$

Using this result in the first relation in (B.28) gives,

$$\begin{bmatrix} f_1 \\ f_2 \\ f_3 \\ f_4 \\ f_5 \\ f_6 \\ f_7 \\ f_8 \end{bmatrix} = \mathbf{F} = (Q^+)^T \mathbf{F}^* = \begin{bmatrix} 1 & 0 & 0 & 0 & 0 & 0 & 0 \\ 0 & 1 & 0 & 0 & 0 & 0 & 0 \\ 0 & 0 & 0.5 & 0 & 0 & 0 & 0 \\ 0 & 0 & 0 & 1 & 0 & 0 & 0 \\ 0 & 0 & 0.5 & 0 & 0 & 0 & 0 \\ 0 & 0 & 0 & 0 & 1 & 0 & 0 \\ 0 & 0 & 0 & 0 & 0 & 1 & 0 \\ 0 & 0 & 0 & 0 & 0 & 0 & 1 \end{bmatrix} \begin{bmatrix} f_1 \\ f_2 \\ f_3 + f_5 \\ f_4 \\ f_6 \\ f_7 \\ f_8 \end{bmatrix}$$

$$= [f_1 \mid f_2 \mid 0.5(f_3 + f_5) \mid f_4 \mid 0.5(f_3 + f_5) \mid f_6 \mid f_7 \mid f_8]^T \tag{B.31}$$

such that every relation in (B.31) yields the same force constraint:

$$f_3 - f_5 = 0 \tag{B.32}$$

Applying a definite integration of (B.32), the constraint is expressed in terms of impulses as,

$$p_3 - p_5 = 0 \tag{B.33}$$

Due to the physical nature of this example, the effects of the stick-slip transition do not arise. Therefore, a consideration of the different slip-states of an impact are not developed for this example.

Appendix C

Equations of Motion: Kane's Method

Kane's method is an approach developed by Thomas Kane for deriving the equations of motion that describe a multibody system. This approach offers the advantages of both the Newton-Euler and Lagrange methods, while eliminating their respective disadvantages. For example, external and constraint forces between bodies do not need to be considered since generalized forces are used instead. In addition, the method of vector products is used and eliminates the need for performing extensive differentiation, which result from energy functions,

The derivation of the equations of motion using Kane's method is presented next, adapted from [70], using the principle of virtual work. Consider a multibody system of n interconnected rigid bodies with $3n$ degrees-of-freedom (DOF) each subject to external and constraint forces. The configuration of the system can be described using generalized coordinates as q_r, where $r = 1, 2, \ldots 3n$. Therefore, the virtual work becomes,

$$\delta W \;=\; \Sigma_{i=1}^{n}\, \mathbf{F}_i \cdot \delta \mathbf{r}_i \tag{C.1}$$

where $\mathbf{F}_i$ is the resultant force acting on the i^{th} particle and $\mathbf{r}_i$ is the position vector of the particle with respect to the inertial reference frame. This resultant force is composed of the external, constraint, and inertia forces, acting on the system. Each can be transformed into an equivalent force $\mathbf{F}$ and torque $\mathbf{H}$, which passes through the mass center of body k, such that,

$$\mathbf{F}_k \;+\; \mathbf{F}_k^c \;+\; \mathbf{F}_k^* \;=\; 0 \tag{C.2}$$

where $k = 1, 2 \ldots n$. Equation (C.2) is obtained using d'Alembert's principle, also known as the Lagrange-d'Alembert principle, which states that the sum of the forces acting on a system of mass particles (i.e. on body k) is zero.

Applying (C.1) to a multibody system and only considering the work due to the forces in (C.2) yields,

$$\delta W \;=\; (\mathbf{F}_k \;+\; \mathbf{F}_k^c \;+\; \mathbf{F}_k^*) \;\cdot \delta \mathbf{r}_k \;=\; 0 \tag{C.3}$$

where $\mathbf{F}_k^c \cdot \delta \mathbf{r}_k \;=\; 0$ since the constraint forces typically do not do any work. Therefore,

$$\delta W \;=\; (\mathbf{F}_k \;+\; \mathbf{F}_k^*) \;\cdot \delta \mathbf{r}_k \;=\; (\mathbf{F}_k \;+\; \mathbf{F}_k^*) \;\cdot \frac{\partial \mathbf{r}_k}{\partial q_r} \delta q_r \;=\; 0 \tag{C.4}$$

Before finding the partial derivative of the position vector, it is written in a different form as $\mathbf{r}_k \;=\; \mathbf{r}_k(q_r, t)$, such that its time-derivative gives,

$$\dot{\mathbf{r}}_k \;=\; \frac{\partial \mathbf{r}_k}{\partial q_r} \, \frac{dq_r}{dt} \;+\; \frac{\partial \mathbf{r}_k}{\partial t} \;=\; \frac{\partial \mathbf{r}_k}{\partial q_r} \dot{q}_r \;+\; \frac{\partial \mathbf{r}_k}{\partial t} \tag{C.5}$$

and its partial derivative with respect to $\dot{q}_r$ yields,

$$\frac{\partial \dot{\mathbf{r}}_k}{\partial \dot{q}_r} \;=\; \frac{\partial \mathbf{v}_k}{\partial u_r} \;=\; \frac{\partial \mathbf{r}_k}{\partial q_r} \tag{C.6}$$

Using (C.4) and (C.6), it is appropriate to write an equation for the forces as,

$$\underbrace{\mathbf{F}_k \cdot \frac{\partial \mathbf{v}_k}{\partial \dot{q}_r}}_{f_r} \;+\; \underbrace{\mathbf{F}_k^* \cdot \frac{\partial \mathbf{v}_k}{\partial \dot{q}_r}}_{f_r^*} \;=\; 0 \tag{C.7}$$

where f_r and f_r^* are the generalized active and inertia forces, respectively. Similarly for the moments,

$$\underbrace{\mathbf{T}_k \cdot \frac{\partial \boldsymbol{\omega}_k}{\partial \dot{q}_r}}_{H_r} \;+\; \underbrace{-(\boldsymbol{\alpha}_k \cdot \widehat{I} \;+\; \boldsymbol{\omega}_k \times \widehat{I} \cdot \boldsymbol{\omega}_k) \cdot \frac{\partial \omega_k}{\partial \dot{q}_r}}_{H_r^*} \;=\; 0 \tag{C.8}$$

where H_r and H_r^* are the generalized active and inertia moments, respectively. By summing the external and inertia parts in (C.7) and (C.8), the equations of motion by using Kane's method become,

$$F_r \;+\; F_r^* \;=\; 0 \tag{C.9}$$

where,

$r = 1, \ldots, n$ (n is the number of degrees-of-freedom)

F_r : generalized active (applied) forces

: quantities formed by taking dot products of partial velocities (angular) and active forces (torques)

F_r^* : generalized inertia forces

: quantities formed by taking dot products of the partial velocities and inertia forces/torques

And, for completeness, the general form of (C.9) used in this research for the multi-body systems considered:

$$\underbrace{M(\mathbf{q})\ddot{\mathbf{q}} \; + \; \mathbf{b}(\mathbf{q},\dot{\mathbf{q}}) \; + \; \mathbf{g}(\mathbf{q})}_{-F_r^*} \; = \; \boldsymbol{\Gamma}(\mathbf{q}) \; = \; \underbrace{G^T\boldsymbol{\tau} \; + \; J^T(\mathbf{q})\mathbf{F}}_{F_r} \qquad \text{(C.10)}$$

where,

$M(\mathbf{q})$: is the mass/inertia matrix

$\ddot{\mathbf{q}}, \dot{\mathbf{q}}, \mathbf{q}$: generalized acceleration, velocity and position

$\mathbf{b}(\mathbf{q}, \dot{\mathbf{q}})$: Coriolis vector

$\mathbf{g}(\mathbf{q})$: gravity vector

$\boldsymbol{\Gamma}(\mathbf{q})$: generalized active forces (F_r)

G : generalized torque matrix

$\boldsymbol{\tau}$: actuator joint torques

$J(\mathbf{q})$: Jacobian matrix

$\mathbf{F}$: impact/contact forces vector

Appendix D

Additional Example: Five-Ball Newton's Cradle

A frictionless, five-ball Newton's cradle is considered as shown in Fig. D.1a using the developed approach. This system has five rotational DOFs q_1-q_5, with five balls labeled A, B, C, D, E and equal radius R. The balls hang from massless strings of length L and each string is separated by a distance λ, where $\lambda = 2R$, consistent with balls at rest are in contact. Similar to the three-ball cases, Ball A is released from rest at an arbitrary height and impacts Ball B with initial velocity $\dot{q}_1^-$. Balls B-E are initially at rest, $\dot{q}_2^- = \dot{q}_3^- = \dot{q}_4^- = \dot{q}_5^- = 0$, and in contact. The forces at impact are shown in Fig. D.1b.

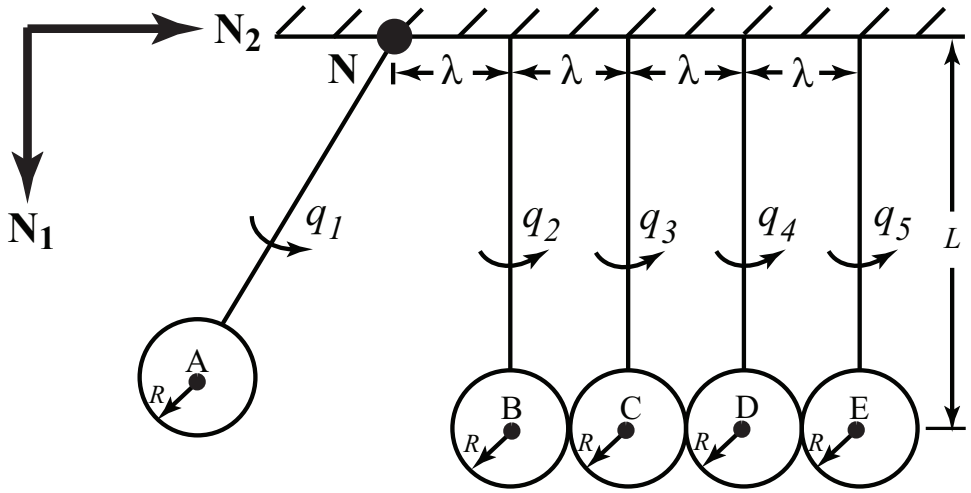

Figure D.1. Planar model of a five-ball Newton's Cradle.

D.0.1 Case 1: Uniform, Unit Masses and $e_* = 1$

This case examines balls with equal, unit mass $m_A = m_B = m_C = m_D = m_E = 1\ kg$, $e_* = 1$, and $v_1^- = 1.0\ m/s$. The same method for treating the indeterminacy for the three ball system is applied here using additional constraints. The motion obtained from simulating this case is shown in Fig. D.2a. As in the previous cases, this figure only shows the first collision, which triggers a single impact event that is

indeterminate with respect to the impact forces. Ball A swings down and collides with Balls B-E, which are at rest and in contact. The momentum is completely transferred to Ball E and Balls A-D remain at rest and in contact after the collision. The data for this case is given in Fig. D.2b.

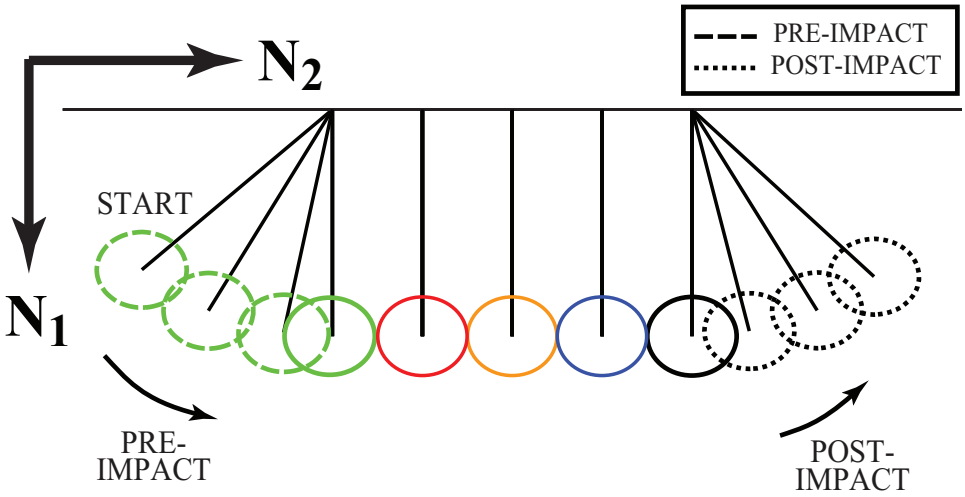

Figure D.2. Simulation of the five-ball Newton's Cradle with $e_* = 1$.

Plots of the normal work done and evolution of component velocities are shown in Fig. D.3. The normal work plot ascends back to zero which corresponds to $W_{nf} = 0$ since $e_* = 1$. The transfer of momentum from Ball A to E occurs, depicted by the normal component velocities of Balls A, v_1 and E, v_{15} in Fig. D.3b. The resulting motion for this case is compared to the theoretical result presented in Table 4 of [79]. For the purpose of comparison, $v_1^- = 1.0\ m/s$ where $\alpha = 1$ and $\gamma = 1$ in [79], which corresponds to uniform, unit masses $m = 1\ kg$ and rigid balls, respectively. A comparison of the theoretical results in this work and [79] is presented in Table D.1. The post-impact motions show that the two are quite different. The result in

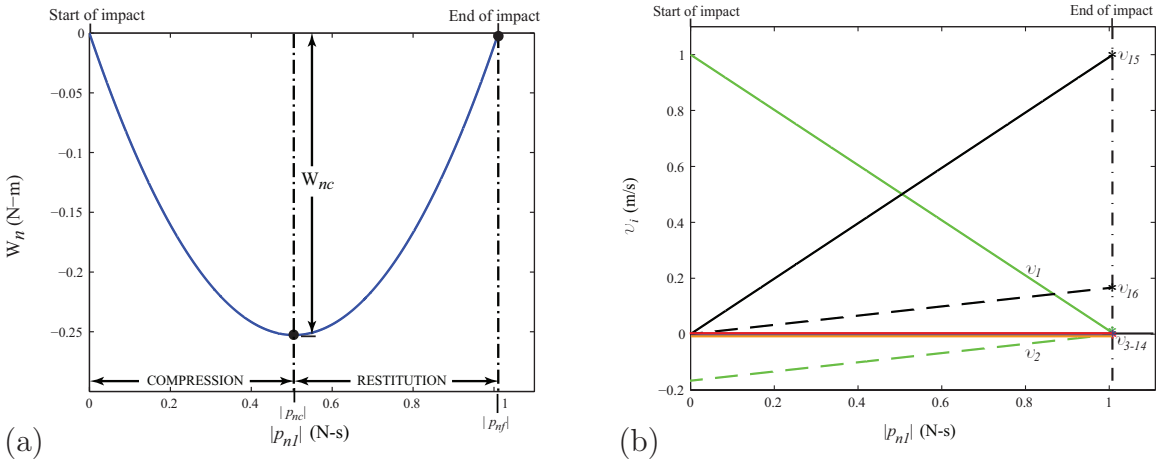

Figure D.3. (a) Normal work done and (b) evolution of velocities throughout the impact event for the five-ball Newton's Cradle with $e_* = 1$.

[79] predicts a motion in which Balls A, B and C reverse direction and Balls D and E move to the right, where most of the momentum is transferred to Ball E. This is in large contrast to the result in this work, which predicts that all the momentum is transferred to Ball E and Balls A-D remain at rest after impact.

Table D.1. Comparison of theoretical results for the five-ball Newton's Cradle with $e_* = 1$, $\alpha = 1$ and $\gamma = 1$ [79].

Theoretical	$\dot{q}_1^+$ (m/s)	$\dot{q}_2^+$ (m/s)	$\dot{q}_3^+$ (m/s)	$\dot{q}_4^+$ (m/s)	$\dot{q}_5^+$ (m/s)	ECOR [-]
Mono-stiffness model [79]	-0.1322	-0.0754	-0.0311	0.2958	0.9429	$e_* = 1$
Rodriguez-Bowling	0.00	0.00	0.00	0.00	1.00	$e_* = 1$

However, the solutions are compared using $\Sigma\ m_i(\dot{q}_i^+)^2$ and $\Sigma\ m_i(\dot{q}_i^-)^2$ parameters, which quantify the consistency of the motions and are found to match. The significance of the results for this case demonstrate the application of the proposed

framework to a five-ball system. The post-impact motion obtained here is similar to the three-ball case, which is expected since $e_* = 1$, but is not comparable to the result in [79]. A plot of the generalized speeds and energy of the system to verify energetic consistency for the simulation is presented in Fig. D.4.

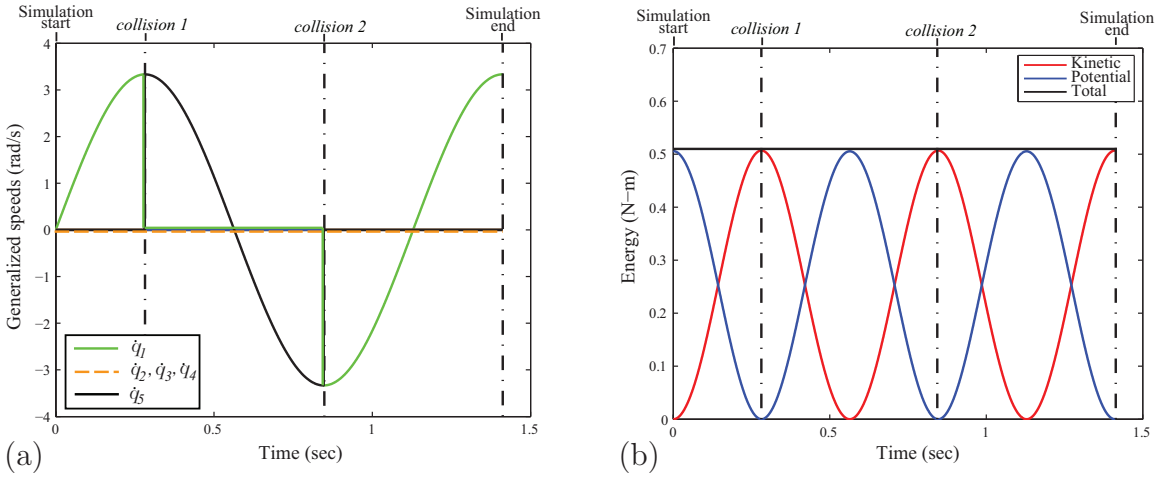

Figure D.4. (a) Generalized speeds for the five-ball Newton's Cradle and (b) energy consistency throughout the simulation with $e_* = 1$.

D.0.2 Case 2: Uniform, Unit Masses and $e_* = 0.8$

The next case considered for the five-ball Newton's cradle examines balls with equal, unit mass $m_A = m_B = m_C = m_D = m_E = 1\ kg$, $e_* = 0.8$, and $v_1^- = 1.304\ m/s$. The motion obtained from simulating this case is depicted in Fig. D.5a. This plot shows the first collision of Ball A with Balls B-E. In this case some energy is dissipated because $e_* = 0.8$; the data for this case is given in Fig D.5b.

The collision of Ball A with Balls B-E triggers *four impact events*, similar to the phenomena for a three-ball Newton's Cradle with $e_* = 0.85$. The first impact event involves all five balls simultaneously and most of the momentum is transferred to Ball

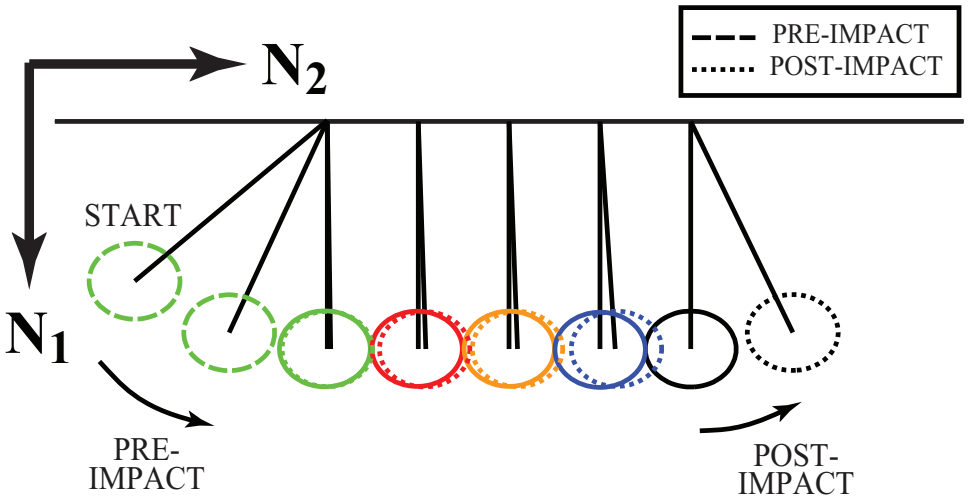

Figure D.5. Simulation of the five-ball Newton's Cradle with $e_* = 0.8$.

E. Once again, the post-impact velocities of the system after the first impact show that Ball A is moving faster to the right than Balls B, C and D while Ball E begins to separate from these balls. This results in a second impact event that only involves Balls A-D, which is indeterminate. The treatment of this second impact event reveals that most of the momentum is transferred to Ball D.

The post-impact velocities of the system indicate that Ball A is still moving to the right at a faster rate than Balls B and C, while Ball D has begun to separate from these balls. This results in a third impact event which only involves Balls A-C, an indeterminate impact event. The same phenomena is observed hereafter in which a fourth impact event is triggered, a determinate impact event. *Again, these multiple impact events stem directly from the analysis with the given model parameters and initial conditions;* there was no a priori knowledge or manipulation of the model or initial conditions to cause this phenomena.

Analysis of the first impact event is shown in Fig. D.6. The energy loss with $e_* = 0.8$ is illustrated in Fig. D.6a because the normal work curve does not ascend back to zero. The evolution of the component velocities, shown in Fig. D.6b, depicts

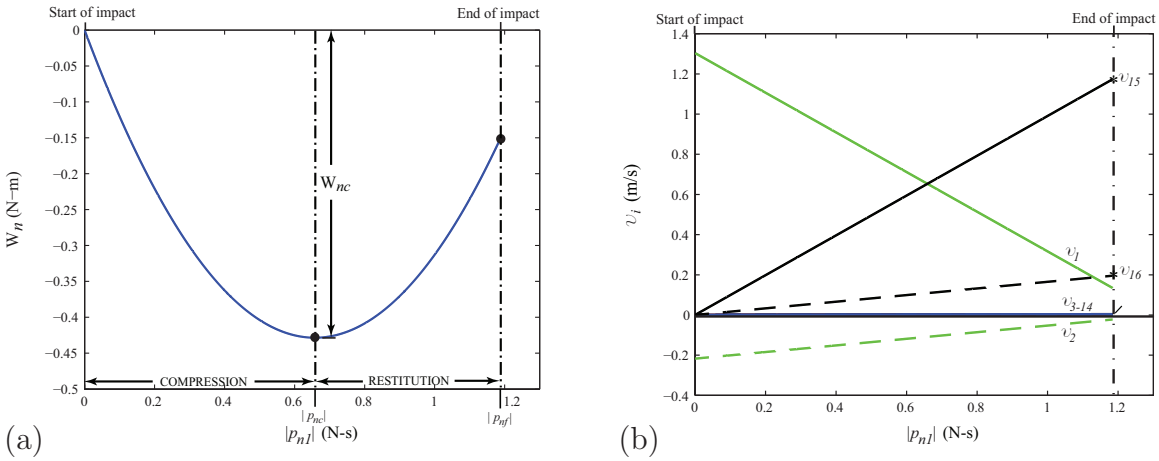

Figure D.6. (a) Normal work done and (b) evolution of velocities throughout the first impact event for the five-ball Newton's Cradle with $e_* = 0.8$.

how the terminal component velocities of Ball E, v_{15-16} are reached. This plot also shows the post-impact velocities of Balls A-D, which serve as the initial conditions for the second impact event; $v_1 > v_3 = v_7 = v_11$ indicating a subsequent impact event.

The analysis of the second impact event is illustrated in Fig. D.7. This impact begins with the post-impact velocities of Balls A-D from the previous impact, in which Ball E has begun to separate from the other balls. The normal work in Fig. D.7a, where $e_* = 0.8$ is used again, shows the energy loss as occurred in the first impact event. The evolution of the component velocities in Fig. D.7b demonstrates how the component velocities of Ball D, v_{11-14} reach their terminal value. This plot also shows the post-impact velocities of Balls A-C; $v_1 > v_3 = v_7$ indicating a subsequent impact.

Treatment of the third and fourth impact events are depicted in Figs. D.8 and D.9. In each impact event, the analysis in Figs. D.8a and D.9a illustrate the energy loss where $e_* = 0.8$ are used. The terminal component velocities of Ball C, v_{7-10} are shown in Fig. D.8b and Balls A, v_{1-2} and B, v_{3-6} are shown in Fig. D.9b.

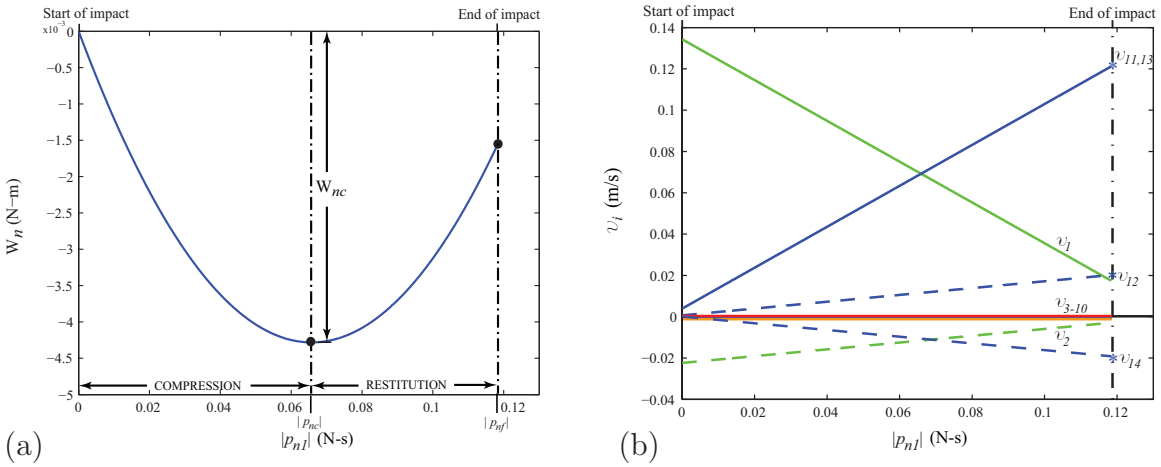

Figure D.7. (a) Normal work done and (b) evolution of velocities throughout the second impact event for the five-ball Newton's Cradle with $e_* = 0.8$.

The propagation of momentum in the resulting motion is obtained here. The post-impact generalized speeds in this case follow $\dot{q}_1^+ < \dot{q}_2^+ < \dot{q}_3^+ < \dot{q}_4^+ < \dot{q}_5^+$. The main differences in these two cases are the mass of the balls, ECOR used and the number of impact events captured. It can be concluded that the mass of each ball and the energy dissipated in the simultaneous collision are the contributing factors in the number of impact events that occur. To the best of their knowledge, the authors could not find a similar example to this case for comparison of the results. A plot of the generalized speeds and energy of the system to verify energetic consistency for the simulation is presented in Fig. D.10.

D.0.3 Case 3: Non-Uniform Masses and $e_* < 1$

As a final study, a non-uniform series of balls with $e_* < 1$ is considered for the five-ball Newton's cradle. The first collision of Ball A with Balls B-E, triggers *four impact events* as occurred in *Case 2*. The first three impact events are indeterminate, while the fourth impact event is determinate. A plot of the motion, as well as analysis

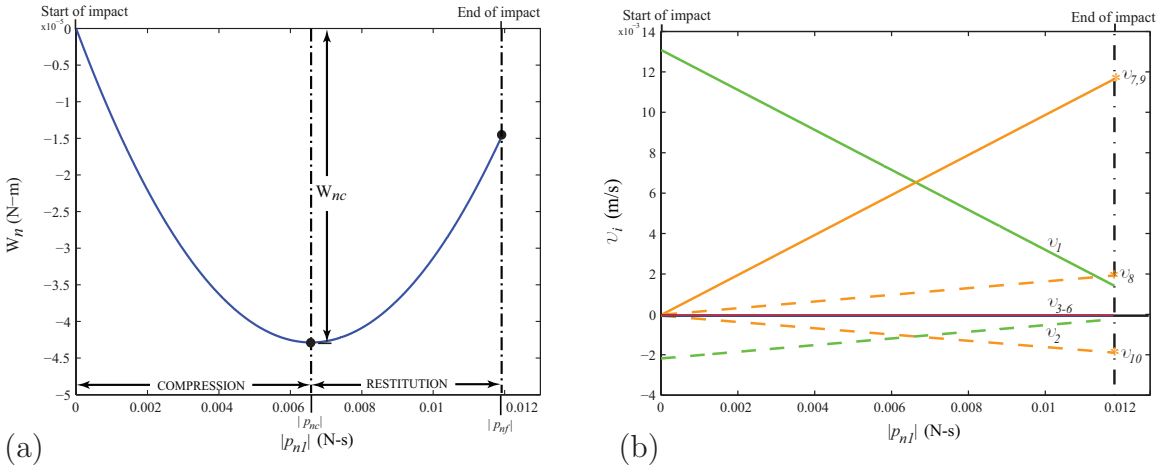

Figure D.8. (a) Normal work done and (b) evolution of velocities throughout the third impact event for the five-ball Newton's Cradle with $e_* = 0.8$.

plots of the normal work and evolution of velocities are not presented here since a similar analysis was given in *Case 2*. Rather, conclusions are made from a comparison of the motion obtained here and the experimental results in [2], which are given in Table D.2. In particular, a comparison of this case is made to the result presented in Fig. 12 of [2]. This case has a pre-impact velocity of $v_1^- = 1.0\ m/s$ for a sequence of balls that follow $ABACA$, where $m = 0.045\ kg$ for a ball type A, and $m = 0.053\ kg$ for ball types B and C, see [2]. The post-impact velocity predictions shown in Fig. 12, [2] were approximated to within $\pm 0.025\ m/s$ from the data given.

In Table 1 of [2], the authors present experimentally determined, local ECORs for a pair of balls with different masses. Three local ECORs are used in [2] for the sequence of balls, $ABACA$, studied in this case. As it was discussed in Sec. 6.3.1, it is difficult to apply the ECOR at each impact point because the ECOR in this work can only function as a global parameter to model the energy dissipated at the *system level*. This is due to the negligible local compliance considered at the impact points. As a result, e_* for this case was adjusted in the proposed approach to obtain a motion

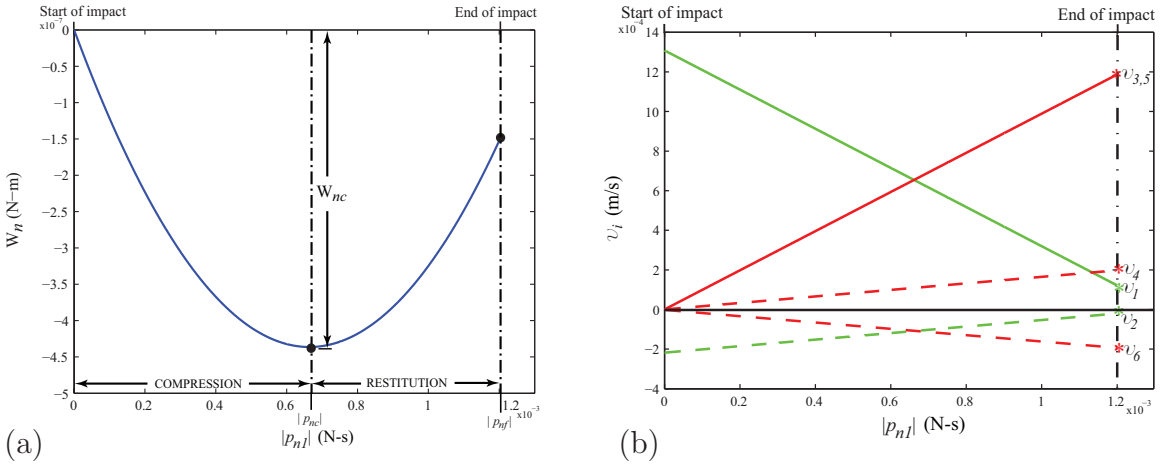

Figure D.9. (a) Normal work done and (b) evolution of velocities throughout the fourth impact event for the five-ball Newton's Cradle with $e_* = 0.8$.

Table D.2. Comparison of theoretical and experimental results of the non-uniform five-ball Newton's Cradle with $e_* < 1$ for a sequence of balls $ABACA$, [2].

		$\dot{q}_1^+$ (m/s)	$\dot{q}_2^+$ (m/s)	$\dot{q}_3^+$ (m/s)	$\dot{q}_4^+$ (m/s)	$\dot{q}_5^+$ (m/s)	ECORs [-]
Experimental	ICR [2]	0.150	0.190	0.200	0.250	0.340	$e_{1,2} = 0.53$ $e_{3,4} = 0.31$
Theoretical	Rodriguez-Bowling	0.046	0.048	0.113	0.221	0.525	$e_* = 0.4$

which was closest to [2]. It was determined that $e_* = 0.4$ for all four impact events produced adequate results. The two solutions in Table 3 do not exactly match but exhibit a similar post-impact motion. The post-impact velocities $\dot{q}_1^+$ and $\dot{q}_2^+$ are much slower compared to [2], whereas $\dot{q}_3^+$ and $\dot{q}_4^+$ are relatively close, and $\dot{q}_5^+$ is predicted to be faster than in [2]. The solutions are somewhat in agreement by comparing the $\Sigma\ m_i(\dot{q}_i^+)^2$ value for consistency of the motion. Plots of the generalized speeds and energy of the system to verify energetic consistency are included in Fig. D.11.

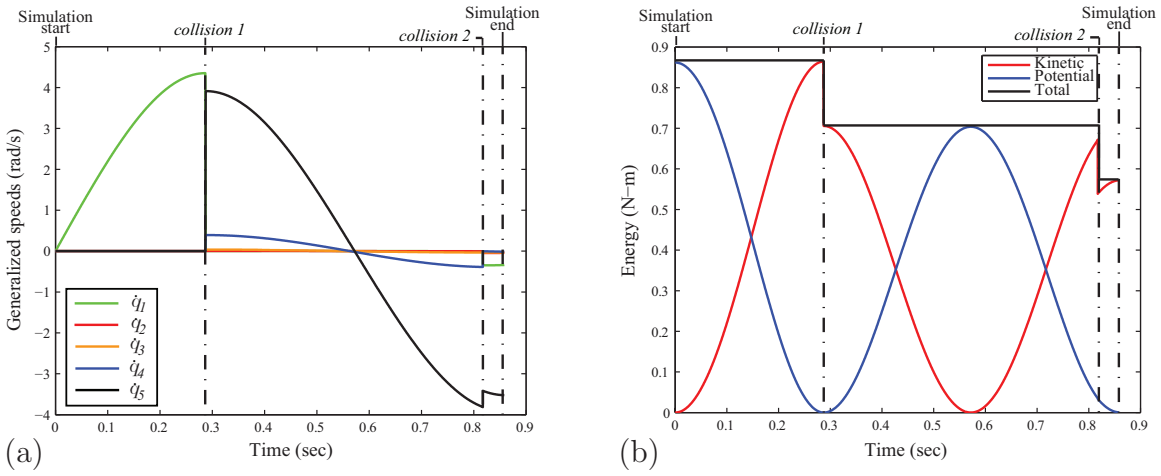

Figure D.10. (a) Generalized speeds for the five-ball Newton's Cradle and (b) energy consistency throughout the simulation with $e_* = 0.8$.

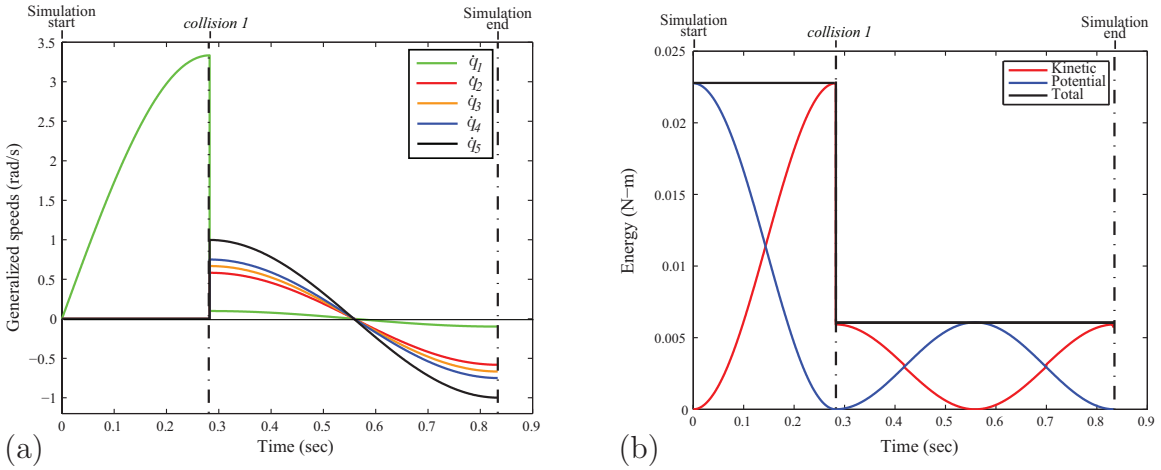

Figure D.11. (a) Generalized speeds for the non-uniform, five-ball Newton's Cradle and (b) energy consistency throughout the simulation .

Table D.3. Model and simulation parameters for the five-ball Newton's Cradle cases.

	Parameter	Value	Unit
Model	L	0.30	m
	R	0.05	m
	λ	0.10	m
Five ball			
Case 1	$m_A - m_E$	1.00	kg
	v_1^-	1.00	m/s
	μ_1, μ_2, μ_3, μ_4	0.0	-
Case 2	$m_A - m_E$	1.00	kg
	v_1^-	1.304	m/s
	μ_1, μ_2, μ_3, μ_4	0.0	-
Case 3	m_A, m_C, m_E	0.045	kg
	m_B, m_D	0.053	kg
	v_1^-	1.00	m/s
	μ_1, μ_2, μ_3, μ_4	0.0	-
Simulation	step size	0.001	s
	abserr	1.0e-12	-
	relerr	1.0e-11	-

References

[1] C. Yilmaz, M. Gharib, and Y. Hurmuzlu, "Solving frictionless rocking block problem with multiple impacts," *Proceedings of the Royal Society A: Mathematical, Physical and Engineering Sciences*, vol. 465, no. 2111, pp. 3323–3339, Nov. 2009.

[2] V. Ceanga and Y. Hurmuzlu, "A new look at an old problem: Newton's cradle," *ASME Journal of Applied Mechanics*, vol. 68, no. 4, pp. 575–583, Apr. 2000.

[3] W. Stronge, *Impact Mechanics*. Cambridge University Press, 2000.

[4] S. Djerassi, "Three-dimensional, one point collision with friction," *Multibody System Dynamics*, vol. 27, no. 2, pp. 173–195, Feb. 2012.

[5] V. Bhatt and J. Koechling, "Three-dimensional frictional rigid-body impact," *Journal of Applied Mechanics*, vol. 62, no. 4, pp. 893–898, Dec. 1995.

[6] ——, "Partitioning the parameter space according to different behaviors during three-dimensional impacts," *ASME Journal of Applied Mechanics*, vol. 62, no. 3, pp. 740–746, Sep. 1995.

[7] D. Marghitu and Y. Hurmuzlu, "Three-dimensional rigid-body collisions with multiple contact points," *ASME Journal of Applied Mechanics*, vol. 62, no. 3, pp. 725–732, Sep. 1995.

[8] R. Brach, *Mechanical Impact Dynamics*. Wiley, New York, 1991.

[9] A. Rodriguez, "Simulation of indeterminate multipoint impact and contact with friction," Master's thesis, University of Texas at Arlington, 2010.

[10] A. Rodriguez and A. Bowling, "Simulation of indeterminate multipoint impact and contact with friction," in *European Community on Computational Methods*

in Applied Sciences (ECCOMAS) Thematic Conference on Multibody Dynamics, July 2011.

[11] ——, "Indeterminate multipoint impact with friction of agile legged robots," in *IEEE International Conference on Robotics and Biomimetics (IEEE-ROBIO)*, December 2011.

[12] ——, "Solution to indeterminate multi-point impact with frictional contact using constraints," *Multibody System Dynamics*, vol. 28, no. 4, pp. 313–330, November 2012.

[13] ——, "Analytic treatment of newton's cradle using constraints," in *European Community on Computational Methods in Applied Sciences (ECCOMAS) Thematic Conference on Multibody Dynamics*, July 2013.

[14] ——, "Study of the stick-slip transition of newton's cradle with friction," in *ASME 2013 International Design Engineering Technical Conferences and Computers and Information in Engineering Conference (IDETC/CIE)*, August 2013.

[15] ——, "Study of newton's cradle using a new discrete approach," *Multibody System Dynamics*, 2013, DOI:10.1007/s11044-013-9406-3.

[16] ——, "Analytic solution of indeterminate multi-point impact problems using stronge's hypothesis," *Multibody System Dynamics*, 2014, (under review).

[17] Y. Gonthier, J. McPhee, C. Lange, and J.-C. Piedboeuf, "A regularized contact model with asymmetric damping and dwell-time dependent friction," *Multibody System Dynamics*, vol. 11, no. 3, pp. 209–233, Apr. 2004.

[18] G. Gilardi and I. Sharf, "Literature survey of contact dynamics modeling," *Mechanism and Machine Theory*, vol. 37, no. 10, pp. 1213–1239, Oct. 2002.

[19] I. Sharf and Y. Zhang, "A contact force solution for non-colliding contact dynamics simulation," *Multibody System Dynamics*, vol. 16, no. 3, pp. 263–290, Oct. 2006.

[20] S. Djerassi, "Collision with friction; Part A: Newton's hypothesis," *Multibody System Dynamics*, vol. 21, no. 1, pp. 37–54, Feb. 2009.

[21] ——, "Collision with friction; Part B: Poisson's and Stronge's hypotheses," *Multibody System Dynamics*, vol. 21, no. 1, pp. 55–70, Feb. 2009.

[22] G. Darboux, "Etude géométrique sur les percussions et le choc des corps," *In Bulletin des Sciences Mathématiques et Astronomiques, deuxiéme série*, vol. 4, no. 1, pp. 126–160, 1880.

[23] J. Keller, "Impact with friction," *Journal of Applied Mechanics, Transactions ASME*, vol. 53, no. 1, pp. 1–4, Mar. 1986.

[24] W. Stronge, "Smooth dynamics of oblique impact with friction," *International Journal of Impact Engineering*, vol. 51, pp. 36–49, Jan. 2013.

[25] P. Bergés and A. Bowling, "Rebound, slip, and compliance in the modeling and analysis of discrete impacts in legged locomotion," *Journal of Vibration and Control*, vol. 17, no. 12, pp. 1407–1430, Dec. 2006.

[26] S. Djerassi, "Stronge's hypothesis-based solution to the planar collision-with-friction problem," *Multibody System Dynamics*, vol. 24, no. 4, pp. 493–515, Dec. 2010.

[27] B. Brogliato, A. Ten Dam, L. Paoli, F. Génot, and M. Abadie, "Numerical simulation of finite dimensional multibody nonsmooth mechanical systems," *Applied Mechanics Reviews*, vol. 55, no. 2, pp. 107–149, Mar. 2002.

[28] A. Bowling, D. Flickinger, and S. Harmeyer, "Energetically consistent simulation of simultaneous impacts and contacts in multibody systems with friction," *Multibody System Dynamics*, vol. 22, no. 1, pp. 27–45, Aug. 2009.

[29] M. Anitescu and F. Potra, "Formulating dynamic multi-rigid-body contact problems with friction as solvable linear complementarity problems," *Nonlinear Dynamics*, vol. 14, no. 3, pp. 231–247, Nov. 1997.

[30] A. Chatterjee, "On the realism of complementarity conditions in rigid body collisions," *Nonlinear Dynamics*, vol. 20, no. 2, pp. 159–168, Oct. 1999.

[31] H. Lankarani, "Contact force model with hysteresis damping for impact analysis of multibody systems," *Journal of Mechanics and Design*, vol. 112, no. 3, pp. 369–376, Sep. 1990.

[32] W. Goldsmith, *Impact: The Theory and Physical Behavior of Colliding Solids*. Edward Arnold Publishers Ltd, London, 1960.

[33] H. Hertz, *Miscellaneous papers*. H. Hertz, Jones, and Schott, London, 1896.

[34] K. Hunt and F. Crossley, "Coefficient of restitution interpreted as damping in vibroimpact," *Journal of Applied Mechanics, Trans. ASME*, vol. 42, no. 2, pp. 440–445, Jun. 1975.

[35] C. Canudas de Wit, H. Olsson, K. Astrom, and P. Lischinsky, "A new model for control of systems with friction," *IEEE Trans. Automatic Control*, vol. 40, no. 3, pp. 419–425, Mar. 1995.

[36] O. Bauchau and J. Changkuan, "Modeling friction phenomena in flexible multibody dynamics," *Computational Methods Applied Mechancial Engineering*, vol. 195, no. 16, pp. 6909–6924, Jun. 2006.

[37] W. Iwan, "On a class of models for the yielding behavior of continuous and composite systems," *ASME Journal of Applied Mechanics*, vol. 89, no. 3, pp. 612–617, Sep. 1967.

[38] P. Dahl, "Solid friction damping of mechanical vibrations," *AIAA Journal*, vol. 14, no. 12, pp. 1675–1682, Dec. 1976.

[39] J. Moreau, "Numerical aspects of the sweeping process," *Computer Methods in Applied Mechanics and Engineering*, vol. 177, no. 3, pp. 329–349, May 1999.

[40] A. Banerjee and T. Kane, "Modeling and simulation of rotor bearing friction," *Journal of Guidance Control Dynamics*, vol. 17, no. 5, pp. 1137–1151, Jan. 1994.

[41] O. Bauchau and J. Rodriguez, "Modeling of joints with clearance in flexible multibody systems," *International Journal of Solids Structures*, vol. 39, pp. 41–63, 2002.

[42] C. d. Coulomb, "Théorie des machines simples, en ayant égard au frottement de leurs parties, et la roideur des cordages," *Piéce qui a reporté le Prix double de l'Académie des Sciences pour l'année*, pp. 163–332, 1785.

[43] P. Song, P. Krauss, and P. Dupont, "Analysis of rigid-body dynamic models for simulation of systems with frictional contacts," *ASME Journal of Applied Mechanics*, vol. 68, no. 1, pp. 118–128, Jun. 2000.

[44] C. Glocker and C. Studer, "Formulation and preparation for numerical evaluation of linear complentarity systems in dynamics," *Multibody System Dynamics*, vol. 13, no. 4, pp. 447–463, May 2005.

[45] D. Karnopp, "Computer simulation of stick-slip friction in mechanical dynamic systems," *Journal of Dynamic Systems, Measurement, and Control*, vol. 107, no. 1, pp. 100–103, Mar. 1985.

[46] D. Haessig and B. Friedland, "On the modeling and simulation of friction," *American Control*, vol. 113, no. 3, pp. 354–362, Sep. 1991.

[47] I. Han and B. Gilmore, "Multi-body impact motion with friction-analysis, simulation, and experimental validation," *Journal of Mechanical Design, Transactions of the ASME*, vol. 115, no. 3, pp. 412–422, Sep. 1993.

[48] T. Mouri, T. Yamada, A. IWAI, N. Mimura, and Y. Funahashi, "Identification of contact conditions from contaminated data of contact force and moment," *Proceedings IEEE International Conference on Robotics and Automation*, vol. 1, pp. 597–603, May 2001.

[49] A. Bowling, "Dynamic performance, mobility, and agility of multi-legged robots," vol. 128, no. 4, pp. 765–777, Dec. 2006.

[50] J. Dormand and P. Prince, "A family of embedded runge-kutta formulae," *Journal of Computational and Applied Mathematics*, vol. 6, no. 1, pp. 19–26, Mar. 1980.

[51] P. Flores, R. Leine, and C. Glocker, "Modeling and analysis of planar rigid multibody systems with translational clearance joints based on the non-smooth dynamics approach," *Multibody System Dynamics*, vol. 23, no. 2, pp. 165–190, Feb. 2010.

[52] J. Choi, H. Ryu, C. Kim, and J. Choi, "An efficient and robust contact algorithm for a compliant contact force model between bodies of complex geometry," *Multibody System Dynamics*, vol. 23, no. 1, pp. 99–120, Jan. 2010.

[53] D. Lopes, M. Silva, J. Ambrosio, and P. Flores, "A mathematical framework for contact detection between quadric and superquadric surfaces," *Multibody System Dynamics*, vol. 24, no. 3, pp. 255–280, Oct. 2010.

[54] D. Flickinger and A. Bowling, "Simultaneous oblique impacts and contacts in multibody systems with friction," *Multibody System Dynamics*, vol. 23, no. 3, pp. 249–261, Mar. 2010.

[55] Y. Wang, V. Kumar, and J. Abel, "Dynamics of rigid bodies undergoing multiple frictional contacts," *Proc-IEEE Int'l Conference on Robotics and Automation*, vol. 3, pp. 2764–2769, May 1992.

[56] L. Johansson, "A Newton method for rigid body frictional impact with multiple simultaneous impact points," *Computer Methods in Appl. Mechanics Engineering*, vol. 191, pp. 239–254, Nov. 2001.

[57] Y. Maeda, K. Oda, and S. Makita, "Analysis of indeterminate contact forces in robotic grasping and contact tasks," *IEEE International Conference on Intelligent Robots and Systems*, pp. 1570–1575, Oct. 2007.

[58] T. Omata and K. Nagata, "Rigid body analysis of the indeterminate grasp force in power grasps," *IEEE Transactions on Robotics and Automation*, vol. 16, no. 1, pp. 46–54, Feb. 2000.

[59] Y. Hurmuzlu and D. Marghitu, "Rigid body collisions of planar kinematic chains with multiple contact points," *International Journal of Robotics Research*, vol. 13, no. 1, pp. 82–92, Feb. 1994.

[60] Y. Wang and M. Mason, "Two-dimensional rigid-body collsions with friction," *Journal of Applied Mechanics*, vol. 59, pp. 635–642, Sep. 1992.

[61] W. Stronge, "Friction in collisions: resolution of a paradox," *Journal of Applied Physics*, vol. 69, no. 2, pp. 610–612, Jan. 1991.

[62] A. Bedford and W. Fowler, *Engineering Mechanics: Dynamics*. Pearson Education, Inc., 2008.

[63] M. Brake, "An analytical elastic-perfectly plastic contact model," *International Journal of Solids and Structures*, vol. 49, no. 22, pp. 3129–3141, Nov. 2012.

[64] R. Jackson, I. Green, and D. Marghitu, "Predicting the coefficient of restitution of impacting elastic-perfectly plastic spheres," *Nonlinear Dynamics*, vol. 60, no. 3, pp. 217–229, Mar. 2010.

[65] Y. Zait, V. Zolotarevsky, Y. Kligerman, and I. Etsion, "Multiple normal loading-unloading cycles of a spherical contact under stick contact condition," *ASME Journal of Tribology*, vol. 132, no. 4, pp. 041 401–1–7, Sep. 2010.

[66] E. Whittaker, *A Treatise on the Analytical Dynamics of Particles and Rigid Bodies*. Cambridge University Press, 2nd ed., 1917.

[67] E. Routh, *Dynamics of a system of rigid bodies*. MacMillan & Co., London, 1905.

[68] D. Stoianovici and Y. Hurmuzlu, "A critical study of the applicability of rigid-body collision theory," *Journal of Applied Mechanics*, vol. 63, pp. 307–316, 1996.

[69] C. Glocker and F. Pfeiffer, "Multiple impacts with friction in rigid multi-body systems," *Nonlinear Dynamics*, vol. 7, no. 4, pp. 471–497, Jun. 1995.

[70] T. Kane and D. Levinson, *Dynamics: Theory and Applications*. McGraw-Hill, New York, 1985.

[71] D. Marghitu and E. Stoenescu, "Rigid body impact with moment of rolling friction," *Nonlinear Dynamics*, vol. 50, no. 3, pp. 597–608, Nov. 2007.

[72] W. Yao, B. Chen, and C. Liu, "Energetic coefficient of restitution for planar impact in multi-rigid-body systems with friction," *International Journal of Impact Engineering*, vol. 31, no. 3, pp. 255–265, Mar. 2005.

[73] D. Stewart, "Rigid-body dynamics with friction and impact," *SIAM Review*, vol. 42, no. 1, pp. 3–39, Mar. 2000.

[74] B. Brogliato, *Nonsmooth Mechanics: Models, Dynamics and Control*. Springer-Verlag London Ltd., 2nd ed., 1999.

[75] F. Prieto and P. Lourenço, "On the rocking behavior of rigid objects," *Meccanica*, vol. 40, no. 2, pp. 121–133, Apr. 2005.

[76] B. Brogliato, H. Zhang, and C. Liu, "Analysis of a generalized kinematic impact law for multibody-multicontact systems, with application to the planar rocking block and chains of balls," *Multibody System Dynamics*, vol. 27, no. 3, pp. 351–382, Jan. 2012.

[77] V. Seghete and T. Murphey, "Multiple instantaneous collisions in a variational framework," in *Proceedings of the IEEE Conference on Decision and Control*, Dec. 2009, pp. 5015–5020.

[78] C. Liu, Z. Zhao, and B. Brogliato, "Frictionless multiple impacts in multibody systems. i. Theoretical framework," *Proc. R. Soc. A Math. Phys. Eng. Sci.*, vol. 464, no. 2100, pp. 3193–3211, Dec. 2008.

[79] ——, "Frictionless multiple impacts in multibody systems. II. Numerical algorithm and simulation results," *Proceedings of the Royal Society A: Mathematical, Physical and Engineering Sciences*, vol. 465, no. 2101, pp. 1–23, Jan. 2009.

[80] C. Glocker and U. Aeberhard, "The geometry of Newton's cradle," *Nonsmooth Mechanics and Analysis: Theoretical and Numerical Advances*, vol. 12, pp. 185–194, 2006.

[81] J. Batlle, "The sliding velocity flow of rough collisions in multibody systems," *ASME Journal of Applied Mechanics*, vol. 63, no. 3, pp. 804–809, Sep. 1996.

[82] J. Craig, *Introduction to Robotics: Mechanics and Control*. Addison-Wesley Publishing Company, Inc., 1989.

Biographical Information

Adrian Rodriguez was born and raised in the small town of Eagle Pass, Texas on April 12, 1987. He grew a fascination for the subjects of math and science in middle school, where he competed in U.I.L. events of Number Sense, Calculator Applications and General Math. This fascination for math and science developed into a passion in high school during the launch of the Mars Exploration Rovers - Spirit and Opportunity.

Adrian graduated high school in 2005, 4th in his class, and went on to major in Mechanical Engineering at the University of Texas at Austin. At Texas, he bred his skills in engineering, worked as a student assistant in the Executive Education department in the Red McCombs School of Business, and actively participated in various student organizations: American Society of Mechanical Engineers, Robotics and Automation Society, The Navigators and co-founding Texas Golf Club. In the latter stages of the program, Adrian contemplated the idea of research and pursuing graduate school. After participating in an undergraduate research program, Intellectual Entrepreneurship, he knew research was the next step. Adrian graduated from Texas in May 2009.

In fall 2009, Adrian began the master's program in Mechanical Engineering at the University of Texas at Arlington. He conducted research in the area of multibody dynamics under the supervision of Dr. Alan Bowling. It is during this time that he strengthened his research skills and realized that it was something he wanted to continue at the doctoral level. After defending his thesis and receiving his Masters of Science degree in December 2010, Adrian began the doctoral program at UTA as a

fellow of the Louis Stokes Alliance for Minority Participation program. This provided Adrian the resources to fund his research and present at national and international conferences - 6 in total. During his time at UTA, Adrian balanced his research work with various engineering projects and student organizations, while holding several leadership positions: DARPA Robotics Challenge, American Society of Mechanical Engineers, UTA Volunteers, Graduate Student Senate, UTA-HOSTS mentoring program, ROVER Society at UTA, Golden Key International Honour Society and Latin American Student Organization. Adrian also began part-time work as a Mechanical Engineer at Clovis Research, L.C. in July 2013, Adjunct Professor for Thermodynamics II and Graduate Research Assistant/Intern at UTA Research Institute in January 2014. Adrian received his Ph.D. in Mechanical Engineering from UTA in May 2014.

Adrian's favorite food is cheese enchiladas and enjoys travel, playing golf, exercising, reading magazines, and collects television series of any genre. Adrian met his better half, Amanda Sanchez, as a junior in high school and they have remained together throughout their undergraduate programs at Texas and graduate programs (him at UTA, her at Texas Weslayan School of Law). They plan to tie the knot on December 27, 2014 in Austin, Texas.